Investigation of transport phenomena in semiconductors and semiconductor devices: drain noise, two-phonon scattering, and phonon drag

Thesis by
Iretomiwa Esho

In Partial Fulfillment of the Requirements for the
Degree of
Doctor of Philosophy

Caltech

CALIFORNIA INSTITUTE OF TECHNOLOGY
Pasadena, California

2024
Defended December 7, 2023

ACKNOWLEDGEMENTS

I wish to start by extending my gratitude to Professor Austin Minnich, my advisor, for his guidance and mentorship throughout the past five years. His commitment to the development of his students is unquestionable, and I appreciate his efforts in fostering a positive and supportive work atmosphere within our group.

I thank my thesis committee members, Dr. Stevan Nadj-Perge, Dr. Melany Hunt, and Dr. Kieran Cleary, for serving on my defense committee. I extend my appreciation to Kieran for welcoming me into the Cahill Radio Astronomy Laboratory during my second year, where I learned everything I know about transistor amplifiers.

Special thanks to Dr. Ankur Jain, Dr. Alan Bowling, and Dr. Krishna Shah, for introducing me to the realm of scientific research and offering invaluable support, guidance, and mentorship in my undergraduate years.

I am grateful for the friendships I cultivated at Caltech. Taeho Kim, Hirsh Kamakari, Nachiket Naik, Adrian Tan, Benjamin Hatanpaa, Zachery Iton, Neehar Kondapaneni: thanks for making the last five years memorable. I would like to thank Alexander Choi for his support throughout the years. To Bekari Gabritchidze: you are an amazing human. Thank you for everything. To the Minnich Group members, it was a pleasure to meet you all and learn from each one of you. Justin, I enjoyed very much all our discussions and I can't wait to see all you accomplish. To the SOPS IM football team, playing with you all was one of my favorite things to do at Caltech. Thank you.

Many thanks to Tesleem Lawal for the enduring friendship and support during our shared challenges throughout the PhD journey. Madhu Tennakoon and Tife Moyela: I am glad we crossed paths. Thank you for inspiring me.

To my partner Ose: Thank you for your constant love, support, and patience throughout this journey. To my sisters Ola, Lana, and Lola, thank you for always being there. Finally, to my parents Michael and Abimbola: none of this would have been possible without your sacrifice and unwavering dedication to your kids' education. Thank you.

ABSTRACT

The dynamics of charge carriers in semiconductors set the foundation for semiconductor device performance. Devices crucial for fields like radio astronomy rely on transistor amplifiers where hot electron dynamics impact noise significantly. The overarching goal of this work is to contribute towards the development of better transistor amplifiers by investigating electron transport in existing devices and emerging materials.

The physical mechanisms governing noise in a class of semiconductor devices called high electron mobility transistors (HEMTs) are not completely understood. HEMTs are transistors that use a junction between two materials of different band gaps as the channel. HEMTs are used as amplifiers by translating a small signal applied at the gate terminal to a large current at the drain terminal or output. The noise added at the input is well-characterized by the device physical temperature, while the origin of the noise added at the output is still up for debate. We attempt to fill this knowledge gap by proposing a theory of noise occurring at the drain terminal of these devices as a type of partition noise arising from two possible electron paths. This theory emphasizes the critical role of the conduction band offset between epitaxial layers of the device: a larger offset maximizes the channel sheet density and minimizes electron transfer between layers, potentially improving noise performance. The theory accounts for the magnitude and dependencies of the drain temperature and suggests strategies to realize devices with lower noise.

We then investigate phonon-limited charge transport in the semiconductor boron arsenide. Boron arsenide has drawn significant interest due to reports of simultaneous high thermal conductivity and ambipolar charge mobility, desirable properties for integration in electronic devices. The theoretical prediction of high electron and hole mobility assumed the dominance of charge carrier scattering by one phonon. We consider the effects of two-phonon electron and hole scattering processes in boron arsenide, and find that inclusion of these higher-order processes reduces the computed room-temperature electron and hole mobility significantly from the one-phonon value. Despite its potential, our predictions of electron and hole mobility contradict recent experimental reports based on photoexcited charge carrier diffusion. Several factors may explain this discrepancy, including another type of two-phonon scattering not

considered in this work, superdiffusion of hot carriers, induced carrier concentration, or a combination of all or some of the above elements.

At high carrier concentrations, the phonon system may interact with the electron system on the timescale of the phonon-phonon interaction. When this happens, the nonequilibrium state of phonons becomes important for electron transport, and vice versa as these systems interact in a coupled manner. This coupled interaction could lead to an inflated value of the experimentally reported mobility. We quantify this effect, known as phonon drag, with a coupled electron-phonon Boltzmann transport equation framework and demonstrate that the electron mobility is indeed enhanced significantly at the relevant carrier densities.

PUBLISHED CONTENT AND CONTRIBUTIONS

[1] Iretomiwa Esho and Austin J. Minnich. Charge transport in BAs and the role of two-phonon scattering. In: *Physical Review B* 108.16 (2023). `https://journals.aps.org/prb/abstract/10.1103/PhysRevB.108.165202`, p. 165202.

I.E. co-designed the research, conducted the calculations, analyzed the data, and wrote the manuscript.

[2] Iretomiwa Esho, Alexander Y. Choi, and Austin J. Minnich. Theory of drain noise in high electron mobility transistors based on real-space transfer. In: *Journal of Applied Physics* 131.8 (2022). `https://doi.org/10.1063/5.0069352`.

I.E. co-designed the research, conducted the calculations, analyzed the data, and wrote the manuscript.

[3] Alexander Y. Choi, Iretomiwa Esho, et al. Characterization of self-heating in cryogenic high electron mobility transistors using Schottky thermometry. In: *Journal of Applied Physics* 130.15 (2021). `https://pubs.aip.org/aip/jap/article/130/15/155107/1062506`.

I.E. conducted Schottky thermometry measurements, contributed to data analysis, and provided edits to the manuscript.

CONTENTS

LIST OF FIGURES

Number *Page*

Chapter 1

INTRODUCTION

A physical understanding of charge dynamics in semiconductor devices is of paramount importance across various domains, including telecommunications, energy conversion, radio astronomy, and quantum computing. As these devices continue to undergo miniaturization, applied voltages on the order of 1 V or less can lead to electric fields $\sim 10^5$ V cm^{-1} [1]. Such high fields are known to heat charge carriers to temperatures significantly higher than that of the host lattice, and may ultimately degrade device performance. In particular, fields such as radio astronomy rely on transistor amplifiers for amplification of very weak signals, and the quality of signal amplification, or equivalently amplifier noise performance, is dependent on the dynamics of hot electron transport in the transistor.

In addition to the contribution from hot electron dynamics to the noise performance, several other properties of the conducting material can influence the performance of a device. For example, the low-field velocity response of a material to an electric field is an important parameter: materials possessing higher drift velocity for a given applied field are typically more desirable for high-frequency applications. Thermally conductive materials are also more desirable as they are able to dissipate unwanted heat better to the surrounding medium. Poor heat dissipation is of considerable importance and degrades several device characteristics, including noise performance [2, 3, 4]. Therefore, we are motivated to not only pursue a deeper understanding of the factors limiting the noise performance of these electronic devices, but also to seek out and investigate materials that could ultimately form the foundation for improved device performance.

This thesis consists of two parts. The first part, covered in Chapter 2 presents a new explanation for the origin of a type of noise observed in high electron mobility transistors (HEMTs). The second part, explored in Chapters 2 and 3, is a first-principles analysis of the charge carrier characteristics of a promising novel semiconductor material with the potential for integration into various electronic device categories in the future.

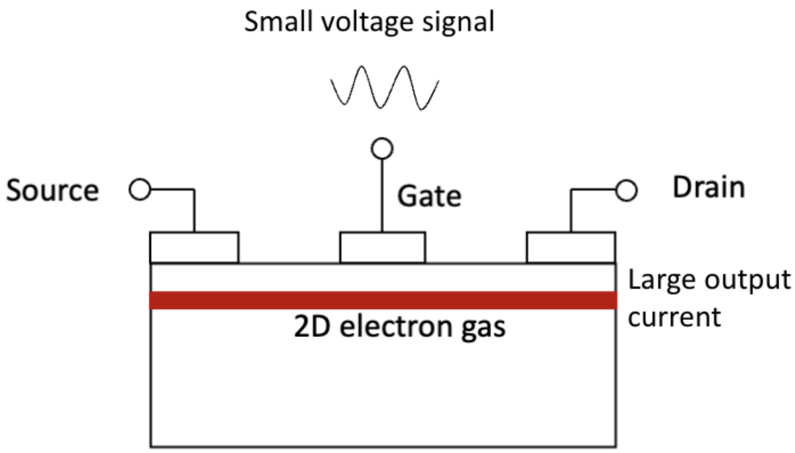

Figure 1.1: Schematic of HEMT showing the source, gate, and drain terminals, 2D electron gas, and illustrating the principle of amplification. A signal to be amplified is added at the input gate terminal, which then modulates the current observed at the drain terminal when the device is biased.

In this chapter, we will outline the central problem we aim to tackle and introduce several concepts foundational to our approach. These elements provide necessary context for subsequent chapters.

1.1 HEMTs and the limits of noise performance

A high electron mobility transistor (HEMT) is a type of transistor that uses a heterojunction as the conducting channel. The heterojunction is made of two semiconductors with different bandgaps, such as InAlAs/InGaAs. The conducting electrons are confined in a quantum well, forming a 2D electron gas (2DEG). The conducting electrons are physically isolated from dopants to preserve the high electron mobility. The HEMT has three terminals: source, gate, and drain. Electrons travel from source to drain under the application of a drain-source voltage, and the current seen at the drain can be modulated by the application of a gate-source voltage. Figure 1.1 shows a schematic of the HEMT that pictorially depicts its basic principle of operation: a small input signal at the gate is observed as current modulation at the drain end of the device.

The noise performance of a device is usually characterized with an overall (noise) temperature. All contributing elements to the noise are captured by this temperature. The noise temperature is a way to express the noise power

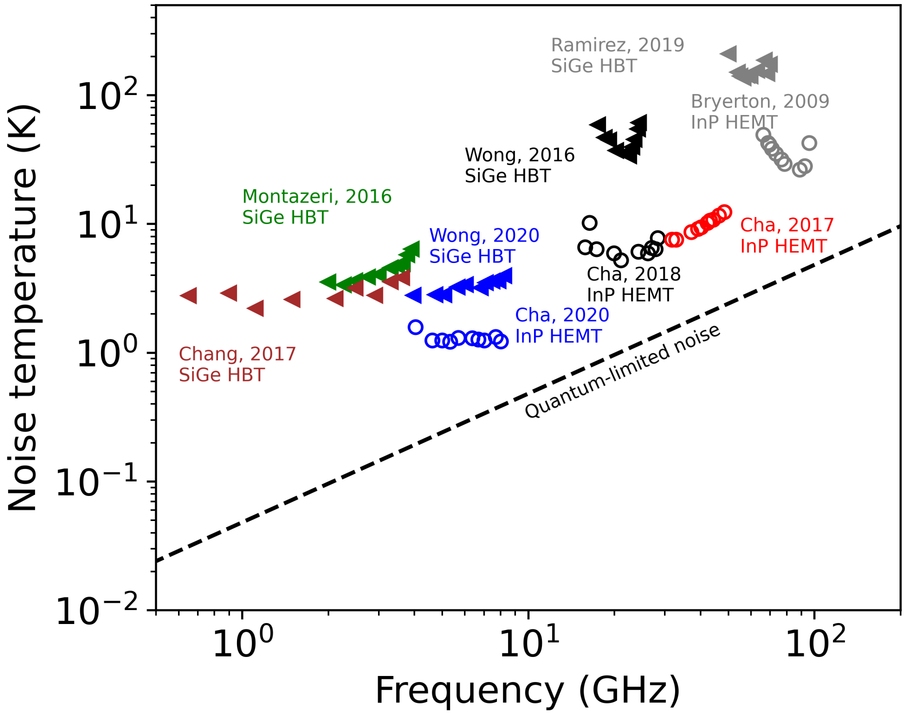

Figure 1.2: Figure showing that HEMT amplifiers exhbibit state-of-the-art noise performance in the 5–100 GHz frequency range. The best HEMT low-noise amplifiers (LNAs) have a noise figure 4 to 10 times the quantum limit in the given range, but applications continue to drive the development of better amplifiers.

of a component or system as if it were caused by thermal fluctuations at a certain temperature. Lower noise temperature values indicate less noise and are generally desirable in electronic systems, but especially in applications like radio astronomy, where sensitivity to faint signals is crucial. Currently, amplifiers based on HEMTs boast state-of-the-art performance below 100 GHZ, outperforming other amplifiers such as silicon-germanium (Si-Ge) heterojunction bipolar transistors (HBTs). Figure 1.2 is a plot of the noise temperature of state-of-the-art HEMTs compared to their SiGe HBT counterparts.

This figure illustrates that although HEMTs provide comparatively good noise performance, there is still room for improvement as the best devices still possess a noise temperature $\sim 4\times\ T_{QL}$, where T_{QL} is the standard quantum limit for noise [5]:

$$T_{QL} = \frac{hf}{k_B} \tag{1.1}$$

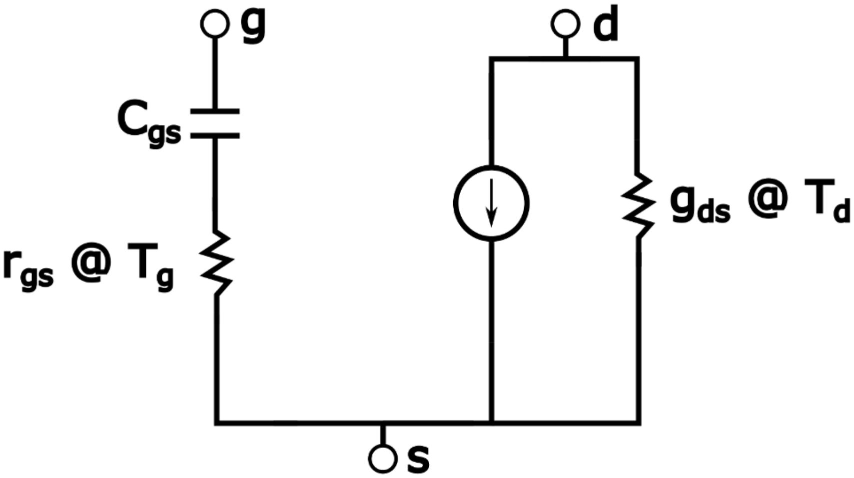

Figure 1.3: Figure showing that the noise sources in HEMTs are typically interpreted using an equivalent circuit proposed by Marian Pospieszalski in 1989 [6]. In this model, the noise properties of an intrinsic chip are treated by assigning equivalent temperatures T_g and T_d to the resistive elements r_{gs}, the gate source resistance, and g_{ds}, the output conductance of the equivalent circuit.

Here, h is Planck's constant, f is frequency of operation, and k_B is the Boltzmann constant.

Since noise in HEMTs is typically interpreted as noise arising from the random thermal motion of electrons in a resistor, noise models of HEMTs generally assign equivalent physical temperatures to resistors in the HEMT (see Fig. 1.3). For example, in the widely adopted Pospieszalski model, the noise contribution from the input (gate) terminal is well represented by setting this noise temperature to the physical temperature of the device [6]. Therefore, cooling the device generally results in a reduced noise temperature and improved noise performance. On the contrary, the drain-source resistance which is assigned a drain temperature T_d is typically employed as a fitting parameter. The drain noise determines the minimum achievable noise temperature of a HEMT and despite its significance, there is no consensus yet as to its physical origin. Understanding the microscopic mechanisms behind T_d would be crucial to effectively mitigate its impact on HEMT noise performance.

1.2 First-principles approach to semiconductor property prediction

As mentioned in the previous section, the dynamics of electron transport in devices is significantly influenced by electron-phonon interactions. In recent years, there has been substantial advancement in first-principles methodologies to study electron-phonon interactions that integrate density functional theory [7]. The study of electrons in materials presents a complex many-body problem that necessitates the application of statistical principles to describe fundamental characteristics of materials, and approximations are often required to make real progress in establishing quantitative theories. The most commonly employed approximation is the independent-electron approximation. In this approach, each electron acts in an effective potential, independent of other electrons.

Density functional theory

Density functional theory (DFT) provides a rigorous way to describe the electron characteristics of atoms, molecules, and solids, allowing for prediction of a vast array of properties such as lattice parameters, electronic band structures, optical absorption, electrical and thermal conductivity, and superconductivity to name a few. By minimizing the total energy of a system with respect to the electron density, DFT enables the determination of ground-state properties and offers valuable insights into the behavior of electrons in matter.

The fundamental principle of DFT is that any property of a many-body system can be written as a functional of the ground state density of that system. The modern DFT formulation was proposed by Hohenberg and Kohn in 1964 [8] when they showed that all properties of a many body system can be viewed as unique functionals of the ground state density. For a system of interacting particles the Hamiltonian is of the form:

$$H = -\frac{\hbar^2}{2m_e}\sum_i \nabla_i^2 + \sum_i V_{\text{ext}}(\mathbf{r}_i) + \frac{1}{2}\sum_{i\neq j}\frac{e^2}{|\mathbf{r}_i - \mathbf{r}_j|} \tag{1.2}$$

where the three terms on the right hand side of Eq. 1.2 represent the kinetic energy term, the potential energy term due to the nuclei, and the electron-electron interactions, respectively. Hohenberg and Kohn's formulation is based on two theorems:

1. For a system of particles interacting within an external potential, the potential is determined uniquely by the ground state particle

density of the system.

> **2**. A universal functional for the energy in terms of the density can be defined for any external potential, and the ground state energy of the system is the global minimum of this functional. The density that minimizes the energy is the exact ground state density of the system.

A consequence of the first theorem is that given the ground state density, the many-body wavefunctions of all states are determined (since we have determined the density and thus the Hamiltonian), thus all properties of the system are determined. From the second theorem, it follows that to determine the ground state density and energy, the energy functional is sufficient. The proofs of the theorems are straightforward and can be found in several electronic structure texts, so we do not repeat them here but highlight the important points. For the first theorem, the proof relies on considering two different (by more than a constant) external potentials that result in the same ground state density. By considering expressions for the energy in both cases, one can arrive at a contradictory statement which then mandates that there cannot be two different external potentials that lead to the same ground density.

For the proof of the second theorem, we first define a new quantity $F[n]$ that is a functional of the density, such that it contains information about the interacting electron system. We can again show by similar arguments in the previous case that if $F[n]$ is known, then minimizing the total energy with respect to the density would lead us to the exact ground state density. Note that these theories by themselves do not prescribe a way to solve the many-body problem. This is where the Kohn-Sham approach to the many-body problem comes in handy.

The Kohn-Sham auxiliary system and electronic band structure

The Kohn-Sham approach proposed in 1965 [9] replaces the original interacting many-body system with an auxiliary system that is easier to solve, i.e. a non-interacting system. This approach makes a key assumption: that the ground state density of the interacting system is equal to that of the auxiliary, non-interacting system. This leads to a more tractable problem where all the interaction terms are buried into another functional of the density called the exchange-correlation functional. Following a variational approach, we obtain the Kohn-Sham equations in the form of independent particle equations:

$$H_{\mathrm{KS}}[n(\mathbf{r})]\psi_i(\mathbf{r}) = \epsilon_i \psi_i(\mathbf{r}) \tag{1.3}$$

where i labels an electron, ϵ are the eigenvalues or Kohn-Sham energies, and ϕ is the Kohn-Sham orbital. Note that the Kohn-Sham eigenvalues and eigenfuctions do not possess physical meaning and thus do not correspond to physical energies or wavefunctions of the system. The Kohn-Sham Hamiltonian is given by:

$$H_{\mathrm{KS}} = -\frac{\hbar^2}{2m_e}\nabla^2 + V^{\mathrm{KS}}(\mathbf{r}) \tag{1.4}$$

Here, V^{KS} includes ionic contributions (V^{ion}), Hartree contribution (V^{H}), and the exchange-correlation potential (V^{xc}) [10]:

$$V^{\mathrm{KS}} = V^{\mathrm{ion}} + V^{\mathrm{H}} + V^{\mathrm{xc}} \tag{1.5}$$

Phonon properties and electron-phonon matrix elements

The interaction of electrons with lattice vibrations is often the most important interaction type, and it is the only type we consider in this thesis. For example, it is well-established that the electron mobility of a defect-free semiconductor near room temperature is limited by interaction with lattice vibrations [11]. We will investigate electron-phonon interactions using DFT as a backbone.

We can obtain the total potential energy of electrons and nuclei in an "infinite" solid with periodic boundary conditions using standard DFT techniques. To study lattice vibrations, we begin by expanding this potential energy in the ionic displacements at second order. This is the harmonic approximation. In this expansion, the second derivatives of the energy with respect to the atomic coordinates define the *interatomic force constants*, and the Fourier transform of the force constants is known as the *dynamical matrix*. Upon diagonalization, we obtain the normal modes of vibration, also known as polarization of the wave. Using creation and annihilation operators one can show that these classical normal modes are related to quanta of lattice vibrations, or phonons [7].

For a 3-dimensional crystal with N=2 atoms in the primitive unit cell, the dynamical matrix is a 6×6 Hermitian matrix. The eigenvalues of the matrix are $3 \times N = 6$ phonon frequencies for each wavevector, corresponding to the 6 polarizations and constituting what is known as the *phonon dispersion* of the crystal. There are three phonon branches known as the acoustic branches, that vanish as $\mathbf{q} \to 0$, while the other 3 branches are known as optical branches.

We have now discussed electronic bands and phonon dispersion of crystals. The last major ingredient we need before discussing how to obtain observables is the electron-phonon matrix element. The electron-phonon matrix element describes the coupling between an electron and a phonon and has the form:

$$g_{mn\nu}(\mathbf{k},\mathbf{q}) = \langle u_{m\mathbf{k}+\mathbf{q}} | \, \Delta_{\mathbf{q}\nu} v^{\mathrm{KS}} \, | u_{n\mathbf{k}} \rangle_{uc} \tag{1.6}$$

where u are Bloch-periodic components of the Kohn-Sham (KS) wave functions, $\Delta_{\mathbf{q}\nu} v^{\mathrm{KS}}$ is the variation in the KS potential due to lattice vibrations experienced by electrons, and the integral is over one unit cell. Here, the KS potential is typically expanded to first order in the atomic displacements to obtain $\Delta_{\mathbf{q}\nu} v^{\mathrm{KS}}$. One approach to obtain the scattering potential $\Delta_{\mathbf{q}\nu} v^{\mathrm{KS}}$ in the DFT framework is to construct a supercell consisting of repeated integer units of the unit cell, displace an atom by a small amount, and calculate the restoring forces on the other atoms. This is known as the *frozen-phonon* method. This method may not be suitable for calculating matrix elements corresponding to long wavelength phonons because the supercell may become too large for computational feasibility [7]. Another approach, which we adopt in this thesis, is using density functional perturbation theory (DFPT) [12], where the dynamical matrices are directly computed at arbitrary phonon momenta. DFPT has the advantage that $\Delta_{\mathbf{q}\nu} v^{\mathrm{KS}}$ can be computed using just the unit cell. Once we obtain the electron-phonon matrix elements, the electron-phonon scattering rates can be derived [7]. They have the form:

$$\begin{aligned}\Gamma_{n\mathbf{k}}(T) = \frac{2\pi}{\hbar N} \sum_{m\nu\mathbf{q}} |g_{mn\nu}(\mathbf{k},\mathbf{q})|^2 \big[&(N_{\nu\mathbf{q}} + 1 - f_{m\mathbf{k}+\mathbf{q}}) \delta(\epsilon_{n\mathbf{k}} - \epsilon_{m\mathbf{k}+\mathbf{q}} - \hbar\omega_{\nu\mathbf{q}}) \\ &+ (N_{\nu\mathbf{q}} + f_{m\mathbf{k}+\mathbf{q}}) \delta(\epsilon_{n\mathbf{k}} - \epsilon_{m\mathbf{k}+\mathbf{q}} - \hbar\omega_{\nu\mathbf{q}}) \big]\end{aligned} \tag{1.7}$$

Here, ϵ are quasiparticle or band energies, $\omega_{\nu\mathbf{q}}$ is the frequency of a phonon with wavevector $\mathbf{q}$ and branch index ν, and f and N are electron and phonon occupation functions that describe the probability that a state is occupied. The relaxation time of a state is the inverse of the scatterig rate, $\tau_{n\mathbf{k}} = (\Gamma_{n\mathbf{k}})^{-1}$

Wannier interpolation

The expression in Eq. 1.7 requires a dense electron and phonon grid in the Brillouin zone, typically ~ 3 orders of magnitude greater than that used in DFT and DFPT calculations. This computational cost is not feasible for DFT calculations, so a typical process is to first calculate the electron and phonon properties on a coarse $\mathbf{k}$ and $\mathbf{q}$ grid, e.g. $10 \times 10 \times 10$, and then interpolate to a fine grid $\sim 100 \times 100 \times 100$. The most widely used scheme, which we also adopt in this work, is Wannier interpolation [13, 14]. Wannier functions are real-space, localized representations of the Bloch states (for example, the Bloch states obtained from a DFT calculation) and provide a physical picture of the bonding characteristics in a system. They can be constructed from a unitary transformation of the initial Bloch states, such that the original Hamiltonian can be expressed in this basis. A Fourier transform back to reciprocal space then yields the desired interpolation onto an arbitrary grid.

Boltzmann transport theory

The Drude model, developed by Paul Drude in 1900 [15], is a simple, classical model that provided a basic framework of understanding the behavior of electrons in metals. Some of the key features of the model include the incorporation of scattering mechanisms with ions that limit the conductivity of the material, an assumption of free electrons moving in straight lines between collisions, and neglect of electron-electron and electron-ion interactions (except for collisions). The electrical mobility in the Drude model is given as:

$$\mu = \frac{e\tau}{m} \tag{1.8}$$

where τ is a phenomenological relaxation time, e is the elementary charge and m is the electron effective mass. Since Drude, significant progress has been made to develop more sophisticated transport models that capture important physical processes in materials. Following the advent of DFT and DFPT, some of the earliest *ab initio* studies on electron mobility employed the Boltzmann Transport Equation (BTE) with varying approximations [16, 17, 18, 19]. The BTE describes the evolution of the distribution function of a particle in the presence of an external field. Boltzmann initially formulated the equation for dilute gases, where the motion of individual gas molecules is governed by collisions with other molecules. He considered the probability distribution of particles in both position and momentum space. The key idea in Boltzmann's work was the consideration of particle collisions, which lead to changes in momentum and position. He introduced the concept of a collision integral to describe how quasiparticles change their momentum due to interactions. Boltzmann's initial work was focused on gases, but the equation could be extended to describe the behavior of particles in a solid. In this case, quasiparticles are typically electrons, and the collisions are often due to interactions with other electrons, lattice vibrations (phonons), and impurities.

The distribution function of an electron $f(\mathbf{r}, \mathbf{k}, t)$ is the probability that it has wave vector $\mathbf{k}$ at time t and position $\mathbf{r}$. We can start by assuming that the rate of change of $f(\mathbf{r}, \mathbf{k}, t)$ can be written as:

$$\frac{\partial f(\mathbf{r}, \mathbf{k}, t)}{\partial t} = \left(\frac{\partial f}{\partial t}\right)_{\text{drift}} + \left(\frac{\partial f}{\partial t}\right)_{\text{coll}} \tag{1.9}$$

where the drift term captures the effect of external forces and the collision term (coll) captures internal collision processes. One assumption in Eq. 1.9 is that the external field does not couple directly with collisions in the system, an assumption that could be invalid in cases of very strong external fields or strong collisions. The drift term may be obtained by considering the distribution of particles in a small phase space volume $d\mathbf{k}d\mathbf{r}$ drifting to a nearby small volume $d\mathbf{k}'d\mathbf{r}'$ in a time Δt [20]:

$$\left(\frac{\partial f}{\partial t}\right)_{\text{drift}} = -\left[\frac{\partial f}{\partial \mathbf{k}} \cdot \frac{1}{\hbar}\left(e\mathcal{E} + \mathbf{v} \times \mathbf{B}\right) + \frac{\partial f}{\partial \mathbf{r}} \cdot \mathbf{v}\right] \tag{1.10}$$

Here, $\mathcal{E}$ and $\mathbf{B}$ represent applied electric and magnetic fields, respectively, $\mathbf{v} = \frac{d\mathbf{r}}{dt}$ is the time rate of change of $\mathbf{r}$. The collision term describes the effects of collision or scattering processes on $f(\mathbf{r}, \mathbf{k}, t)$ and can be derived using Fermi's Golden Rule. This term will be discussed in more detail in Chapter 3. The BTE we are interested in solving is therefore:

$$\frac{\partial f}{\partial t} + \frac{\partial f}{\partial \mathbf{r}} \cdot \mathbf{v} + \frac{\partial f}{\partial \mathbf{k}} \cdot \frac{1}{\hbar}\Big(e\mathcal{E} + \mathbf{v} \times \mathbf{B}\Big) = \left(\frac{\partial f}{\partial t}\right)_{\text{coll}} \tag{1.11}$$

The second term on the left hand side of this equation describes diffusion, and the third term captures effects of the applied external fields. Solution of Eq. 1.11 for $f(\mathbf{r}, \mathbf{k}, t)$ leads us to several transport coefficients which are Brillouin zone integrals of $f(\mathbf{r}, \mathbf{k}, t)$. Further, some of the coefficients we are interested in (e.g. electrical conductivity) are steady-state properties, so we can often ignore the time derivative in Eq. 1.11. The primary difficulty of the BTE arises from the collision term which ideally should include all relevant scattering processes in the material.

1.3 Outline of thesis

In Chapter 2, we give an introduction to the principles of operation of HEMTs, describe its characteristics, important figures of merit, noise sources and review previous explanations of the physical origin of noise in these devices. We then propose a new theory of drain noise in HEMTs as a type of partition noise arising from real-space transfer of hot electrons from the channel to the barrier. The theory accounts for the magnitude and dependencies of the drain temperature and suggests strategies to realize devices with lower noise figure.

In Chapter 3, we give an overview of the numerical methods we adapted to solve the BTE, and apply this *ab initio* method to investigate two-phonon electron and hole scattering processes in boron arsenide. We find that inclusion of these higher-order processes reduces the computed room-temperature electron and hole mobility in BAs by around 40% from the one-phonon value, resulting in an underestimate of experimental values by a similar percentage. We discuss the apparent disagreement between our results and experiment and suggest an experimental approach to test our predictions using luminescence spectroscopy.

Motivated by our results in Chapter 3, we quantify the effect of phonon drag on the electron mobility in boron arsenide – an effect that coulld possibly overestimate the obtained mobility from recent experiments. We find that at carrier densities that these experiments are performed, the drag contribution to the mobility is around 25% and could be partially responsible for the disagreement of our two-phonon results with experiment.

Chapter 2

THEORY OF DRAIN NOISE IN HIGH ELECTRON MOBILITY TRANSISTORS BASED ON REAL-SPACE TRANSFER

This chapter has been adapted, in part, from:

> Iretomiwa Esho, Alexander Y. Choi, and Austin J. Minnich. Theory of drain noise in high electron mobility transistors based on real-space transfer. Journal of Applied Physics 131.8 (2022).

Low noise microwave amplifiers based on HEMTs are widely used in scientific applications ranging from radio astronomy [21] to quantum computing [22, 23]. Decades of progress in device fabrication have yielded significant advances in figures of merit such as transconductance [24, 25, 26], gain [27], unity gain cutoff frequency [28, 29, 30], maximum oscillation frequency [31], and power consumption [32, 33, 34].

A HEMT utilizes an interface between two materials of different band gaps as the channel. The wide band gap material is doped, thus resulting in the transfer of electrons from the wide band gap material to the conduction band of the lower band gap material to occupy lower energy states [35]. These electrons are confined in a potential well and form the two dimensional electron gas (2DEG). The 2DEG exhibits higher electron mobility as compared with the electrons in the doped channel of the MOSFET because of reduced ionized impurity scattering by the dopants. HEMTs typically have channel mobilities around 10^4 cm^2 V^{-1} s^{-1} at room temperature (and 10^5 cm^2 V^{-1} s^{-1} at cryogenic temperatures) and a typical dopant concentration of 10^{19} cm $^{-3}$, compared to Si MOSFETs at 10^3 cm^2 V^{-1} s^{-1} [36, 37].

The basic layout of a HEMT is shown in Fig. 2.1. The HEMT is usually grown by metalorganic chemical vapor deposition (MOCVD) or molecular-beam epitaxy (MBE). In MOCVD, growth of crystalline layers is by chemical reaction in a chamber, leading to deposition of materials on a substrate. In molecular-beam epitaxy, beams are directed in an ultra-high vacuum environment at a substrate where they react to create the required layers.

The HEMT is grown on a substrate material such as GaAs, SiC, or InP. A

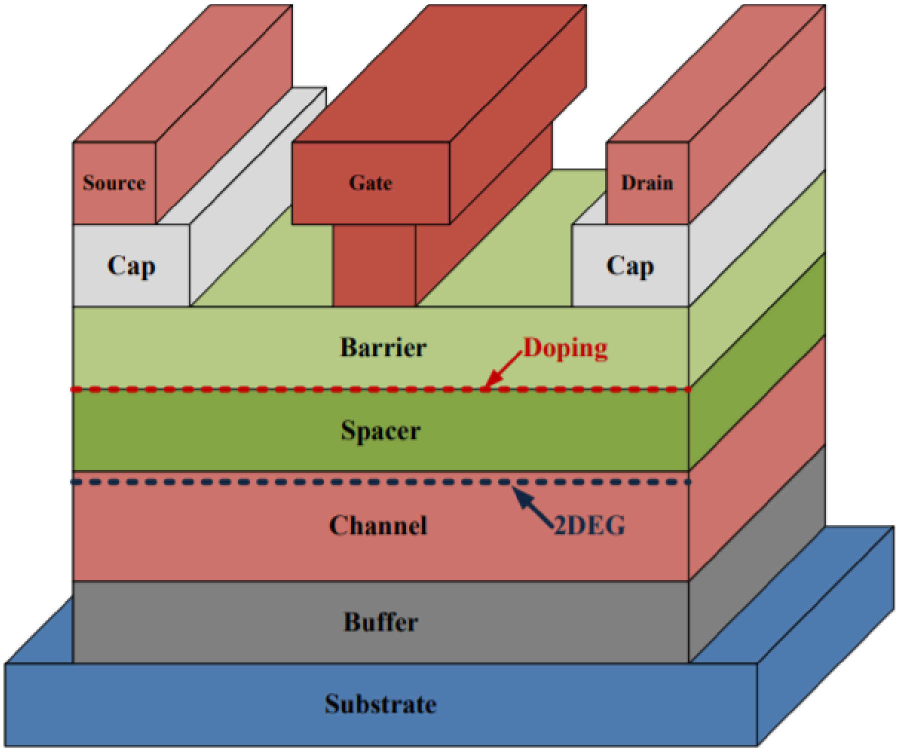

Figure 2.1: Epitaxial structure of a HEMT showing the material layers, metallic contacts, and locations of the delta doping layer and 2DEG. The barrier consists of a thin, delta-doped layer of donor electrons that migrate to the channel and form the quantum well. There is a spacer between the barrier and channel that physically isolates the conduction electrons in the channel from the ionized dopants in the barrier which acts to reduce impurity scattering and enhances the mobility. Figure adapted from [38].

buffer is introduced between substrate and channel to mitigate effects of lattice mismatch such as cracks and dislocations between substrate and channel. The buffer is typically a few hundred nanometers thick. The channel, about 15 nm thick, is the lower band gap material, and a $3 - 10$ nm spacer layer is typically introduced between the channel and the higher band gap material (barrier) to separate the 2DEG from ionized donors, thereby reducing ionized impurity scattering. A thinner spacer layer increases sheet charge density but also reduces electron mobility due to impurity scattering. A thicker layer improves electron mobility but reduces electron density in the channel. The barrier is usually 10 - 30 nm. Introducing the dopants as a delta layer in the transistor has several advantages including reduced gate-to-channel distance, high carrier density, and enhanced breakdown voltage [39]. The cap layer is highly doped ($10^{18} - 10^{19}$ cm^{-3}) to reduce the source and drain contact resistances. Additionally, it protects the barrier surface from oxidation.

The source, drain, and gate contacts provide a mechanism to control the flow of electrons from source to drain. The source contact is typically grounded, and a positive bias is applied to the drain contact. This positive bias induces electron flow from source to drain. The gate is a Schottky contact that modulates electron concentration in the channel by shrinking the depletion region under the gate or extending it into the channel.

HEMTs are depletion mode devices: current flows when the drain is biased with respect to the source even if there is no voltage applied to the gate. This is a consequence of electron transfer forming the channel when dissimilar bandgap materials are brought together, in contrast to enhancement mode devices like the MOSFET where a threshold gate voltage is needed to form the channel.

DC and RF characteristics

As with the MOSFET, the drain current increases with drain voltage (linear regime) up until a certain voltage where it saturates (saturation regime). This saturation is caused by a restriction on further heating of electrons as they emit optical phonons. In reality, certain mechanisms such as impact ionization and presence of traps can cause the current to continue increasing beyond the linear regime [40, 41, 42, 43]. The drain current also increases as the gate voltage increases, up to a voltage where it saturates, corresponding to the channel being completely undepleted. Figure 2.2 shows current-voltage characteristics of an InGaAs channel HEMT at various temperatures. In Fig. 2.2 we notice that the drain current shows an initial linear increase with the drain voltage before it appears to reach a point of saturation, at which instead of saturation, there is a noticeable kink.

There are a number of important electrical characteristics used to evaluate the performance of transistors, including the transconductance g_m, output conductance g_o, current gain h_{21}, and current gain cut-off frequency f_T. Transconductance is defined as:

$$g_m = \left.\frac{\partial I_D}{\partial V_{GS}}\right|_{V_{DS}} \tag{2.1}$$

Transconductance is a measure of the change in output (drain) current with respect to a change in input (gate) voltage.

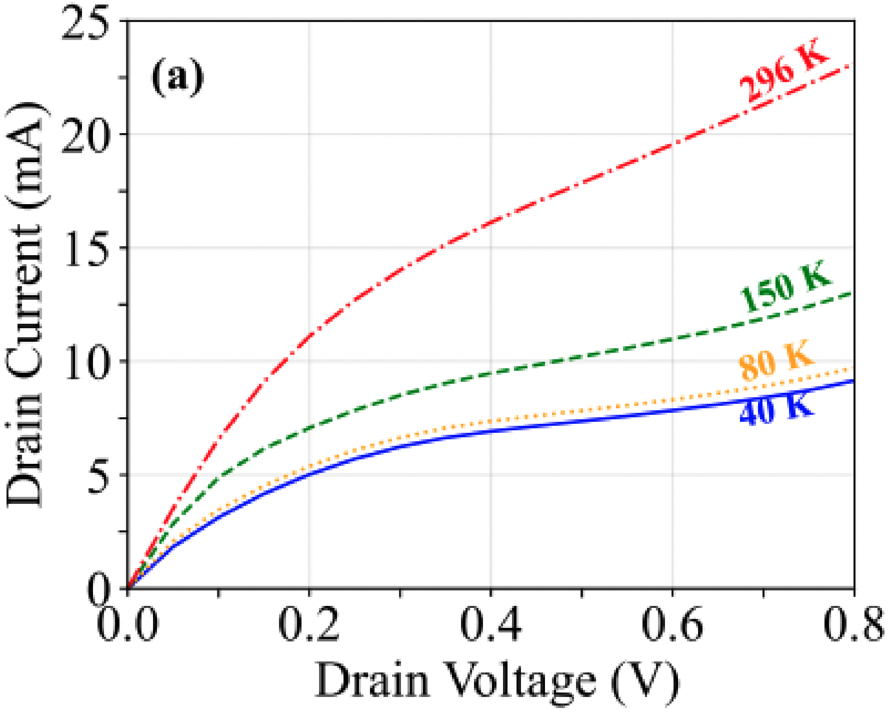

Figure 2.2: DC IV characteristics of a GaAs HEMT at different temperatures with an applied gate-source voltage $V_{GS} = -0.2$ V. The current initially increases linearly with voltage and then approaches saturation due to optical phonon emission. The observed kink is likely due to impact ionization or presence of traps. Data obtained from Bekari Gabritchidze and used with permission.

The output conductance g_{ds} measures the variation of drain current with respect to variations in drain voltage. It is defined as

$$g_{ds} = \left.\frac{\partial I_D}{\partial V_{DS}}\right|_{V_{GS}} \tag{2.2}$$

Ideally, $g_{ds} = 0$ in saturation since the drain current does not depend on drain voltage in this regime.

The current gain h_{21} mentioned above refers to the small-signal current gain, that is, i_d/i_g when an additional small-signal voltage is applied to the gate, where i_d and i_g are the small-signal drain current and small-signal gate current, respectively. h_{21} is given by

$$h_{21} = \frac{g_m}{j\omega C_{gsi}} \tag{2.3}$$

C_{gsi} is the intrinsic gate-source capacitance. As the frequency ω of the input signal increases, the gate current increases, and at a certain frequency, the gate current equals the drain current. This is because the impedance from the capacitor becomes small relative to the gate resistance as ω gets large enough. The current gain cut-off frequency, f_T, is defined as the frequency at which the small-signal current gain becomes unity.

$$f_T = \frac{g_m}{2\pi C_{gsi}} \tag{2.4}$$

f_T is a widely used figure of merit because it provides an indication of the high frequency behavior of transistors. State–of–the–art InGaAs channel HEMTs with $f_T > 600$ GHz have been reported [44, 45].

Noise measurements

For low noise applications, it is important to accurately determine how much noise a device adds to an input signal. The noise figure of a device is a figure of merit that quantifies how much the signal to noise ratio of a signal is degraded. One can imagine a device with gain G and a signal to noise ratio (SNR) at the input $\mathrm{SNR}_i = S_i/N_i$ where a signal S_i is applied at the input and N_i is the input noise. We know that the output signal $S_o = S_i G$, therefore the signal to noise ratio at the output is $\mathrm{SNR}_o = S_i G/N_o$ with N_o being the output noise. The noise factor is defined as the ratio of these quantities. That is,

$$F = \frac{\mathrm{SNR}_i}{\mathrm{SNR}_o} = \frac{N_o}{N_i G} \tag{2.5}$$

The noise figure is defined as

$$\mathrm{NF} = 10\log_{10}\frac{\mathrm{SNR}_i}{\mathrm{SNR}_o} = \mathrm{SNR}_{i,\mathrm{dB}} - \mathrm{SNR}_{o,\mathrm{dB}} \tag{2.6}$$

The noise figure is usually measured with a spectrum analyzer using the Y-factor technique. In this technique, one uses a noise source with two temperature states. The high temperature state has the higher output noise power and the low temperature state, the reduced noise output. For each of the noise input states, the noise source is applied to the device input and the noise power at output measured. The noise figure of the device is then calculated from these measurements. The Y factor term is defined as the ratio of the measured noise output power at the high temperature state to the noise output power at the low temperature state. If G remains constant for these two states, the device noise temperature can be expressed as [46]:

$$T_N = \frac{T^{\mathrm{ON}}_{\mathrm{source}} - Y T^{\mathrm{OFF}}_{\mathrm{source}}}{Y-1} \tag{2.7}$$

Strictly speaking, the noise obtained through this procedure is the total system noise temperature, including the device noise contribution as well as the measurement system's contribution. Since we are typically interested in the device's noise temperature, a correction must be applied to isolate its contribution. This correction is done with a cascaded noise factor equation [46], resulting in an expression for the actual device temperature of the form:

$$T_{N,1} = T_N - \frac{T_{N,2}}{G_1} \tag{2.8}$$

where $T_{N,2}$ is the noise temperature of the measurement system and $T_{N,1}$ is the corrected device noise temperature. It is clear from Eq. 2.8 that if device gain G_1 is high, the measurement system's contribution to Eq. 2.7 will be minimal.

2.1 Noise sources in a HEMT

There are several potential sources of noise when operating a HEMT device or amplifier. Some of these are thermal noise, hot electron noise, flicker (1/f) noise, thermal noise, and generation-recombination (G-R) noise. Flicker noise is associated with traps and defects and has an inverse frequency dependence, which is why it is also known as $1/f$ noise. As one may expect, this type of noise becomes less important at high frequencies. G-R noise is related to trap-assisted capture and emission of electrons and is only an important source of noise for frequencies less than 10 MHz [47]. The dominant noise sources across various frequency ranges are shown schematically in Fig. 2.3. For microwave frequencies, the important noise mechanisms are hot electron noise, thermal noise, and shot noise. We discuss each of these in turn.

Hot electron noise

The term "hot electron" refers to an electron gas temperature that is higher than that of the lattice. In transistors, this high temperature state is usually a result of high electric fields that can be achieved by the application of a source-drain voltage on the order of 1 V for a typical source-drain distance of $\sim 1\ \mu$m. The observed current fluctuation associated with the hot electron gas is known as hot electron noise. Hot electron noise can be a result of

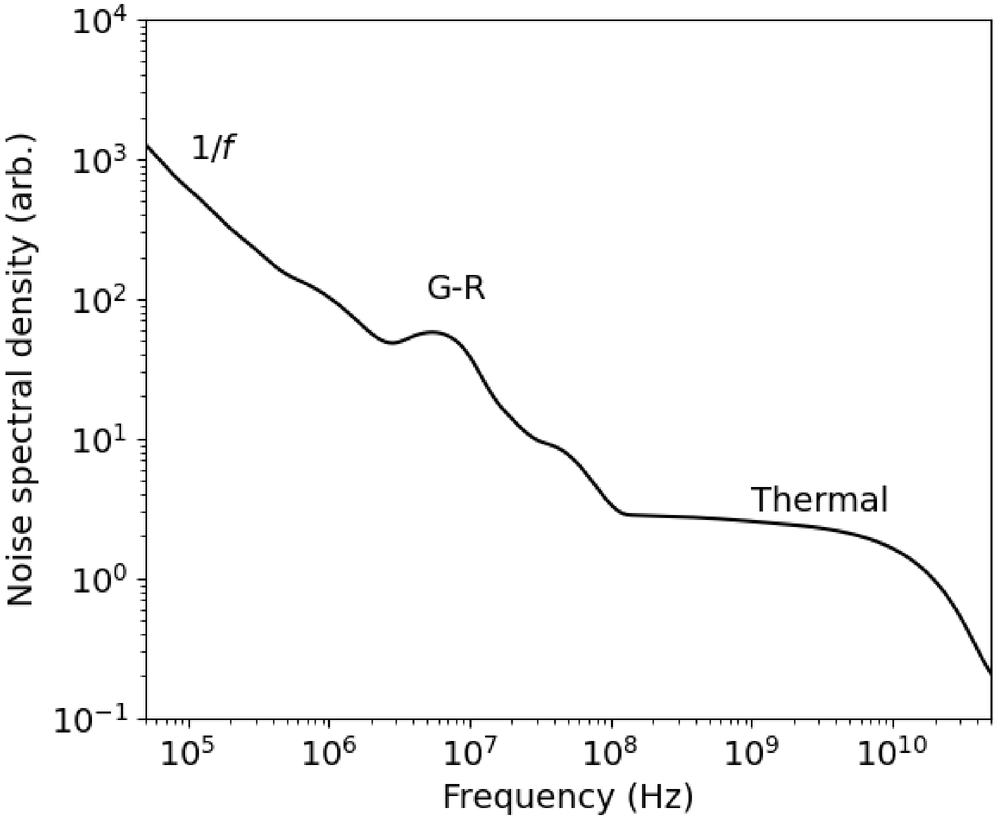

Figure 2.3: Schematic showing primary noise sources across frequency ranges. $1/f$ flicker noise is typically dominant in the sub-MHz range, while generation-recombination noise is dominant in the sub-GHz range. Noise sources that are thermal in nature and lead to carrier velocity fluctuations tend to be dominant for frequencies greater than 1 GHz. Figure adapted from [47].

intervalley processes in multi-valley semiconductors [48] and/or an analogous process known as real-space transfer (RST) where electrons are excited out of a confined quantum well into an adjacent layer.

Thermal noise

The random motion of electrons in an electrical conductor due their thermal energy is known as thermal noise [49, 50], and is one of the most important noise sources in devices. This noise mechanism is also known as Johnson-Nyquist noise. The corresponding power spectral density is: [51]:

$$\overline{v_n^2} = 4k_B T R \Delta f \tag{2.9}$$

where k_B is Boltzmann's constant, T is the physical temperature of the device, R is the resistor value, and Δf is the bandwidth. Thermal noise is proportional to physical temperature, and for this reason, electronic devices are cooled to cryogenic temperatures to achieve better noise performance. Note that a HEMT can be modeled as a single noisy resistor - in this case the temperature T will represent an elevated characteristic noise temperature, equivalent to the noise temperature in Eq. 2.7.

Shot noise

Shot noise is a type of noise that arises due to the fact that charge is quantized, and is a quantification of the statistical nature of the arrival of electrons at a terminal. The shot noise spectrum is:

$$\overline{i^2} = 2qI\Delta f \tag{2.10}$$

where q is electronic charge and I is current. Shot noise occurs when there is a need for a DC current to traverse a potential barrier, and the stochastic or random nature of this traversal is what gives rise to shot noise.

2.2 Experimental characterization of noise parameters

Determination of the noise parameters of a HEMT requires a small-signal model. A small-signal model is a simple representation of an electronic circuit that is used to analyze its behavior under small variations around a specific operating point, and can provide valuable information about device parameters, including but not limited to resistances, capacitances, and noise parameters.

Small signal models are typically made up of intrinsic and extrinsic components. Parasitic effects specifically related to the drain, gate, and source contacts are accounted for by the extrinsic component. These parasitic effects are categorized into capacitances, inductances, and resistances. On the other hand, the intrinsic component represents the HEMT's active region. It is dependent on the biasing conditions and can also be categorized into capacitances, resistances, conductances, and a transit time. In context of this thesis, we will narrow our attention to only a subset of these parameters. An important intrinsic parameter is the channel resistance, R_{ds}. This is the resistance of the channel under the gate and can be alternatively represented as the inverse of the output conductance in Eq. 2.2. Another important parameter is the gate-source capacitance, C_{gs}. This is the capacitance formed by the gate towards the source side and the 2DEG. Note that because this capacitance is directly related to the depletion layer under the gate, it is also known as depletion capacitance. The gate-drain capacitance C_{gd} is the capacitance formed by the gate towards the drain side and the 2DEG. Similarly, the gate-source resistance is represented as R_{gs}. These and other parameters can either be extracted directly or though an optimization procedure. Direct extraction requires obtaining the voltage dependence of HEMT scattering parameters (S-parameters) to obtain the intrinsic parameters, and a de-embedding process to obtain the extrinsic parameters. More details of this type of procedure are given in Refs. [52]. After acquiring the intrinsic and extrinsic parameters, we can proceed with modeling to obtain the noise parameters.

2.3 Pospieszalski's noise model

HEMT noise can be modeled with a two-port network with voltage (v_n) and current (i_n) noise sources added at the input gate terminal of the transistor, with no correlation assumed between these noise sources. A schematic of this two port network is shown in Fig. 2.4. The most widely adopted scheme to obtain the noise parameters of a HEMT based on a noisy two port network is the Pospieszalski model [6]. In this model, uncorrelated thermal voltage and noise sources are assigned to the intrinsic resistive elements of the HEMT, and are related to the equivalent physical temperatures of the resistors. The output conductance g_{ds}, with a physical temperature represented as the drain temperature T_d, is the only unknown parameter and thus is a fitting parameter. An equivalent gate temperature T_g is assigned to the resistive element R_{gs}. The minimum noise temperature of the device can thus be expressed in terms of the intrinsic parameters as [6]:

$$T_{min} = 2\frac{f}{f_T}\sqrt{g_{ds}R_{gs}T_gT_d + \left(\frac{f}{f_T}\right)^2 \cdot R_{gs}^2 g_{ds}^2 T_d^2 + 2\left(\frac{f}{f_T}\right)^2 \cdot R_{gs}g_{ds}T_d} \qquad (2.11)$$

In this expression, T_g is closely related to the gate temperature and is typically assumed to be equal to the ambient temperature. Therefore, all parameters in Eq. 2.11 are known except T_d, which can be obtained through a fitting procedure. Nonetheless, given that T_d is merely a parameter used for fitting,

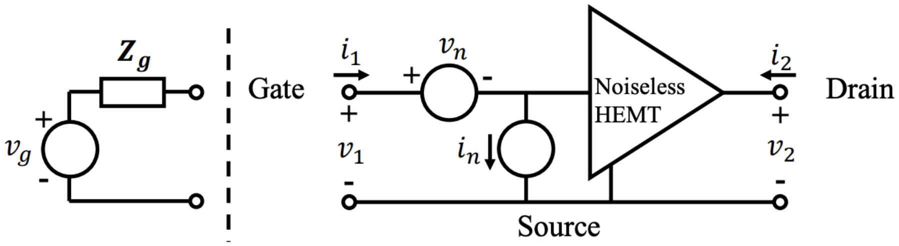

Figure 2.4: Noisy two port representation of a HEMT composed of a noiseless HEMT with added external noise sources v_n and i_n.

it raises the question of its physical origin, an answer which would eventually pave way for devices with better noise performance.

2.4 Previous explanations of the origin of T_d

Generation of dipole layers

The physical origin of the drain noise, T_d, is still up for debate, but there have been several proposed theories. One explanation given by Statz and colleagues [53] interprets drain noise in the saturation regime as arising from the generation of dipole layers that end up drifting to the drain contact. We start from the expression of the basic noise current density source given by Shockley and van der Ziel [54, 55, 56]:

$$\overline{J_n(x)J_n(x')} = \frac{4q^2Dn\Delta f}{A}\delta(x-x') \tag{2.12}$$

where J_n is the noise current density at x, D is the high field diffusion coefficient, n is the carrier density, and A is the cross-sectional area. Assuming that the noise current may be interpreted as a distribution of mutually uncorrelated spatial and time impulses, Eq. 2.12 may be written for the autocorrelation of the current density at point x as:

$$\overline{(AJ_n(x))^2} = \frac{4q^2DnA\Delta f}{\Delta x} \tag{2.13}$$

Note that we have substituted $\delta(x-x') = 1/\Delta x$ for $x = x'$. One then draws a comparison with the shot noise spectrum given in Eq. 2.10. For shot noise, current impulses occur at a rate I/q. In Eq. 2.13, one may follow a similar interpretation and conclude that it represents a sequence of current impulses occurring at the rate:

$$r = \frac{2DnA}{\Delta x} \tag{2.14}$$

The authors then describe this as each of the current impulses result in a displacement of charge q over a distance Δx, and thus the formation of a dipole layer of strength $q\Delta x/A$. Further, they say that since these impulses occur in the saturated regime, the dipole layers drift unchanged to the drain contact and conclude that the spontaneous generation of these dipole layers can be identified as the source of drain noise.

Suppressed shot noise

More recently, drain noise in HEMTs and field effect transistors (FETs) in general has been attributed to a suppressed shot noise mechanism [57]. The justification for this attribution is based on the fact that shot noise is proportional to current and experimentally, T_d is known to be proportional to the drain current. The drain current noise spectrum is then represented in a shot noise form as:

$$\overline{i_{ds}^2} = 4k_B T_d g_{ds} \Delta f = 2FqI_d \Delta f \tag{2.15}$$

where I_d is drain current and F is a shot noise suppression factor and is known as the Fano factor. It was posited that in the limit of very short gate lengths, F approaches 1 and drain noise becomes a pure shot noise mechanism arising from ballistic transport, but for typical FETs, $F \sim 0.1$, suggestive of quasi-ballistic transport. A few issues arise with this theory. First, one requirement for this interpretation to be physically correct is that F be independent of device bias (the shot noise dependence on bias is already captured in I_d of Eq. 2.15) and ambient temperature. However, a few studies have reported a dependence of T_d on physical temperature and bias [58, 59, 60], although the dependence on physical temperature is disputed [61]. Furthermore, it is well-established that electrons undergo sufficient disruptive electron-electron and electron-phonon collisions [62, 63] as they travel from source to drain to call into question the physical picture of quasi-ballistic transport in a HEMT.

2.5 Real-space transfer and drain noise

None of the previous explanations of drain noise discussed above have been widely accepted or confirmed experimentally. The explanation based on gen-

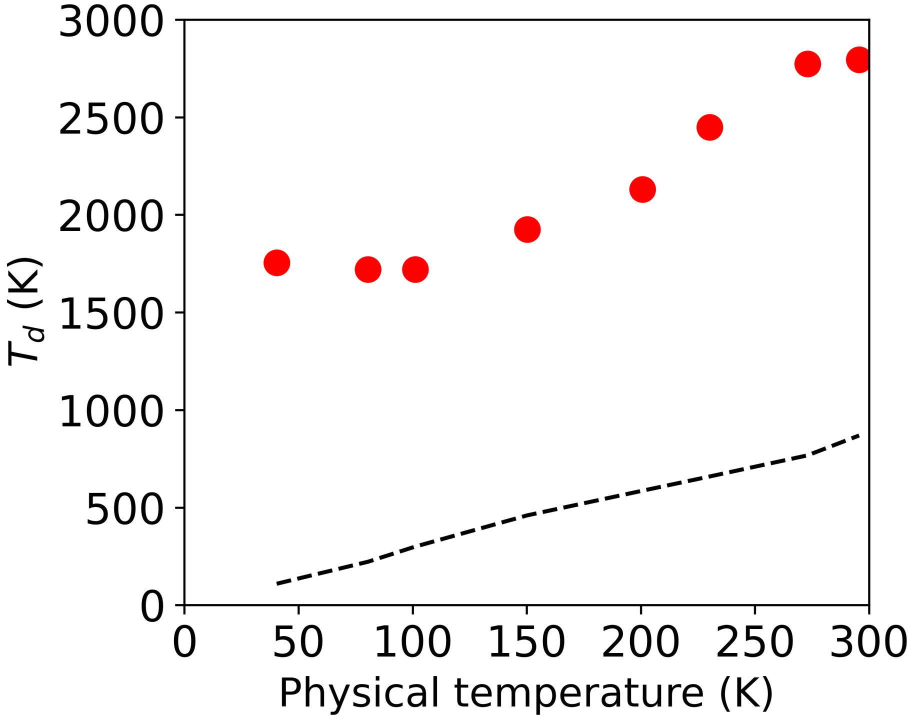

Figure 2.5: Drain noise temperature versus physical temperature showing the contribution from the channel thermal noise. This figure indicates there is another source of drain noise in addition to the thermal contribution. Figure obtained from Ref. [64].

eration of dipole layers is difficult to confirm experimentally while the explanation based on a suppressed shot noise mechanism is inconsistent with the modern understanding of hot electron transport in semiconductor materials. A starting point towards determining the mechanism behind drain noise is to first account for the thermal noise contribution that arises from the conductance of the HEMT channel. Should thermal noise predominantly contribute to the drain noise magnitude, an additional mechanism need not be considered. Figure 2.5 is a plot of the drain noise temperature T_d versus physical temperature, obtained from Ref. [64]. The trend in this figure indicates that the channel thermal noise contribution is not sufficient to explain the magnitude of T_d, and another mechanism should be primarily responsible for the magnitude of the drain noise.

To determine this additional mechanism, we recognize that there exists a large body of work that extensively investigated high-field transport [65, 66, 67], energy relaxation [68, 69, 70, 62, 71, 63, 72], microwave noise [73, 74], and related properties in 2D quantum wells [75, 76, 77, 78, 79]. The physical picture of high-field transport obtained from these studies is that electrons are heated by the electric field and lose energy primarily by optical phonon emission. Photoluminescence experiments provide evidence that electrons heated by the field scatter rapidly enough with each other to maintain a distribution characterized by a temperature that is higher than the lattice temperature [66]. If the electron temperature is sufficiently high, electrons may thermionically emit over the confining potential at the heterointerface between channel and barrier and thereby leave the channel in a process known as real-space transfer (RST). This process was originally proposed as a means to realize heterostructure devices exhibiting negative differential resistance (NDR), where the NDR originates from an increased electron population in the lower mobility barrier layer as the drain voltage is increased [80]. Devices exploiting the effect, such as charge injection transistors [81] and negative resistance field effect transistors [82], were reported shortly thereafter. RST has also been observed in HEMTs under forward gate bias and high drain voltage [83, 84].

Observing NDR in a HEMT requires a non-negligible fraction of channel electrons to emit into the low-mobility barrier layer. However, even if RST is not evident in current-voltage characteristics, it may contribute to microwave noise as a type of partition noise between two dissimilar current paths, similar to intervalley noise [85, 86]. Microwave noise in semiconductor quantum wells and devices has been previously attributed to RST. For instance, Aninkevicius *et al.* concluded that RST was the origin of noise in an AlGaAs/GaAs heterostructure at 80 K based on the measured dependencies of noise temperature on electric field and conduction band offset, and they further attributed intervalley noise suppression to RST at high fields [73]. In HEMTs, Feng *et al.* attributed drain noise partially to RST [87], although evidence supporting the claim was not provided. Other works reported on a RST process dominating low frequency noise characteristics of AlGaAs/InGaAs HEMTs [88]. Monte Carlo simulations have reported RST to affect the transit time [89] and contribute to gate noise [90]. Despite these prior studies in which noise in HEMTs was attributed to RST, a systematic examination of whether RST can account for the reported magnitude and trend of microwave drain noise in the context of the Pospieszalski model is lacking.

2.6 Theory

Consider a two-dimensional electron gas (2DEG) with an applied longitudinal electric field between the source and drain contacts such that electrons flow from source to drain. We may focus only on the region under the gate by incorporating the other regions as access resistances [91]. At the low-noise bias $V_{GS} \sim -0.1$ V, the channel is pinched off, leading to an electric field with peak value ~ 100 kV cm^{-1} [92] under the drain side of the gate to maintain the current of around tens of mA mm^{-1} [93]. The electric field heats the electrons to a temperature that may be sufficient for electrons to thermionically emit out of the channel; if so, current will flow through both the channel and the barrier to the drain contact. The barrier is typically of much lower mobility than the channel owing to ionized impurity scattering by the dopants, and therefore NDR will result from RST if a sufficiently large fraction of electrons transfer to the barrier.

Even if no changes in the $I_{DS}-V_{DS}$ characteristics due to RST can be detected, non-negligible current noise may still be generated by RST. The generated noise can be viewed as a type of partition noise owing to the different mobilities of the channel and barrier. As given in Eq. 4.21 of Ref. [67], the spectral noise power of this mechanism can be expressed in terms of frequency ω and electric field $\mathcal{E}$ by:

$$S_j(\omega, \mathcal{E}) = \frac{4e^2 n_1 n_2 (v_{d1} - v_{d2})^2 \tau}{V_0 n (1 + \omega\tau)^2} \tag{2.16}$$

where τ is the characteristic time for electrons to transfer from channel to barrier; n_1, n_2, v_{d1}, and v_{d2} are average carrier concentrations and velocity in the channel (index 1) and barrier (index 2), respectively; $n = n_1 + n_2$; and V_0 is the 2DEG volume.

Equation 2.16 can be simplified further with the following considerations. First, we take $n_2 \ll n_1$ because NDR is not observed at the low-noise bias, constraining the maximum magnitude of n_2. Second, $v_{d2} \ll v_{d1}$ since the spacer mobility is much less than the channel mobility. Finally, $\omega\tau \ll 1$ in microwave applications so that Eq. 2.16 becomes:

$$S_j(\mathcal{E}) = \frac{4e^2 n_2 v_{d1}^2 \tau}{V_0} \tag{2.17}$$

Let $V_0 = LWd$, where W and d are the gate width and 2DEG thickness, respectively, and L is a characteristic length over which electrons are hot enough to undergo RST. To facilitate comparison with the Pospieszalski model, we note that the spectral density of current fluctuations (S_I) is related to that of current density fluctuations (S_j) as $S_I = A^2 S_j$ where $A = Wd$. Then, S_I can be expressed as:

$$S_I(\mathcal{E}) = \frac{4e^2 n_{s2} v_{d1}^2 W \tau}{L} \tag{2.18}$$

where $n_{s2} = dn_2$ is the barrier sheet density and we have assumed that d is on the order of the barrier thickness.

This partition noise is added at the output of the HEMT. In the Pospieszalski model, the output spectral noise power $S_I = 4k_B T_d g_{DS}$ is parametrized by a drain temperature, T_d, of the drain conductance g_{DS}. To connect Eq. 2.18 to the Pospieszalski model, we equate the spectral noise powers and solve for T_d. A simple expression for the drain temperature can then be obtained as:

$$T_d = \frac{e^2 v_{d1}^2 n_{s2} \tau}{k_B g'_{DS} L} \tag{2.19}$$

where $g'_{DS} = g_{DS}/W$ is the drain conductance per width. From Eq. 2.19, T_d is observed to depend on n_{s2}, showing a direct relationship between the fraction of electrons transferred into the barrier and T_d. n_{s2} in turn depends on the electron temperature, the conduction band offset between channel and barrier, and the probability for a hot electron to emit out of the channel. We note that T_d should be regarded as the additional noise contribution from RST over that contributed by the channel resistance which could be computed using the methods of Ref. [94].

2.7 Results

We assess the validity of the theory by first presenting experimental evidence of the RST process in modern HEMTs at cryogenic temperatures. Current-voltage characteristics of an InP HEMT studied in Ref. [29] were measured at 5 K. The data, courtesy of Junjie Li and Jan Grahn at Chalmers University of Technology, are shown in Figure 2.6a for -0.42 V $\leq V_{GS} \leq 1.14$ V. Typical $I-V$ curves are observed for most values of V_{GS}, including those corresponding

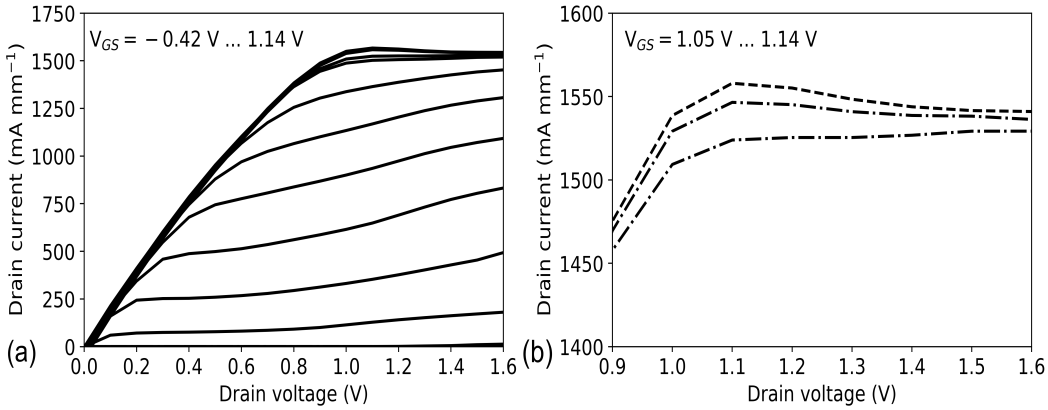

Figure 2.6: Current-voltage characteristics of a HEMT illustrating negative differential resistance (NDR). (a) $I_{DS} - V_{DS}$ characteristics of a 2 × 100 μm gate width, 150 nm gate length InP HEMT at 5 K for several V_{GS}. (b) Magnified view of current-voltage characteristics in (a) under forward bias. NDR is observed for $V_{GS} \gtrsim 1.05$ V and $V_{DS} \gtrsim 1.1$ V. Data courtesy of Junjie Li and Jan Grahn, Chalmers University of Technology.

to depletion ($V_{GS} \lesssim -0.1$ V) at the low noise bias. In particular, a positive output conductance, $g_{DS} > 0$, is observed for $V_{GS} < 1$ V.

As V_{GS} increases above 1 V for $V_{DS} \gtrsim 1.1$ V, $g_{DS} < 0$ is observed. A magnified view of these characteristics is shown in Fig. 2.6b, in which NDR is clearly present. Self-heating can be excluded as the origin as the three curves in Fig. 2.6b differ in dissipated power by only a few percent yet exhibit qualitatively different $I - V$ trends, depending on the value of V_{GS}.

On the other hand, the observed trends qualitatively agree with those reported in prior studies of NDR devices [95, 96, 97] and HEMTs [98, 84] at similar bias. In the case of HEMTs, a negative output conductance at forward gate bias and high $V_{DS} \gtrsim 1$ V was attributed to heating of electrons by the source-drain voltage, leading to increased emission of channel electrons into the barrier and through the gate terminal as V_{DS} increased. As a result, the drain current decreased with increasing V_{DS}, leading to a negative output conductance [98, 84]. The forward-biased gate voltage V_{GS} allows sufficient number of electrons to be emitted into the barrier so that the negative output conductance is observed. Although we have presented measurements on one HEMT in this study, the measurements are in qualitative agreement with trends reported previously [98, 84], suggesting that similar results are observable in HEMTs more generally. These considerations therefore support the hypothesis that RST occurs and could also produce partition noise in modern HEMTs.

We now examine the predictions of the theory and how they compare to the reported magnitude and dependencies of drain noise. First, to estimate the magnitude of T_d from Eq. 2.19, we must specify numerical values of the various parameters. We choose $L \sim 100$ and $g'_{DS} \sim 50$ mS mm^{-1} [93]. The channel-barrier transit time, τ, has been estimated to be on the order of picoseconds by analyzing current reduction in a test structure devised to measure switching and storage effects in GaAs/AlGaAs heterojunctions [99]. Following Eq. 5.15 in Ref. [79], we choose $\tau \sim 1$ ps as a characteristic time for the emission process.

Next, the sheet density in the barrier due to transferred electrons, n_{s2}, is required. This parameter depends on the channel sheet density in the pinched off region under the gate n_{s1}; the hot electron fraction η, or the fraction of electrons that are energetic enough to thermionically emit over the barrier; and the probability for a hot electron to actually emit, γ; as $n_{s2} \equiv \gamma\eta n_{s1}$. The typical sheet density obtained from Hall measurements is $\sim 3 \times 10^{12}$ cm^{-2} [100]. However, the sheet density of relevance to RST is that near the pinchoff region of the gate where the electron temperature is highest. This value can be estimated using the typical current at the low-noise bias and the saturated drift velocity. Monte Carlo simulations have reported the saturated electron velocity to be $v_{d1} \sim 5 \times 10^7 \text{cm}\,\text{s}^{-1}$ for InGaAs HEMTs [101, 102]. Using a value of $I_{DS} \sim 75$ mA mm^{-1}, a typical value at the low-noise bias [93], we obtain $n_{s1} \sim 10^{11}$ cm^{-2}. For simplicity, we assume that all electrons with sufficient energy jump the barrier so that $\gamma = 1$.

The hot electron fraction η is determined by the conduction band offset ΔE_c and V_{GS} for a given electron temperature T_e. This fraction can be obtained using standard theory for the current across a Schottky barrier (see Eq. 61 in Chapter 3 of Ref. [103]) as $\eta = \exp(-(\Delta E_c - qV_{GS})/k_B T_e)$.

Due to the exponential dependence of η on V_{GS}, we neglect the weaker dependence of n_{s1} on V_{GS} in our analysis. To compute η, we must specify T_e in the channel. We obtained a numerical estimate of its magnitude for a 100 nm gate InAlAs/InGaAs HEMT with $V_{DS} = 0.5$ V, $V_{GS} = 0$ V at a lattice temperature of 300 K using Synopsys TCAD to solve the hydrodynamic and Poisson equations in a provided template structure [104]. The result is shown

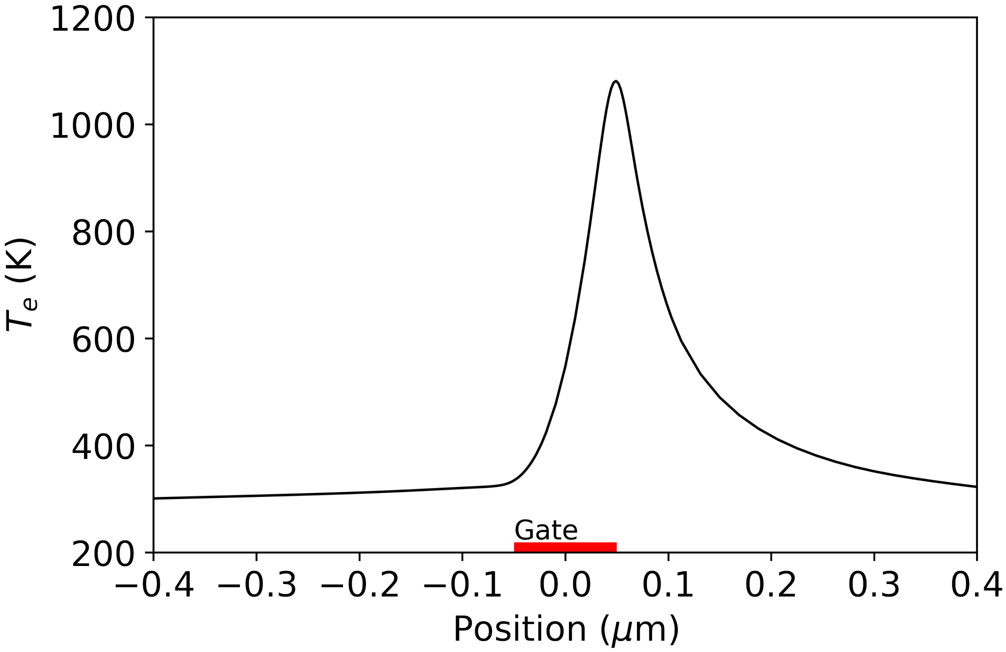

Figure 2.7: Electron temperature T_e versus position along the channel computed using Sentaurus TCAD for $V_{DS} = 0.5$ V, $V_{GS} = 0$ V. T_e peaks at the drain edge of the gate and decreases towards the drain as electrons lose energy by optical phonon emission.

in Fig. 2.7. We observe that T_e equals the lattice temperature at the source, increases to a peak value at the drain side of the gate edge due to heating by the electric field, and decreases towards the drain as electrons lose energy by optical phonon emission. This calculation shows that peak electron temperatures in the HEMT are on the order of 1000 K around the low-noise bias point, although this value could vary by several hundred K depending on the device and bias conditions. With T_e estimated, we can now compute η. For $\Delta E_c \sim 0.5$ eV [91] and $T_e \sim 1000$ K, we find $\eta \sim 0.3\%$.

Using these numerical parameters, we can now use Eq. 2.19 to estimate T_d. We find $T_d \sim 260$ K. This value is of the same order as those reported in modern HEMTs [93, 105]. Due to uncertainties regarding the exact values of the parameters in Eq. 2.19, we note that this value of T_d should be regarded as an order of magnitude estimate rather than a precise value. At a qualitative level, this estimation shows that a relatively small portion of the electron population appears capable of explaining an appreciable portion of the drain noise measured experimentally. At the same time, the effect of RST on mobility would likely not be observable in a HEMT under normal operating conditions due to the small value of η.

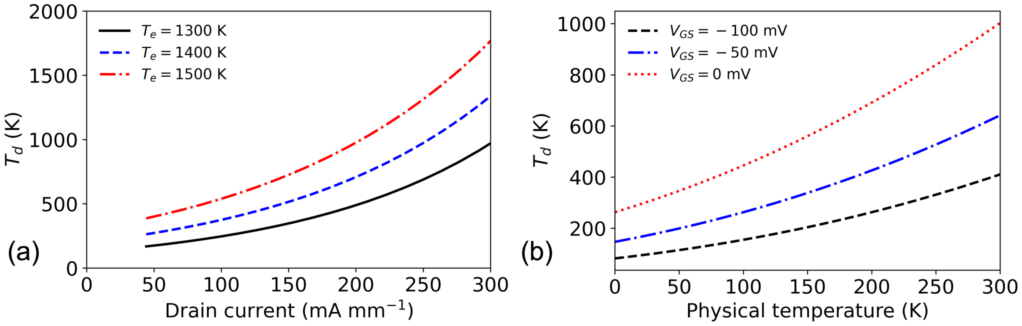

Figure 2.8: Calculation of drain noise temperature. (a) Drain noise temperature T_d versus I_{DS}. Increasing V_{GS} and hence I_{DS} lowers the energy barrier for thermionic emission, leading to higher T_d. Transfer characteristics were obtained from Fig. 4.1 of Ref. [93]. (b) T_d versus physical temperature T for $\Delta T = 1000$ K. The occupation of electronic states above the Fermi energy increases with temperature, and consequently, T_d increases with T as the hot electron fraction η increases.

We now examine the dependencies of T_d predicted from Eq. 2.19. Previous works have reported a dependence of T_d on I_{DS} [21, 105] as well as physical temperature [106, 60, 59]. The present theory predicts a dependence of T_d on V_{GS} since V_{GS} changes the Fermi level of the electrons under the gate, thus altering the population of hot electrons able to thermionically emit out of the channel as experimentally shown in Fig. 2.6b.

To verify that this dependence is predicted by the model, we plot T_d versus I_{DS} in Fig. 2.8a. The values of I_{DS} are estimated from the transfer characteristics of an InP HEMT for $V_{DS} = 0.5$ V [93]. We observe a dependence of T_d on I_{DS} which compares reasonably with experiments (see Fig. 5 of Ref. [21], Figs. 4 and 5 of Ref. [105]). In addition to qualitatively reproducing the experimental drain temperature–drain current relationship, the theory offers a physical explanation for this dependence as arising from the dependence of the hot electron fraction on Fermi level, which is controlled by V_{GS}.

We next examine the dependence of T_d on physical temperature. Several authors have reported a temperature dependence of T_d, as in Fig. 8 of Ref. [106], Fig. 8 of Ref. [60], and Fig. 3 of Ref. [59]. On the other hand, other noise measurements were reported to be consistent with a temperature-independent T_d [61]. Importantly, one key observation from Fig. 2.5 is that the temperature dependence of the drain noise temperature is largely accounted for by the thermal noise temperature dependence, and another mechanism such as RST may be responsible for the residual weak temperature dependence and overall magnitude. This idea is supported by studies on electron energy in bulk semiconductors using Monte Carlo simulations that suggest that at high electric fields, electron energy possesses a weak dependence on physical temperature [107]. Because the physical temperature dependence of T_d in our model arises from the electron temperature as discussed above, a weak electron temperature dependence on the physical temperature would result in a drain temperature that is also weakly dependent on physical temperature.

However, if RST does possess a physical temperature, we briefly discuss below how this dependence, shown in Figure 2.8b, may arise. For a non-degenerate electron gas, the electronic heat capacity is constant [108] so that $T_e = T + \Delta T$ where ΔT denotes the electron temperature increase and is independent of T. In this figure, ΔT was chosen as 1000 K so that the computed T_d is consistent with reported cryogenic values in modern HEMTs (see Fig. 10 of Ref. [2]). The figure shows that T_d can vary with physical temperature because T_e varies linearly with physical temperature, which in turn affects T_d through η. We observe that this dependence is more pronounced at higher physical temperatures, the parameter range studied in Ref. [60]. At lower temperatures below 100 K, the dependence is weaker and may be more difficult to discern experimentally relative to room temperature measurements considering the challenge of accurately extracting the drain temperature from microwave noise data. The weaker dependence below 100 K may also account for the conclusions of Ref. [61] that T_d is independent of temperature because that study did not consider temperatures above 100 K. A quantitative comparison of the calculated dependence to experiment is difficult because T_d data are often reported with I_{DS} held constant, requiring shifts in V_{GS} to compensate for changes in mobility, conduction band offset, threshold voltage, and related quantities with temperature. Due to the lack of availability of certain data, particularly the variation of conduction band offset with temperature, such changes are not included in the present calculation and will be addressed in future work.

2.8 Discussion

We have presented evidence that drain noise in HEMTs can be attributed to the partition noise arising from RST of electrons from the channel to the barrier. We now discuss this finding in the context of prior explanations of drain noise. The first explanation for drain noise in the saturated region was due to Pucel *et al.* [109], who described the noise current in terms of the generation of dipole layers formed by random electron scattering events. However, their theory did not make testable predictions and so obtaining evidence to support it is difficult. Other authors have attributed noise in GaAs FETs [110, 111] and Si MOSFETs [112] to intervalley scattering. However, in modern InP HEMTs the $\Gamma - L$ separation in the $\mathrm{In}_x\mathrm{Ga}_{1-x}\mathrm{As}$ channel (0.55 eV at 300 K and $x = 0.53$ [113]) exceeds the conduction band offset so that RST is expected to occur prior to intervalley transfer. Experimental evidence for this expectation has been reported in AlGaAs/GaAs heterostructures, where noise at intermediate fields, below the threshold for intervalley transfer, is attributed to RST [73].

Several works have suggested that drain noise can be attributed to a suppressed shot noise mechanism in which electrons travel quasiballistically from source to drain [57, 114]. However, various studies of electron transport in quantum wells indicate that the electron mean free path is sufficiently short that the transport is not quasi-ballistic as required for the suppressed shot noise mechanism. For instance, time-resolved differential transmission spectra indicate that photo-excited electrons thermalize within around 200 fs, implying that electron-electron scattering is several times faster than this timescale [63]. Taking the electron-electron scattering time as around 20 fs, the corresponding mean free path is around 40 nm, nearly two orders of magnitude smaller than the $\sim 1\ \mu$m source-drain spacing of modern HEMTs. Further, hot electrons lose energy to the lattice on the drain side of the gate by optical phonon emission with a mean free path of tens of nanometers [62], further disrupting quasiballistic transport across the channel. These considerations suggest that electrons undergo sufficient scattering events to prevent the suppressed shot noise mechanism from contributing to drain noise.

Finally, we consider the predictions of the theory regarding how drain noise may be suppressed. A large ΔE_c is desired in HEMTs to maximize the channel sheet density [91]. Our theory predicts that ΔE_c is also important to suppress RST and hence drain noise. Minimizing RST requires increasing $\Delta E_c/k_B T_e$

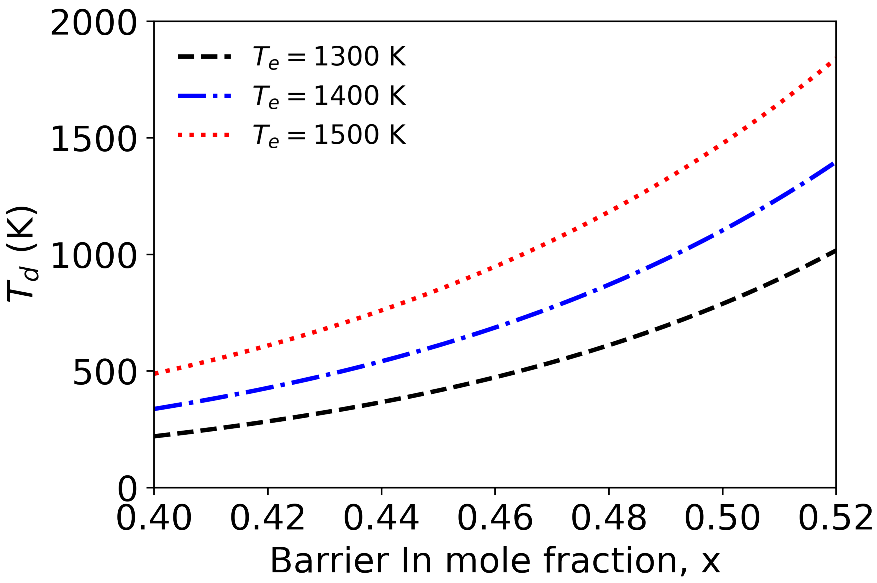

Figure 2.9: Drain temperature versus barrier mole fraction, x in $\mathrm{In}_x\mathrm{Al}_{1-x}\mathrm{As}$. A reduction in T_d is observed as x is decreased due to an increase in ΔE_c.

so that the hot electron fraction decreases. A lower T_e can be achieved by decreasing the InAs content of the channel and hence increasing the effective mass, but this change must be balanced against the need for high mobility and hence higher InAs content. An increase in conduction band offset, on the other hand, can be achieved without affecting the channel by reducing the InAs mole fraction of the barrier. Studies of HEMTs with barrier composition $(\mathrm{InAs})_x$, $0.3 < x < 0.5$, reported decreased RST in devices for smaller x [115]. However, x must be chosen accounting for the lattice mismatch between the channel and barrier that can lead to the formation of misfit dislocations that negatively impact the noise.

We quantify the impact of varied InAs mole fraction in the barrier on T_d by obtaining ΔE_c for each x [115], using these values to calculate the sheet density in the barrier, and following the same analysis as described in Sec. 2.7. The result is shown in Fig. 2.9. We observe a marked decrease in T_d as x is reduced from its lattice-matched value of 0.52 to 0.46, followed by a slower decrease from 0.46 to 0.4. Following Pospieszalski's noise model, specifically Eq. 26 in Ref. [6], a factor of ~ 2 reduction in T_d as seen when x changes from 0.52 to 0.46 translates to a factor of 1.4 reduction in the minimum noise temperature.

This analysis suggests that further improvements to the noise figure of HEMTs can be realized by optimizing the barrier InAs mole fraction.

2.9 Summary

We started this chapter by introducing HEMTs and motivating the need for pursing a deeper understanding of the physical mechanisms governing their noise performance. We surveyed important elements contributing to device performance, and identified a gap related to the contemporary understanding of drain noise in HEMTs. Drawing inspiration from decades of work on real-space transfer in quantum well heterostructures, we formulated a a theory of drain noise in high electron mobility transistors based on microwave partition noise arising from real-space transfer of electrons from the channel to the barrier. The theory successfully explains the reported magnitude and dependencies of T_d. The theory predicts that T_d can be decreased by altering the barrier composition to increase the conduction band offset and thus decrease the occurrence of RST. A reduction in the drain temperature of a HEMT leads to a corresponding decrease in the minimum noise temperature. These results may therefore guide the design of HEMTs with lower microwave noise figure.

Chapter 3

CHARGE TRANSPORT IN BORON ARSENIDE AND THE ROLE OF TWO-PHONON SCATTERING

This chapter has been adapted, in part, from:

> Iretomiwa Esho, and Austin J. Minnich. Charge transport in BAs and the role of two-phonon scattering. Physical Review B 108 (16), 165202

In addition to investigating hot electron transport phenomena in semiconductor devices, there's a need to explore materials that could serve as a basis for improved noise and overall performance. Thermally conductive materials with high charge mobility are desired because of their high frequency and heat dissipating characteristics. One such example is boron arsenide (BAs), a material with high thermal conductivity ~ 1300 W m^{-1} K^{-1} comparable to that of diamond [116, 117, 118, 119] and reported simultaneous high electron and hole mobilities, with computed room-temperature values of 1400 and 2110 cm^2 V^{-1} s^{-1}, respectively [120, 121]. These properties carry important implications for the semiconductor device landscape. For example, boron arsenide-integrated gallium nitride HEMTs exhibit state-of-the-art cooling performance, surpassing diamond-integrated HEMTs [122]. Simulations have also demonstrated its potential uses as a substrate material and as a conducting channel in transistors [121].

Reports of the thermal conductivity of BAs were initially significantly lower than the predictions due to what was thought to be scattering by As vacancies [123]. Theoretically, four-phonon processes were found to make a non-negligible contribution to phonon scattering, yielding a lower thermal conductivity compared to the original predictions [124]. After improvements in synthesis resulting in higher-quality samples, the high thermal conductivity was confirmed experimentally [117, 118, 119] and was found to be in quantitative agreement with predictions including four-phonon scattering.

Initial experiments that estimated the mobility from conductivity and thermoelectric measurements and a single parabolic band model yielded a lower hole mobility of 400 cm^2 V^{-1} s^{-1} [125]; recent direct Hall measurements yielded

$\sim$ 500 cm^2 V^{-1} s^{-1} on bulk samples [126]. The lower values obtained experimentally have been attributed to scattering by charged impurities in the defective samples which could be synthesized. Recent experiments have circumvented the need for high-quality macroscopic samples by measuring the ambipolar diffusivity of photoexcited carriers in a local region of the sample using transient grating experiments [126] or transient reflectivity microscopy [127]. Using the Einstein relation to convert the measured diffusivity into a mobility, these experiments obtained ambipolar mobilities of 1500–1600 cm^2 V^{-1} s^{-1} at some locations on the sample. These values are in good agreement with those calculated from first principles [120].

Most first-principles studies of the electron-phonon interactions employ the lowest level of perturbation theory involving one electron and one phonon (1ph) [128, 7], and this level of theory was also used for BAs [120, 121]. Given the contribution of higher-order phonon processes to thermal transport in BAs [124, 119, 118, 117], it is of interest to consider the role of higher-order processes in charge transport. Although evidence for the contribution of multiphonon processes to electron-phonon scattering has been previously reported [129, 130, 131], only recently have first-principles studies included the contribution of higher-order scattering processes, such as that of an electron with two phonons (2ph) in the electron-phonon interaction [132, 133, 134]. In GaAs at room temperature, the 2ph scattering rates were predicted to be on the order of the 1ph rates [132], resulting in a $\sim$ 40% reduction in the computed mobility at 300 K. Good quantitative agreement with experimental mobility was obtained only considering this correction. Corrections to the high-field transport properties of GaAs of a similar magnitude were also found [133]. For non-polar semiconductors, Hatanpää *et al.* reported improved agreement of the warm electron coefficient in Si over temperatures from 190 to 310 K with the inclusion of 2ph processes [134]. These studies suggest that inclusion of 2ph processes for electron-phonon scattering may be necessary to accurately predict the charge transport properties of semiconductors.

In this chapter, we report an *ab initio* study of the role of two-phonon scattering of electrons and holes on the charge transport properties of BAs. We find that the two-phonon rates may be as large as $\sim$ 50% of the one-phonon rates, leading to a marked reduction in the calculated ambipolar mobility from 1420 cm^2 V^{-1} s^{-1} to 810 cm^2 V^{-1} s^{-1} at room temperature and a 35–50% correction

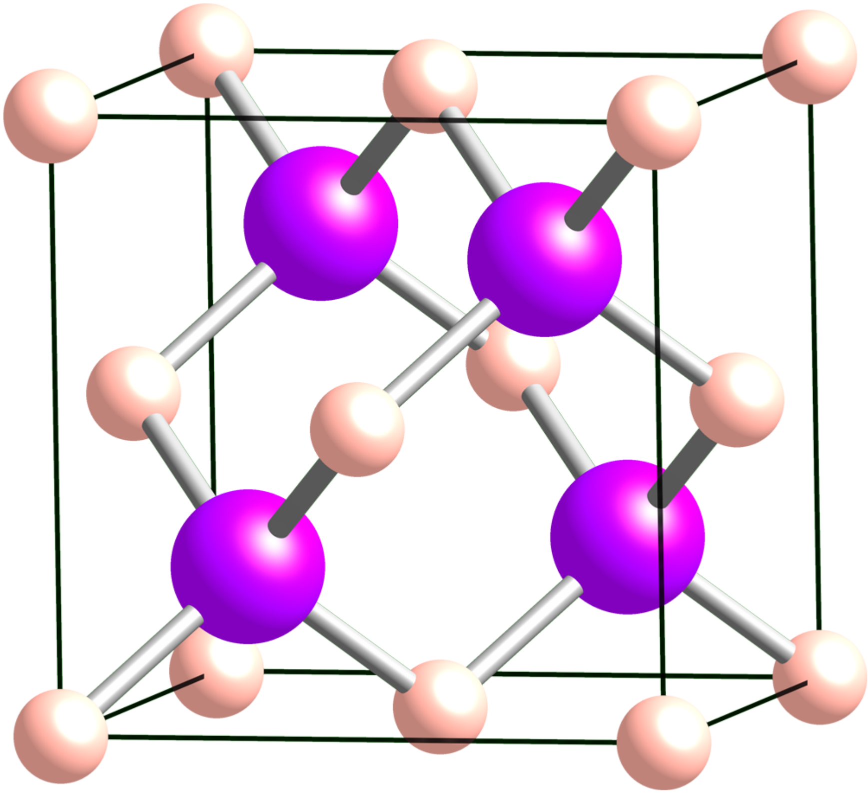

Figure 3.1: Model of the unit cell of boron arsenide showcasing its zinc blende structure.

to the carrier mobility over temperatures from 150 to 350 K. The experimental origin of the discrepancy could arise from the super-diffusion of hot carriers shortly after photoexcitation, an effect which has been observed using scanning ultrafast electron microscopy, leading to an overestimate of the ambipolar diffusivity. On the theory side, an underestimate of the predicted value is possible owing to cancellation between the iterated and direct contributions to 2ph scattering, the latter of which is neglected here. To test our predictions given the defective samples presently available, we suggest an experimental approach based on direct measurements of hot carrier lifetimes using the broadening of photoluminescence spectra.

3.1 Crystal structure of BAs

BAs is a cubic compound semiconductor composed of the III-V elements boron and arsenic. The unit cell is shown in Fig. 3.1 displaying its zinc blende structure. The experimentally measured lattice constant in BAs is ~ 0.4777

nm [135]. These atomic identities and positions, and an initial guess for the lattice constant make up all the material-specific information we need for a first-principles BTE analysis of its transport properties.

3.2 Solution of the BTE for charge transport

We will now build up the method for solving the BTE to study charge transport properties under the influence of an electric field. The BTE we are interested in solving is:

$$\frac{e\mathbf{E}}{\hbar} \cdot \nabla_{\mathbf{k}} f_{\mathbf{k}} = \mathcal{I}[f_{\mathbf{k}}] \tag{3.1}$$

where $f_{\mathbf{k}}$ is the electron occupation function at wave vector $\mathbf{k}$. Note that we have dropped the band index here for clarity. The electric field is $\mathbf{E}$ and the electronic charge is e. The collision integral is represented by $\mathcal{I}$ and describes electronic scattering from one state $\mathbf{k}$ to another state $\mathbf{k}'$. The collision integral is derived from Fermi's Golden Rule (FGR) and is a function of the electron occupation function because of the dependence of scattering on the initial and final states. We consider only time-independent processes in this work, such that $f_{\mathbf{k}}$ is the steady-state result. Further, we assume spatial homogeneity and a non-degenerate carrier concentration. Several observables of interest can be obtained after a solution of the BTE for $f_{\mathbf{k}}$. For example, the current density $J^{\alpha} = \sum_{\beta} \sigma^{\alpha\beta} E^{\beta}$, where $\sigma^{\alpha\beta}$ is the charge conductivity tensor, can be expressed as a sum over the Brillouin zone:

$$\mathbf{J} = \frac{2e}{V_0} \sum_{\mathbf{k}} \mathbf{v}_{\mathbf{k}} f_{\mathbf{k}} \tag{3.2}$$

where V_0 is the supercell volume, $\mathbf{v}_{\mathbf{k}}$ is the group velocity of the electronic state $\mathbf{k}$. The major complication in Eq. 3.1 comes from the collision integral $\mathcal{I}$ which we discuss next.

One-phonon collision integral

We focus on scattering from electron-phonon interactions, which are the dominant electron scattering processes near room temperature and at non-degenerate carrier concentrations. We first discuss the collision integral for electron-one-phonon (1ph) processes, where electrons scatter from one state $\mathbf{k}$ to another state $\mathbf{k}'$ through interaction with a phonon $\mathbf{q}$. The scattering integral from FGR is [136]:

$$\mathcal{I}[f_{\mathbf{k}}] = \frac{-2\pi}{\hbar N}\sum_{\mathbf{q}} |g_{\mathbf{k},\mathbf{q}}|^2 \bigg(\delta(\epsilon_{\mathbf{k}} - \hbar\omega_{\mathbf{q}} - \epsilon_{\mathbf{k}+\mathbf{q}}) H^{\text{em}} + \delta(\epsilon_{\mathbf{k}} + \hbar\omega_{\mathbf{q}} - \epsilon_{\mathbf{k}+\mathbf{q}}) H^{\text{abs}} \bigg) \tag{3.3}$$

where we have again suppressed the phonon branch indices for clarity. The sum is only over $\mathbf{q}$s that satisfy momentum conservation, and the delta functions ensure energy conservation. $g_{\mathbf{k},\mathbf{q}}$ is the electron-phonon matrix element, N is the number of sampled $\mathbf{q}$ points in the Brillouin zone, and H^{em} and H^{abs} are emission and absorption weights that contain the electron occupation functions because scattering should depend on the occupation of the respective states. The weights are in general non-linearly dependent on the occupations and are given by:

$$\begin{aligned} H^{\text{em}} &= f_{\mathbf{k}}(1 - f_{\mathbf{k}+\mathbf{q}})(N_{\mathbf{q}} + 1) - (1 - f_{\mathbf{k}}) f_{\mathbf{k}+\mathbf{q}} N_{\mathbf{q}} \\ H^{\text{abs}} &= f_{\mathbf{k}}(1 - f_{\mathbf{k}+\mathbf{q}})(N_{\mathbf{q}}) - (1 - f_{\mathbf{k}}) f_{\mathbf{k}+\mathbf{q}}(N_{\mathbf{q}} + 1) \end{aligned} \tag{3.4}$$

where $N_{\mathbf{q}}$ is the phonon occupation function. Our end goal is to write the BTE in matrix form so that it can be solved with numerical linear algebra, and therefore it needs to be linearized. We can make several valid approximations to get us to this goal.

First, we can expand the distribution functions about equilibrium, an assumption that relies on the electrons not being driven far out of equilibrium and is valid at low electric fields. We write the occupation function as $f_{\mathbf{k}} = f^0_{\mathbf{k}} + \Delta f_{\mathbf{k}}$. If we substitute this expansion into Eq. 3.4 and retain terms only linear in $\Delta f_{\mathbf{k}}$, and assume that phonons remain in equilibrium, we obtain after a bit of algebra:

$$\begin{aligned} H^{\text{em}} &= \Delta f_{\mathbf{k}}(N_{\mathbf{q}} + 1 - f^0_{\mathbf{k}+\mathbf{q}} - \Delta f_{\mathbf{k}+\mathbf{q}}) - \Delta f_{\mathbf{k}+\mathbf{q}}(f^0_{\mathbf{k}} + N_{\mathbf{q}}) \\ H^{\text{abs}} &= \Delta f_{\mathbf{k}}(N_{\mathbf{q}} + f^0_{\mathbf{k}+\mathbf{q}} + \Delta f_{\mathbf{k}+\mathbf{q}}) - \Delta f_{\mathbf{k}+\mathbf{q}}(N_{\mathbf{q}} + 1 - f^0_{\mathbf{k}}) \end{aligned} \tag{3.5}$$

Note that this set of equations is still non-linear because of the $\Delta f_{\mathbf{k}+\mathbf{q}}$ inside the parentheses. One justifiable assumption to get around this is to recall that we are in the low-field regime where the system responds linearly to the external field. Therefore, it is reasonable to assume that the electronic occupations $f_{\mathbf{k}}$ do not deviate far from equilibrium such that $\Delta f_{\mathbf{k}}$ in $f_{\mathbf{k}} = f^0_{\mathbf{k}} + \Delta f_{\mathbf{k}}$ is small compared to $f^0_{\mathbf{k}}$. This allows us to neglect terms of the form $\Delta f_{\mathbf{k}} \Delta f_{\mathbf{k}+\mathbf{q}}$ in Eq. 3.5, resulting in a linear collision integral with the weights:

$$\begin{aligned} H^{\text{em}} &= \Delta f_{\mathbf{k}}(N_{\mathbf{q}} + 1 - f^0_{\mathbf{k}+\mathbf{q}}) - \Delta f_{\mathbf{k}+\mathbf{q}}(f^0_{\mathbf{k}} + N_{\mathbf{q}}) \\ H^{\text{abs}} &= \Delta f_{\mathbf{k}}(N_{\mathbf{q}} + f^0_{\mathbf{k}+\mathbf{q}}) - \Delta f_{\mathbf{k}+\mathbf{q}}(N_{\mathbf{q}} + 1 - f^0_{\mathbf{k}}) \end{aligned} \tag{3.6}$$

Importantly, we could have reached a similar conclusion from the fact that our analysis is limited to non-degenerate carrier concentrations, for which $f_{\mathbf{k}} \ll N_{\mathbf{q}}$ even at high electric fields, allowing us to also safely assume $\Delta f_{\mathbf{k}} \ll N_{\mathbf{q}}$. Our weights then become:

$$\begin{aligned} H^{\text{em}} &= \Delta f_{\mathbf{k}}(N_{\mathbf{q}} + 1) - \Delta f_{\mathbf{k}+\mathbf{q}}(N_{\mathbf{q}}) \\ H^{\text{abs}} &= \Delta f_{\mathbf{k}}(N_{\mathbf{q}}) - \Delta f_{\mathbf{k}+\mathbf{q}}(N_{\mathbf{q}} + 1) \end{aligned} \tag{3.7}$$

With this linearization, we can write the collision integral $\mathcal{I}[f_{\mathbf{k}}]$ in terms of a scattering matrix $\Theta_{\mathbf{k},\mathbf{k}'}$:

$$\begin{aligned} \mathcal{I}[f_{\mathbf{k}}] = \sum_{\mathbf{k}'} \Theta_{\mathbf{k},\mathbf{k}'} \Delta f_{\mathbf{k}'} = \frac{-2\pi}{\hbar N} \sum_{\mathbf{q}} |g_{\mathbf{k},\mathbf{q}}|^2 \Big[&\big(\delta^{\text{abs}}_{\mathbf{k},\mathbf{q}} N_{\mathbf{q}} + \delta^{\text{em}}_{\mathbf{k},\mathbf{q}}(N_{\mathbf{q}} + 1)\big) \Delta f_{\mathbf{k}} \\ &+ \big(\delta^{\text{abs}}_{\mathbf{k},\mathbf{q}}(N_{\mathbf{q}} + 1) + \delta^{\text{em}}_{\mathbf{k},\mathbf{q}} N_{\mathbf{q}}\big) \Delta f_{\mathbf{k}+\mathbf{q}} \Big] \end{aligned} \tag{3.8}$$

Here, the $\delta_{\mathbf{k},\mathbf{q}}$ terms correspond to those given in Eq. 3.3. The diagonal terms of the matrix are the scattering rates times -1 while the off-diagonal terms are the in-scattering rates, which are only non-zero when $\mathbf{k}' = \mathbf{k} + \mathbf{q}$.

Electric field term in BTE

Now that we have successfully treated the right hand side of Eq. 3.1, we need to consider its left hand side which contains the electric field term and reciprocal space gradients of the occupation functions. The derivative of the equilibrium occupation with respect to $\mathbf{k}$ is an analytical function:

$$\nabla_{\mathbf{k}} f^0_{\mathbf{k}} = \frac{df^0_{\mathbf{k}}}{d\epsilon_{\mathbf{k}}} \frac{d\epsilon_{\mathbf{k}}}{d\mathbf{k}} = -\frac{\hbar}{k_B T} \mathbf{v}_{\mathbf{k}} f^0_{\mathbf{k}} (1 - f^0_{\mathbf{k}}) \tag{3.9}$$

However, we still need the reciprocal space gradient of the deviational occupation, $\nabla_{\mathbf{k}}[\Delta f_{\mathbf{k}}]$. This derivative can be obtained with a finite difference method as shown in Ref. [14]:

$$\nabla_{\mathbf{k}}[\Delta f_{\mathbf{k}}] = \sum_{\mathbf{b}} w_b \mathbf{b}(\Delta f_{\mathbf{k}+\mathbf{b}} - \Delta f_{\mathbf{k}}) \tag{3.10}$$

where $\mathbf{b}$ is a set of vectors that connects a point in the uniformly discretized Brillouin zone to its neighbors and $b = |\mathbf{b}|$ is a constant weight for each set of vectors. Equation 3.10 is required to be correct to linear order from the following condition:

$$\sum_{s}^{N} w_s \sum_{i}^{M_s} b_\alpha^{i,s} b_\beta^{i,s} = \delta_{\alpha\beta} \tag{3.11}$$

where α, β are the Cartesian directions, N is the total number of required nearest neighbor "shells," w_s is the weight associated with the sth shell, and M_s is the total number of nearest neighbor vectors in the sth shell. The weights can be determined by expressing Eq. 3.11 as a matrix equation and inverting the resulting equation to obtain the weights. The procedure for choosing the shells starts with adding shells in order of increasing $|\mathbf{b}|$ and checking if Eq. 3.11 is satisfied. If so, we stop. Otherwise we add the next shell of nearest neighbors and keep checking till Eq. 3.11 is satisfied. For a cubic Bravais lattice point group, the first shell satisfies the required condition. For a one dimensional function with two nearest neighbors, Eq. 3.10 simply reduces to the central difference formula as illustrated in Ref. [137]. We can write the finite difference formula in matrix form, including the electric field term as [137]:

$$\sum_{\alpha} \sum_{\mathbf{k}'} \frac{eE_\alpha}{\hbar} D^{\alpha}_{\mathbf{k},\mathbf{k}'} \Delta f_{\mathbf{k}'} = \sum_{\alpha} \sum_{\mathbf{b}} E_\alpha b_\alpha w_b (\Delta f_{\mathbf{k}+\mathbf{b}} - \Delta f_{\mathbf{k}}) \tag{3.12}$$

where $D^{\alpha}_{\mathbf{k},\mathbf{k}'}$ is only non-zero when $\mathbf{k}' = \mathbf{k} + \mathbf{b}$ or $\mathbf{k}' = \mathbf{k}$. The setup is now complete. The current form of the BTE is:

$$-\frac{e\mathbf{E}}{k_B T} \cdot \mathbf{v}_{\mathbf{k}} f^0_{\mathbf{k}} (1 - f^0_{\mathbf{k}}) + \sum_{\alpha} \sum_{\mathbf{k}'} \frac{eE_\alpha}{\hbar} D^{\alpha}_{\mathbf{k},\mathbf{k}'} \Delta f_{\mathbf{k}'} = \mathcal{I}[f_{\mathbf{k}}] = \sum_{\mathbf{k}'} \Theta_{\mathbf{k},\mathbf{k}'} \Delta f_{\mathbf{k}'} \tag{3.13}$$

By rearranging terms, we obtain the final form of the BTE:

$$\sum_{\mathbf{k}'} \left[\sum_{\alpha} \frac{eE_\alpha}{\hbar} D^{\alpha}_{\mathbf{k},\mathbf{k}'} - \Theta_{\mathbf{k},\mathbf{k}'} \right] \Delta f_{\mathbf{k}'} = \sum_{\mathbf{k}'} \Lambda_{\mathbf{k},\mathbf{k}'} \Delta f_{\mathbf{k}'} = \frac{e\mathbf{E}}{k_B T} \cdot \mathbf{v}_{\mathbf{k}} f^0_{\mathbf{k}} (1 - f^0_{\mathbf{k}}) \tag{3.14}$$

where we have defined a relaxation operator $\Lambda_{\mathbf{k},\mathbf{k}'}$ that combines the finite difference and scattering matrices. The solution to the BTE is:

$$\Delta f_{\mathbf{k}} = \sum_{\mathbf{k}'} \Lambda^{-1}_{\mathbf{k},\mathbf{k}'} \left(\frac{e\mathbf{E}}{k_B T} \cdot \mathbf{v}_{\mathbf{k}'} f^0_{\mathbf{k}'} (1 - f^0_{\mathbf{k}'}) \right) \tag{3.15}$$

. We have now completed the formulation to obtain the non-equilibrium steady state electronic distribution, from which we can obtain several observables of interest, using matrix algebra. So far, we have only considered one-phonon processes where electrons scatter from one state $\mathbf{k}$ to another state $\mathbf{k}'$ through interaction with one phonon. Later, we will follow a similar procedure to include higher order processes where an electron interacts with two phonons.

Iterative scheme to solve the BTE

Now, we will discuss an alternative solution scheme for the BTE which will come in handy in Chapter IV. We seek an alternative linearization where the occupation has the form:

$$f_{\mathbf{k}} = f^0_{\mathbf{k}} + f^0_{\mathbf{k}}(1 - f^0_{\mathbf{k}}) \frac{e\mathbf{E}}{k_B T} \cdot \mathbf{F}_{\mathbf{k}} \tag{3.16}$$

where $\mathbf{F}_{\mathbf{k}}$ is a new dummy variable. Then, we can write Δf as:

$$\Delta f_{\mathbf{k}} = f^0_{\mathbf{k}}(1 - f^0_{\mathbf{k}}) \frac{e\mathbf{E}}{k_B T} \cdot \mathbf{F}_{\mathbf{k}} \tag{3.17}$$

Following what we have done so far, the BTE of Eq. 3.1 can be written as:

$$\begin{aligned} \mathbf{v}_{\mathbf{k}} = \frac{2\pi}{\hbar N} \sum_{\mathbf{q}} |g_{\mathbf{k},\mathbf{q}}|^2 \Big[& \big(\delta^{\text{abs}}_{\mathbf{k},\mathbf{q}} (N_{\mathbf{q}} + f^0_{\mathbf{k}+\mathbf{q}}) + \delta^{\text{em}}_{\mathbf{k},\mathbf{q}} (N_{\mathbf{q}} + 1 - f^0_{\mathbf{k}+\mathbf{q}}) \big) F_{\mathbf{k}} \\ & - \frac{f^0_{\mathbf{k}+\mathbf{q}}(1 - f^0_{\mathbf{k}+\mathbf{q}})}{f^0_{\mathbf{k}}(1 - f^0_{\mathbf{k}})} \big(\delta^{\text{abs}}_{\mathbf{k},\mathbf{q}} (N_{\mathbf{q}} + 1 - f^0_{\mathbf{k}}) + \delta^{\text{em}}_{\mathbf{k},\mathbf{q}} (N_{\mathbf{q}} + f^0_{\mathbf{k}}) \big) F_{\mathbf{k}+\mathbf{q}} \Big] \end{aligned} \tag{3.18}$$

where $\frac{e\mathbf{E}}{k_B T} f^0_{\mathbf{k}}(1 - f^0_{\mathbf{k}})$ has been divided out. One approximation to this equation is to ignore the second part of the right side of Eq. 3.18 and solve for $\mathbf{F}_{\mathbf{k}} = \mathbf{F}^{\text{RTA}}_{\mathbf{k}}$; the key assumption being that the occupations of a state $\mathbf{k}$ are independent of the occupation of all the other states. This means that the other states are assumed in equilibrium and there will be no scattering from $\mathbf{k}'$ to the state $\mathbf{k}$ in consideration. This is known as the relaxation time approximation (RTA), where the relaxation time $\tau_{\mathbf{k}}$ is defined as:

$$\tau_{\mathbf{k}}^{-1} = \frac{2\pi}{\hbar N} \sum_{\mathbf{q}} |g_{\mathbf{k},\mathbf{q}}|^2 \Big[\delta_{\mathbf{k},\mathbf{q}}^{\text{abs}} (N_{\mathbf{q}} + f_{\mathbf{k}+\mathbf{q}}^0) + \delta_{\mathbf{k},\mathbf{q}}^{\text{em}} (N_{\mathbf{q}} + 1 - f_{\mathbf{k}+\mathbf{q}}^0) \Big] \tag{3.19}$$

Here, we see the interpretation of $\mathbf{F}_{\mathbf{k}} = \mathbf{v}_{\mathbf{k}} \tau_{\mathbf{k}}$ as the mean free path of electron. This is usually a reasonable approximation but a full approximation is required for most semiconductors.

The iterative solution to the BTE is based on Eq. 3.18. We start by iterating from the RTA solution, setting all the $\mathbf{F}_{\mathbf{k}+\mathbf{q}}$ to $\mathbf{F}_{\mathbf{k}}^{\text{RTA}}$, evaluating the resulting sum to obtain the next solution $\mathbf{F}_{\mathbf{k}}^{\text{i}+1}$ and keep iterating until convergence.

Two-phonon collision integral

We now discuss two-phonon scattering of the form where an electron is scattered by two consecutive one-phonon events. We emphasize the distinction between this type of two-phonon scattering and instantaneous two-phonons scattering which results from the second derivative of the perturbation potential, the latter which we do not consider in this work. A schematic of the 2ph process is shown in

The 2ph scattering rate as derived in Ref. [132] is:

$$\Gamma_{\mathbf{k}}^{\text{2ph}} = \frac{2\pi}{\hbar N^2} \sum_{\mathbf{q}} \sum_{\mathbf{p}} \left[\Gamma^{\text{1e1a}} + \Gamma^{\text{2e}} + \Gamma^{\text{2a}} \right] \tag{3.20}$$

where we sum over all pairs of phonons that couple **k** to **k**'. The first phonon is indexed by q, the second phonon is indexed by p and N is the number of sampled phonon points. Γ^{1e1a}, Γ^{2a}, and Γ^{2e} refer to emission-absorption, absorption-absorption, and emission-emission electron-phonon processes. The contribution from each of these sub-types (i) is:

$$\Gamma^i = A^i W^i \delta(\epsilon_{\mathbf{k}} - \epsilon_{\mathbf{k}'} - \alpha_{\mathbf{p}}^i \omega_{\mathbf{p}} - \alpha_{\mathbf{q}}^i \omega_{\mathbf{q}}) \tag{3.21}$$

where $\mathbf{k}' = \mathbf{k} + \mathbf{q} + \mathbf{p}$, A^i is a weighting factor, W^i is the 2ph sub-process amplitude, and $\alpha^i = \pm 1$:

$$\begin{gathered} \alpha_{\mathbf{p}}^{1e1a} = 1,\ \alpha_{\mathbf{p}}^{2e} = 1,\ \alpha_{\mathbf{p}}^{2a} = -1, \\ \alpha_{\mathbf{q}}^{1e1a} = -1,\ \alpha_{\mathbf{q}}^{2e} = 1,\ \alpha_{\mathbf{q}}^{2a} = -1 \end{gathered} \tag{3.22}$$

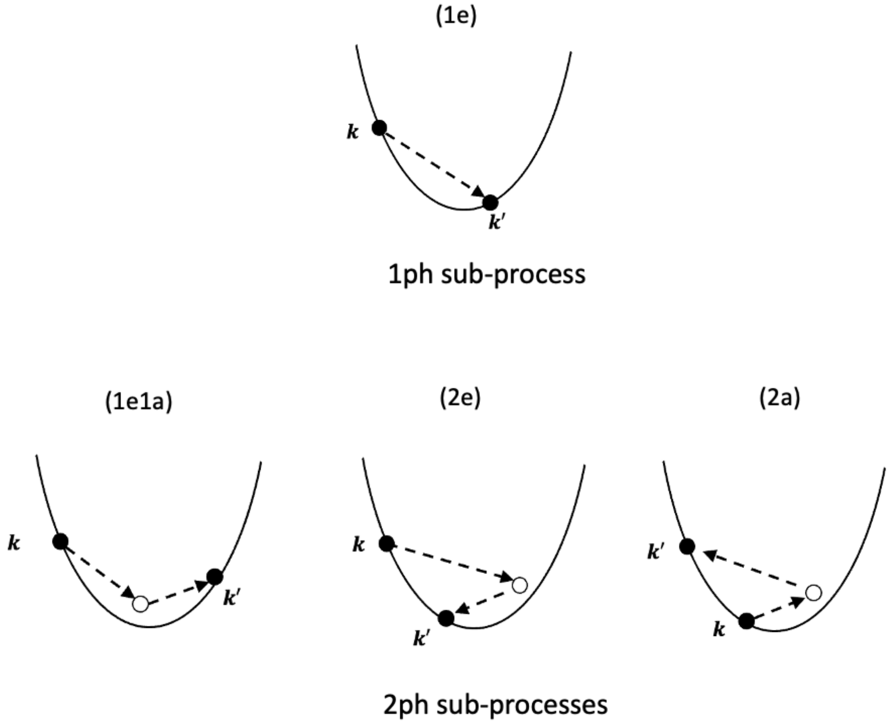

Figure 3.2: Schematic of 1ph and 2ph processes. The top panel is a pictorial representation of the electron-phonon process considered in most first-principles studies of transport in semiconductors, and is the lowest order of perturbation theory. Here, electrons scatter from a state k to another state k' by emission or absorption of a phonon (phonon absorption is not shown in the top panel). The bottom panel represents electron-phonon processes of next-to-leading order (2ph), where an electron may undergo consecutive 1ph scattering with phonons. These processes can be emission-absorption (1e1a), emission-emission (2e), or absorption-absorption (2a).

The sub-process amplitude is given by the following expression:

$$W^i = \left| \left(\frac{g_\nu(\mathbf{k},\mathbf{q}) g_\mu(\mathbf{k}+\mathbf{q},\mathbf{p})}{\epsilon_{\mathbf{k}'} - \epsilon_{\mathbf{k}+\mathbf{q}} + \alpha^i_{\mathbf{p}} \omega_{\nu\mathbf{p}} + i\eta - \Sigma_{\mathbf{k}+\mathbf{q}}} + \frac{g_\mu(\mathbf{k},\mathbf{p}) g_\nu(\mathbf{k}+\mathbf{p},\mathbf{q})}{\epsilon_{\mathbf{k}'} - \epsilon_{\mathbf{k}+\mathbf{q}} + \alpha^i_{\mathbf{q}} \omega_{\nu\mathbf{q}} + i\eta - \Sigma_{\mathbf{k}+\mathbf{p}}} \right) \right|^2 \tag{3.23}$$

Here, we have included the phonon mode indices μ and ν. $g_\nu(\mathbf{k},\mathbf{q}$ is the matrix element coupling a state $\mathbf{k}$ to another state $\mathbf{k}+\mathbf{q}$ through interaction with a phonon $\mathbf{q}$ with mode ν. The band energy at $\mathbf{k}$ is represented by $\epsilon_{\mathbf{k}}$, ω are phonon energies, $i\eta$ is a small term that prevents divergences when the other terms in the denominator sum to zero, and $\Sigma_{\mathbf{k}+\mathbf{q}}$ is the self-energy of the state at $\mathbf{k}+\mathbf{q}$.

We now discuss several details of the 2ph process we consider this work. Firstly, the intermediate state reached after interaction with the first phonon does not have to correspond to a band energy. In the case that this intermediate state coincides with a band energy, this process is termed on-shell, otherwise it's an off-shell process. The off-shell extent is the difference between the off-shell energy and the corresponding band energy. The off-shell extent must be chosen carefully, otherwise our task would be computationally intractable since the intermediate state energy can take any value (see Fig. 3.2). Since the 2ph rate is inversely proportional to the off-shell extent, we expect a "nearly on-shell" approximation to capture most relevant 2ph processes. Secondly, the 2ph process amplitude depends on Σ, the self-energy of the intermediate state for which we only include its imaginary part since the real part acts to correct the band structure and has minimal effect on the scattering rate [132]. The calculation for the 2ph scattering rate is then solved in a self-consistent manner since Σ includes both 1ph and 2ph scattering, $|\mathrm{Im}\Sigma| = \hbar/2[\Gamma^{\mathrm{1ph}} + \Gamma^{\mathrm{2ph}}]$, and we iterate until the 2ph rate from Eq. 3.20 equals the 2ph contribution to $|\mathrm{Im}\Sigma|$. Next, the weighting factors A^i in Eq. 3.21 are given by the following expressions:

$$\begin{aligned}
A^{\mathrm{1e1a}} &= N_{\nu\mathbf{q}} + N_{\nu\mathbf{q}}N_{\mu\mathbf{p}} + N_{\nu\mathbf{q}}f_{\mathbf{k}'} \\
A^{\mathrm{2e}} &= \frac{(1+N_{\nu\mathbf{q}})(1+N_{\mu\mathbf{p}} - f'_{\mathbf{k}}) - N_{\mu\mathbf{p}}f_{\mathbf{k}'}}{2} \\
A^{\mathrm{2a}} &= \frac{N_{\nu\mathbf{q}}(N_{\mu\mathbf{p}} + f_{\mathbf{k}'}) + (1+N_{\mu\mathbf{p}})f_{\mathbf{k}'}}{2}
\end{aligned} \tag{3.24}$$

We can simplify these expressions by again considering a non-degenerate carrier concentration whereby $f'_{\mathbf{k}} \ll 1$ to obtain:

$$\begin{aligned}
A^{\mathrm{1e1a}} &= N_{\nu\mathbf{q}} + N_{\nu\mathbf{q}}N_{\mu\mathbf{p}} \\
A^{\mathrm{2e}} &= \frac{(1+N_{\nu\mathbf{q}})(1+N_{\mu\mathbf{p}})}{2} \\
A^{\mathrm{2a}} &= \frac{N_{\nu\mathbf{q}}N_{\mu\mathbf{p}}}{2}
\end{aligned} \tag{3.25}$$

Although we do not show the effect of high fields on our observables in this work, these approximations ensure that our formalism can be easily generalized to obtain high-field properties.

3.3 Dipole and quadrupole electron-phonon interactions

As discussed in the introduction, the approach to *ab initio* calculations is to first carry out DFPT calculations on coarse $\mathbf{k}$ and $\mathbf{q}$ grids, and then interpolate the calculated quantities onto fine grids using Wannier functions. However, the interpolation near $\mathbf{q} = 0$, is challenging because the perturbation potential can be non-analytic in this region. A long-range multipole expansion of the perturbation potential yields dipole, quadrupole, octopole, and other higher order terms. It has been shown that the long-range dipole (also known as Fröhlich) term diverges as $1/q$ in polar materials, while the quadrupole term approaches a constant value [138, 139]. In nonpolar materials, the Fröhlich) term vanishes as $\mathbf{q} \to 0$, and the quadrupole term becomes dominant [140]. The long-range multipole expansion of the cell-integrated charge response to atomic displacement is [140, 141]:

$$C^{\mathbf{q}}_{k,\alpha} = -iq_\beta Z_{\kappa,\alpha\beta} - \frac{q_\beta q_\gamma}{2} Q_{\kappa,\alpha\beta\gamma} + ... \tag{3.26}$$

where κ is the atom index, β and γ represent Cartesian indices, and the dots are octopole and other higher order terms that are not considered in this work. Here, $\mathbf{Z}_\kappa$ is the first-order rank-2 tensor that corresponds to the Born effective charge (dipole term), and $\mathbf{Q}_\kappa$ is the rank-3 quadrupole tensor. Each of these terms generates macroscopic electric fields in semiconductors. Intuitively, the dipole effect can be understood as the cell response to a formed dipole moment, while the quadrupole effect results from a configuration of two oppositely oriented but equal dipoles. A schematic of the dipole and quadrupole configurations is shown in Fig. 3.3.

Starting from Eq. 3.26, the dipole and quadrupole matrix elements can be obtained from the dipole and quadrupole potentials, respectively, as [140]:

$$\begin{aligned} g^{\text{dip}}_{mn\nu}(\mathbf{k},\mathbf{q}) = \frac{ie^2}{\Omega\varepsilon_0} \sum_\kappa \left(\frac{\hbar}{2\omega_{\nu\mathbf{q}} M_\kappa}\right)^{1/2} \sum_{\mathbf{G}\neq-\mathbf{q}} \frac{(\mathbf{Z}_\kappa \mathbf{e}^\kappa_{\nu\mathbf{q}}) \cdot (\mathbf{q}+\mathbf{G})}{(\mathbf{q}+\mathbf{G}) \cdot \boldsymbol{\epsilon} \cdot (\mathbf{q}+\mathbf{G})} \\ \times \langle m\mathbf{k}+\mathbf{q}| \, e^{i(\mathbf{q}+\mathbf{G})\cdot(\mathbf{r}-\boldsymbol{\tau})} \, |n\mathbf{k}\rangle \end{aligned} \tag{3.27}$$

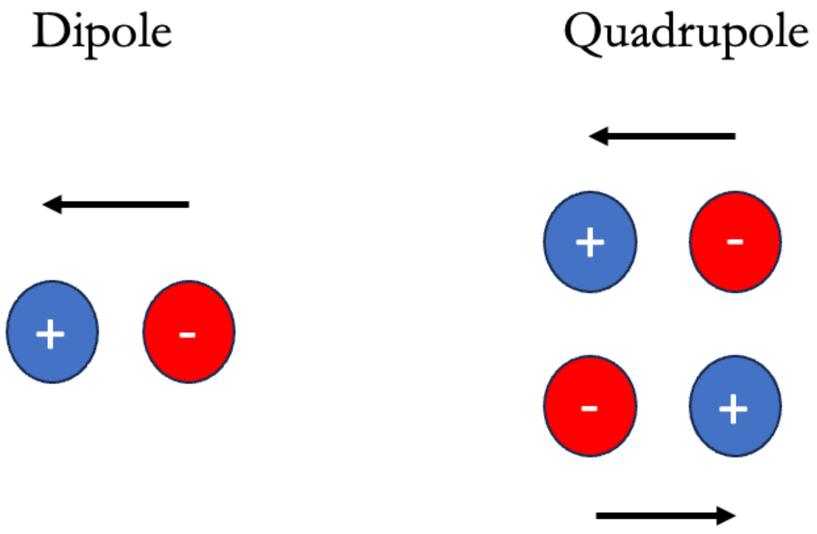

Figure 3.3: Schematic of dipole and quadrupole configurations showing quadrupole moment resulting from arrangement of equal and oppositely oriented-dipoles. The electron-phonon interaction arising from quadrupoles is important in both and polar and nonpolar semiconductors.

$$g_{mn\nu}^{\text{quad}}(\mathbf{k},\mathbf{q}) = \frac{ie^2}{\Omega\varepsilon_0}\sum_{\kappa}\left(\frac{\hbar}{2\omega_{\nu\mathbf{q}}M_\kappa}\right)^{1/2}\sum_{\mathbf{G}\neq-\mathbf{q}}\frac{1}{2}\frac{(\mathbf{q}+\mathbf{G})_\alpha(Q_{\kappa,\alpha\beta\gamma}\mathbf{e}^{\kappa}_{\nu\mathbf{q},\gamma})(\mathbf{q}+\mathbf{G})_\beta}{(\mathbf{q}+\mathbf{G})_\alpha\epsilon_{\alpha\beta}(\mathbf{q}+\mathbf{G})_\beta} \times \langle m\mathbf{k}+\mathbf{q}|\, e^{i(\mathbf{q}+\mathbf{G})\cdot(\mathbf{r}-\tau_\kappa)}\, |n\mathbf{k}\rangle \tag{3.28}$$

where $\boldsymbol{\epsilon}$ is the material dielectric tensor, G are reciprocal lattice vectors, ν is a phonon mode index, and Ω is the unit cell volume. $\mathbf{e}^{\kappa}_{\nu\mathbf{q}}$ is the eigenvector of the dynamical matrix at $\mathbf{q}$ and M_κ is the mass of atom κ positioned at τ. We observe in the limit of long wavelength ($\mathbf{q} \to 0$) that Eqs. 3.27 and 3.28 approach $1/q$ and a constant value, respectively. Similarly, quadrupolar corrections to the dynamical matrices for small $\mathbf{q}$ can be obtained [142, 143]. Note that quadrupole corrections are typically not considered in most *ab initio* works, but we separately consider their effect on the 1ph electron mobility in BAs in section 3.5.

3.4 Computational details

We computed the mobility of electrons and holes in BAs using established methods based on density functional theory (DFT) and density functional perturbation theory (DFPT) [144, 145, 146, 7]. Briefly, we obtained the electronic structure and electron-phonon matrix elements using QUANTUM ESPRESSO [147] with a relaxed lattice constant of 4.819 Å, a coarse $12 \times 12 \times 12$ **k** grid, and plane wave cutoff of 80 Ry. A fully relativistic ultrasoft potential with the Perdew–Burke–Ernzerhof (PBE) exchange-correlation functional was used. For the DFPT calculations, we employed a $6 \times 6 \times 6$ phonon **q** grid. The band structure and electron-phonon matrix elements were interpolated onto fine 160^3 and 80^3 **k** and **q** grids, respectively, using PERTURBO [148]. Increasing the grid density to 200^3 and 100^3 for the **k** and **q** grids, respectively, changed the mobility by 2%. The Fermi level was chosen so as to obtain a carrier concentration of 10^{15} cm^{-3} at all temperatures. The energy window was set to 200 meV above (below) the band extremum for electrons (holes). Increasing the energy window to 250 meV changed the mobility by 0.6%. We explicitly constructed the collision matrix and solved the Boltzmann transport equation using numerical linear algebra, from which transport properties were calculated. Details of this approach are given elsewhere [144, 133, 134]. The contributions of the next-to-leading order electron-phonon scattering (2ph) processes originally derived in Ref. [132] were computed following the implementation used in Ref. [133]. The 2ph rates were iterated five times. Increasing the number of iterations to 6 changed the mobility by 2.7%.

For the investigation of the effect of quadrupolar corrections, we compute the dynamical quadrupoles following the implementation in the ABINIT software [149] which is currently limited to pseudopotentials with non-linear core corrections and LDA functionals, and compute the electron mobility with the EPW software [150].

3.5 Results

Band structure and phonon dispersion

The Wannier-interpolated band structure of BAs is shown in Fig. 3.4. The conduction band minimum (CBM) occurs between the Γ and X points in the Brillouin zone, and the valence band maximum (VBM) occurs at Γ. The VBM is doubly degenerate at Γ instead of triply degenerate because of band splitting from the inclusion of spin orbit coupling (SOC) in our calculations. In

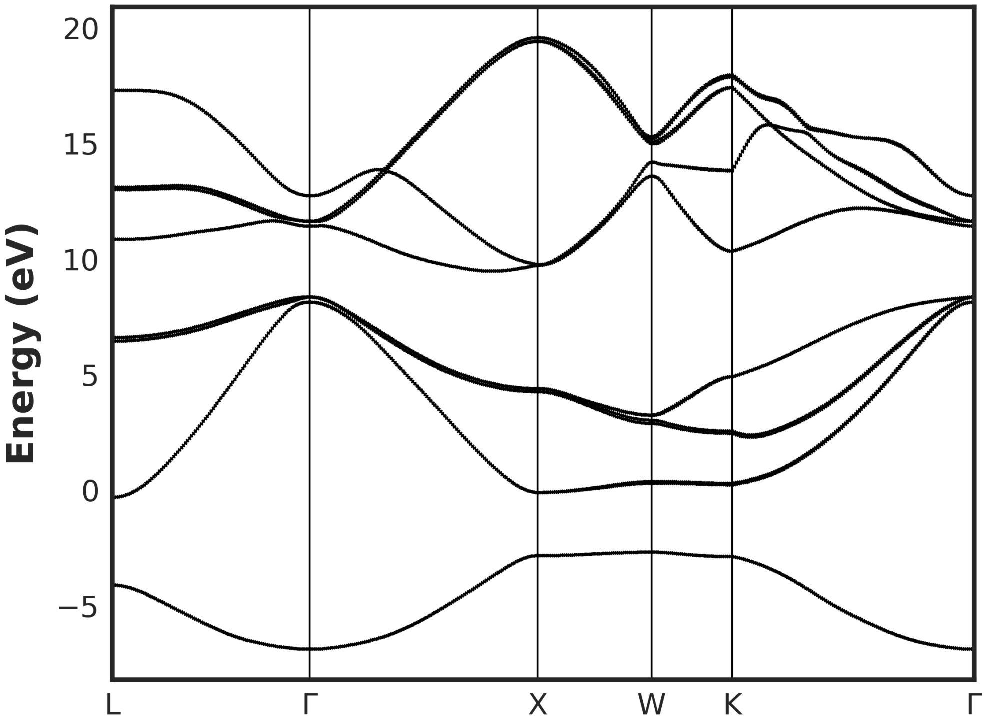

Figure 3.4: Electronic band structure of BAs showing four valence bands and the four lowest lying conduction bands. The valence band maximum occurs at the Γ point in the Brillouin zone, and the conduction band minimum is along the $\Gamma - X$ direction, making BAs an indirect gap semiconductor.

the standard time-independent Kohn-Sham description, relativistic effects are disregarded and therefore SOC is neglected. For electron transport in semiconductors, this is typically a good approximation as SOC has little effect near the the conduction band minimum [151, 121]. However, this is not the case for the valence band. SOC can be captured by employing the appropriate fully relativistic pseudopotentials and a noncollinear representation of the electronic spin degrees of freedom. Because SOC breaks degeneracy at the VBM, seen more clearly in Fig. 3.5, the number of scattering channels is reduced which consequently affects the computed value of the hole mobility.

We next discuss properties of the computed phonon dispersion of BAs, shown in Fig. 3.6. We note two distinct features. First, the optical phonon energy is ∼ 80 meV, which is ≈ 930 K in temperature units. Second, there is a large gap between the acoustic and optical branches. The high Debye temperature, in combination with the acoustic-optical gap, is responsible for the

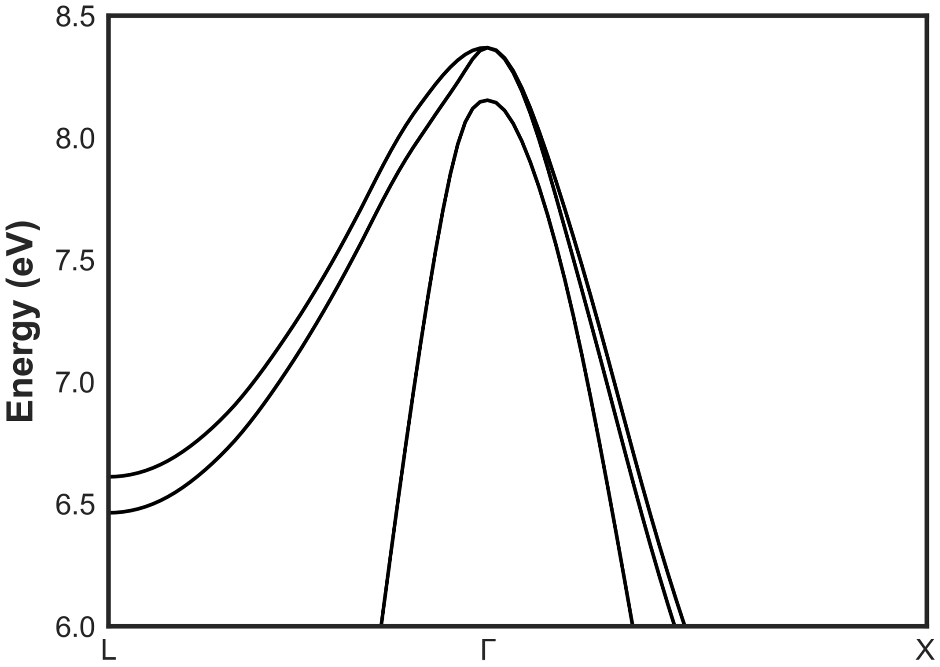

Figure 3.5: Zoomed in band structure of BAs showing degeneracy breaking due to spin orbit coupling. Inclusion of spin orbit coupling in our calculations is important to accurately capture transport properties of holes due to the reduction in the number of scattering channels near the valence band maximum.

observed high thermal conductivity in BAs because it restricts the phase space for three-phonon (phonon-phonon) scattering. Further, the high Debye temperature limits interaction between electrons and longitudinal optical (LO) phonons at room temperature and low electric field because the thermal energy of the electron population at 300 K is not sufficient for significant LO phonon emission of electrons. This has consequences for the electron and hole mobility since LO phonon emission tends to limit the carrier mobility in polar semiconductors [7].

1ph and 2ph scattering rates

The calculated scattering rates for electrons and holes are shown in Figures 3.7a and 3.7b. The trend of the 1ph scattering rates agrees with that reported previously [120]; quantitative differences are due to differing exchange-correlation functional or pseudopotential necessitated by the use of Perturbo

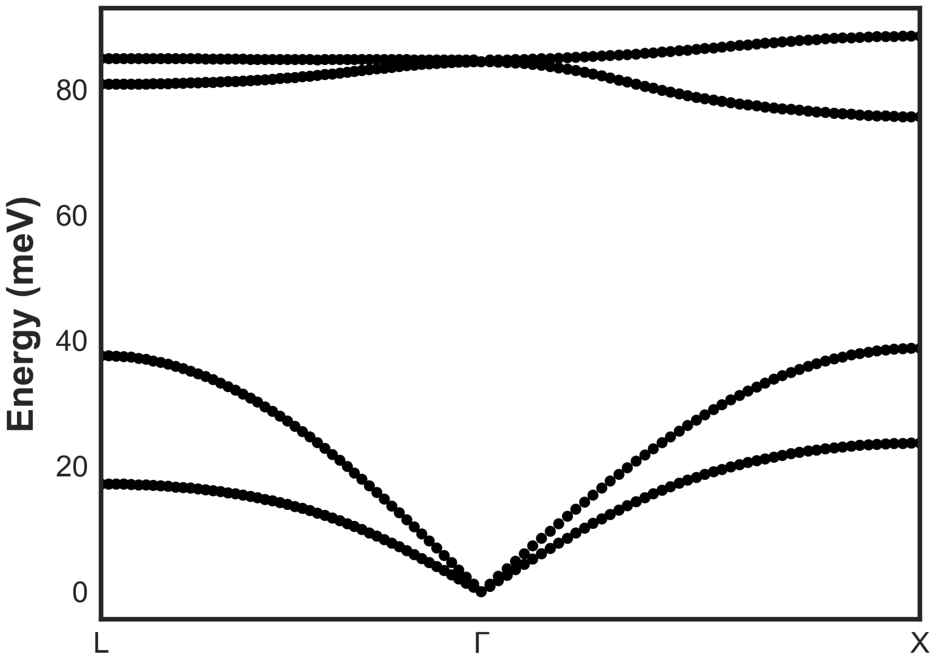

Figure 3.6: Phonon dispersion of BAs. The high Debye temperature is responsible for its exceptional thermal conductivity as it restricts the phase space for three-phonon phonon-phonon interactions. The Debye temperature also limits scattering between electrons and longitudinal optical (LO) phonons at room temperature.

in this work. We observe the characteristic sharp increase in the scattering rate for electrons and holes near $\hbar\omega_{\mathrm{LO}} \sim 80$ meV as longitudinal optical (LO)-phonon emission starts to dominate the electron-phonon interaction. The 2ph rates largely follow the same trend and are on the order of the 1ph rates, consistent with previously published 2ph calculations for GaAs [133, 132] and Si [134]. At 300 K, the 2ph rates are around 50% of the 1ph rates. Prior works have examined the influence of the exchange-correlation functional on charge carrier mobilities, finding variations on the order of ∼10-15% in Si [152] and BAs [120]. Although this uncertainty may influence the predicted absolute mobility values, we expect the relative contribution of 2ph processes compared with 1ph processes to be insensitive to the choice of functional.

2ph processes exhibit several different sub-types because the two phonons involved in scattering can each be emitted or absorbed. Following Ref. [132], processes where a phonon is emitted and another absorbed are denoted 1e1a, and

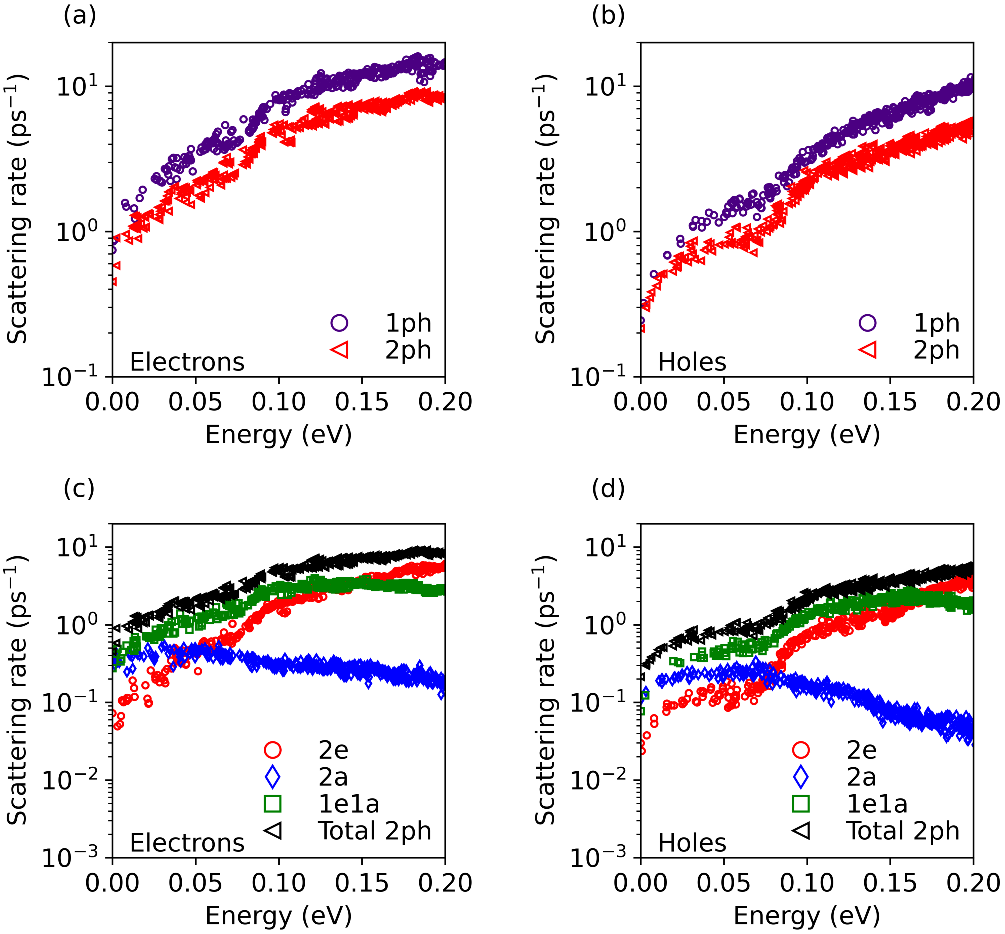

Figure 3.7: Scattering rates vs energy for (a) electrons and (b) holes in BAs including 1ph (circles) and 2ph processes (triangles) at 300 K. The computed 2ph rates for electrons and holes are around 50% of the 1ph rates. Computed total 2ph (triangles), 1e1a (squares), 2a (diamonds), and 2e (circles) scattering rates vs energy for (c) electrons and (d) holes show the sub-processes that comprise the total 2ph rates. Below 150 meV, the 1e1a processes have the largest contribution to the 2ph rates at 300 K.

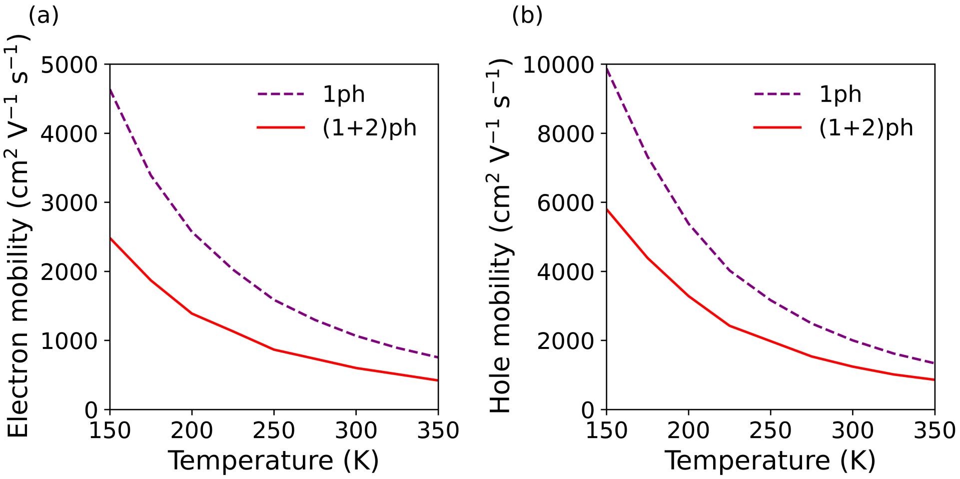

Figure 3.8: Calculations of electron and hole mobility. (a) Electron and (b) hole mobility in BAs vs temperature at the 1ph (dashed line) and (1+2)ph (solid line) level of theory. For holes, the correction to the mobility at room temperature from including 2ph processes is $\sim 37\%$, while for electrons this correction is $\sim 43\%$, demonstrating the significant contribution of 2ph processes to the mobility at room temperature.

processes where two phonons are sequentially emitted or absorbed are 2e and 2a, respectively. The individual sub-processes contributing to the total 2ph rate are shown in Figures 3.7c and 3.7d for electrons and holes, respectively. Below $\hbar\omega_{\mathrm{LO}} \sim 80$ meV, 1e1a processes are dominant. Note that the total 1e1a rate includes processes where a phonon is first emitted and another absorbed, and processes where a phonon is first absorbed and another is subsequently emitted. Two-phonon emission (2e) processes are comparatively weak in this region since LO phonon emission is prohibited until the energy threshold of $2\hbar\omega_{\mathrm{LO}}$. Two-phonon absorption (2a) processes are generally weak throughout the energy range studied, except at sufficiently low energies where emission and therefore 1e1a events become increasingly unlikely such that 2a rates are comparable to 1e1a rates. Between $\hbar\omega_{\mathrm{LO}} \sim 80$ meV and $2\hbar\omega_{\mathrm{LO}}$, the 1e1a and 2e rates increase as LO phonon emission starts to dominate the electron-phonon scattering processes, a feature observed in polar semiconductors [19]. Beyond $2\hbar\omega_{\mathrm{LO}}$, carriers are energetic enough to emit two LO phonons, and 2e processes have the largest contribution to the total 2ph scattering rate. This energy dependence of the individual 2ph sub-processes in BAs is consistent with those reported for GaAs and Si [132, 133, 134].

Electron and hole mobility

We next examine the effect of 2ph processes on the electron and hole mobility. The computed 1ph and (1+2)ph mobility versus temperature is shown in Figures 3.8a and 3.8b for electrons and holes, respectively. With only 1ph processes, we obtain room-temperature electron mobility $\mu_e = 1066$ cm^2 V^{-1} s^{-1} and hole mobility $\mu_h = 2000$ cm^2 V^{-1} s^{-1}, in quantitative agreement with previous 1ph predictions that employ the same PBE exchange-correlation functional (see Supplementary Information of Ref. [120] for calculations using the same functional as in this work). With the inclusion of 2ph processes, μ_e and μ_h decrease to 600 and 1240 cm^2 V^{-1} s^{-1}, respectively, corresponding to a 43 and 37% reduction at room temperature. Over the temperature range from 150 to 350 K, this correction ranges from 36% at 350 K to 41% at 150 K for holes, and 44% at 350 K to 46% at 150 K for electrons. These corrections to the electron mobility are of a comparable magnitude to those obtained for GaAs (∼45%) [133, 132], but slightly higher than those for Si (∼35%) [134].

BAs exhibits several distinct features compared to other polar semiconductors such as GaAs. In GaAs and other polar materials, LO phonons make the overwhelming contribution to electron-phonon scattering [19]. In BAs, carrier scattering relevant to mobility is instead primarily due to acoustic phonons owing to the high optical phonon energy (80 versus 35 meV in GaAs) that limits scattering by LO phonon emission as well as the decreased LO phonon absorption scattering from decreased thermal population [120]. Additionally, in GaAs, intervalley processes have a negligible effect on low-field charge transport because of the Γ-L energy separation of 300 meV, but scattering processes in BAs are more similar to those in Si in that they involve intervalley transfers mediated by zone-edge wave vector phonons. Our calculations reveal that intervalley processes account for 43% of (1+2)ph scattering in BAs at 300 K and 20% at 150 K. The decrease with decreasing temperature occurs due to reduced population of zone-edge phonons required for intervalley scattering. As a comparison, intervalley processes account for 61% of (1+2)ph scattering in Si at 300 K and 25% at 150 K.

Quadrupole effects on the electron mobility

Significant corrections to the carrier mobility have been found in several semiconductors when quadrupole effects are considered. Most notably, in 3C-SiC, the neglect of quadrupoles led to an underestimation $\sim$ 45% of the mobility,

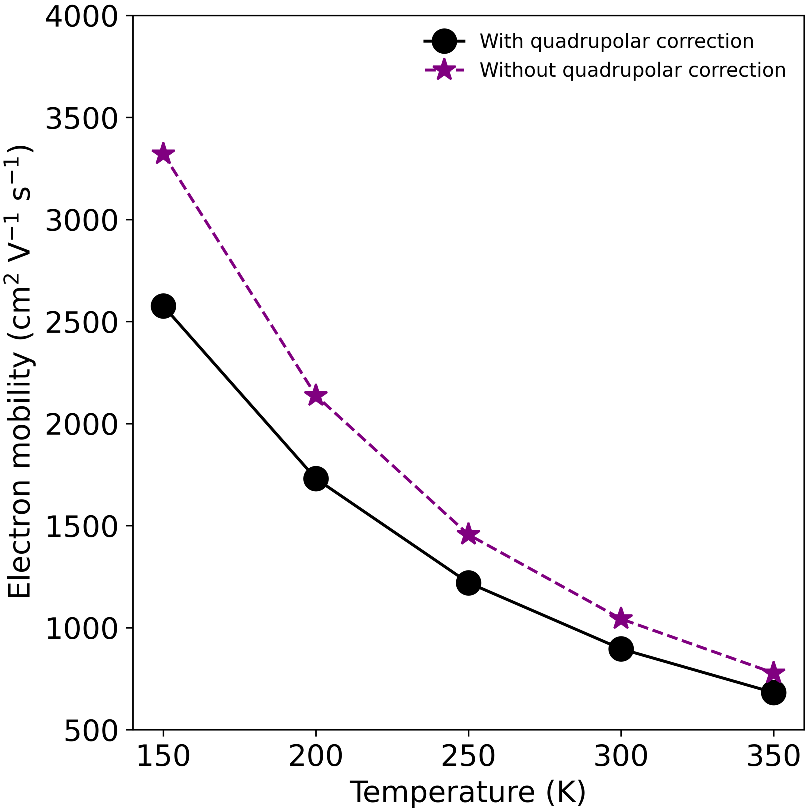

Figure 3.9: 1ph electron mobility versus temperature including quadrupole corrections to the electron-phonon matrix elements and dynamical matrix. Near room temperature, the electron mobility is reduced by $\sim 10\%$. At 150 K, this correction is $\sim 20\%$.

while for c-BN, neglecting quadrupoles overestimated the mobility by $\sim 70\%$ [145]. This effect was minimal on other semiconductors such as Si over a wide temperature range [140, 145]. Given the nature of the impact of quadrupoles on several semiconductors, it is worthwhile to consider their effect on the 1ph mobility in BAs. This is particularly important when we later compare our results to experiments in section 3.6. We computed the quadrupole tensor in BAs and obtained the corresponding effect on its electron mobility at the 1ph level of theory. We obtained $Q_{\mathrm{B}} = 7.64\ e$ bohr and $Q_{\mathrm{As}} = -6.04\ e$ bohr. The computed electron mobility versus temperature including quadrupole corrections to the electron-phonon matrix elements and dynamical matrix is shown in Fig. 3.9.

We can see in Fig. 3.9 that neglecting quadrupoles in BAs leads to an overestimate of the electron mobility. The correction to the electron mobility from including quadrupoles is on the order of 10% near room temperature, and increases as temperature is reduced. At 150 K, the reduction to the electron mobility is around 20%. This correction is similar to results obtained for Si [140].

3.6 Discussion

We now consider our calculated mobility values in the context of recent optical experiments on BAs that reported an ambipolar carrier mobility [126, 127]. At the 1ph level of theory, we predict a high ambipolar mobility $\mu_a = 2\mu_e\mu_h/(\mu_e + \mu_h)$ of 1420 cm^2 V^{-1} s^{-1} at 300 K using 1ph theory, consistent with a prior computed value of 1570 cm^2 V^{-1} s^{-1} with the PBE exchange-correlation functional [120] and in agreement with recent experimental reports [127, 126]. Including 2ph processes reduces μ_a to 810 cm^2 V^{-1} s^{-1}, a 43% reduction. Considering the (1+2)ph mobility value, the apparent agreement between theory and experiment is substantially degraded, with the experiment now overestimating the theory.

This discrepancy could arise from several factors. First, the quantity that was measured in the optical experiments of Refs. [126, 127] was the ambipolar diffusion coefficient of photoexcited charge carriers, from which the mobility was obtained through the Einstein relation. In Refs. [126, 127], the photoexcitation wavelength for determination of the ambipolar diffusion coefficient was chosen to be around the available estimates of the bandgap energy ($\sim$ 2 eV [135, 153, 154, 151]). If the photon energy exceeds the bandgap energy, the photoexcited carriers will have energy in excess of thermal energies, potentially causing the extracted transport properties to differ from their linear-response values. This hot-carrier effect was observed in Ref. [126] and Ref. [127] as a larger measured electronic diffusivity for pump wavelengths $\lesssim$ 500 nm. Evidence for the absence of the hot carrier effect for the final reported diffusivity values was presented, for example, in Fig. 1D of Ref. [126], as the plateau of the measured electronic decay rate with increasing wavelength. On the other hand, scanning ultrafast electron microscopy (SUEM) studies have reported observations of super-diffusion of photoexcited carriers in semiconductors persisting over hundreds of picoseconds [155, 156, 157]. This phenomenon has been attributed to the additional contribution to carrier diffusion of a pressure gradient in the non-degenerate hot carrier gas after photoexcitation [155]. In Refs. [126, 127], the diffusivity was extracted from the electronic decay curve over timescales from tens to hundreds of picoseconds, conceivably leading to an extracted diffusivity that was influenced by super-diffusion.

On the theory side, a possible cause of an underestimate for the computed mobility is the cancellation of the two contributions to electron-phonon scattering at second order. Electron-2ph processes arise from the 1ph term, corresponding to the first derivative of the interatomic potential with respect to lattice displacements taken to second order in perturbation theory, or a direct 2ph term involving the simultaneous interaction of an electron with two phonons with a strength given by second-order derivative of the interatomic potential [158, 159]. These two terms exhibit a non-trivial interaction owing to a cancellation in the long-wavelength acoustic phonon limit which arises from translational invariance of the crystal [160]. In this work and other recent *ab initio* studies of 2ph scattering, only the first term is included, and thus neglect of the second term will lead to an overestimate of 2ph scattering rate. This cancellation has long complicated the study of 2ph scattering in semiconductors [161, 159]. A recent study of 2ph scattering in Si suggested that the correction could be on the order of 10–20% in that material [134]. It is possible that this effect could lead to an underestimate of the computed mobility in BAs; further study is needed to investigate this hypothesis. Lastly, we rule out the effects of quadrupoles as contributing to this discrepancy. In 3C-SiC, neglecting quadrupoles resulted in an underestimate of the 1ph electron mobility by 45% [145]. A similar result in BAs would likely reconcile our 2ph results with experiments; however, as seen in Fig. 3.9, inclusion of quadrupoles reduces the 1ph electron mobility in BAs by around 10% at room temperature, suggesting that the disagreement of our 2ph results with experimental data is not due to the exclusion of quadrupole effects.

Absent higher-quality samples, verifying the prediction of the role of 2ph scattering using transport measurements is challenging due to the contribution of extrinsic defect scattering. We suggest an alternative approach based on continuous wave luminescence spectroscopy which allows the lifetimes of electronic states away from the band minimum to be determined [162]. These states are less influenced by impurity scattering compared to those near the band edge. While the contribution of these higher-energy states to carrier mobility is negligible, the contribution of 2ph processes to the total scattering rate is largely independent of energy, as shown in Fig. 3.7. Therefore, evidence of

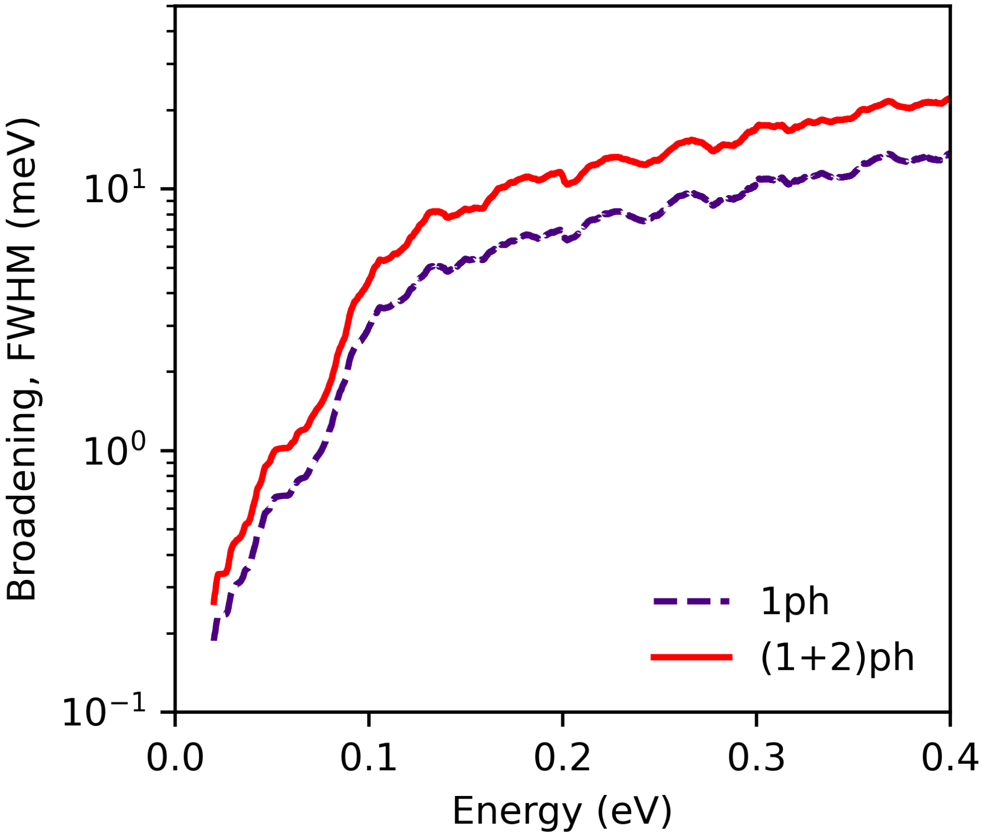

Figure 3.10: Calculated broadening vs energy for electrons due to electron-phonon scattering at 77 K and carrier concentration of 10^{15} cm^{-3}. The difference in broadening between 1ph theory (dashed line) and (1+2)ph theory (solid line) is expected to be distinguishable considering prior reports of experimental uncertainties ∼1 meV [162].

the influence of 2ph scattering on mobility can be obtained by comparing the photoluminescence linewidths of these higher energy states to theory. In these experiments, hot electrons excited by a continuous-wave laser emit photons by recombination, and the spectrum of the emitted light exhibits a broadening that is determined by the lifetime of the state. We may predict the difference in broadening at the 1ph and (1+2)ph levels of theory in BAs using the same *ab initio* theory employed for transport calculations. In Fig. 3.10, we plot the predicted full-width at half-maximum (FWHM) of the luminescence peak, $2\Gamma = \tau^{-1}$, versus energy for electrons. At 0.4 eV above the conduction band minimum (CBM), we predict $2\Gamma \sim 13$ and 21 meV for 1ph and (1+2)ph, respectively. This 8-meV difference is almost an order of magnitude higher than the experimental uncertainty reported in Ref. [162] and thus should be discernible.

3.7 Summary

In summary, we have reported *ab initio* calculations of ambipolar mobility in BAs considering 2ph electron-phonon processes. We find that the inclusion of these processes reduces the predicted electron and hole mobility by 43 and 37% at room temperature, respectively, lowering the ambipolar mobility by 43% and underestimating experimental reports by a similar amount. We hypothesize that the discrepancy between our results and recent optical experiments could in part arise from the super-diffusion of hot carriers, or an underestimation of the calculated mobility owing to cancellations at second-order of perturbation theory. We have suggested an experimental approach based on hot-electron luminescence to test these predictions.

Chapter 4

DRAG-ENHANCED CHARGE CARRIER MOBILITY IN BORON ARSENIDE

The lack of quality bulk BAs samples necessitates the use of unconventional methods to estimate the carrier mobility. As discussed in the previous chapter, one such technique exploits the diffusion of photo-excited carriers to estimate the carrier mobility [126, 127]. In these experiments, a short laser pulse (pump) of wavelength near the bandgap of the material excites electron-hole pairs, and the subsequent diffusion of carriers is monitored with a subsequent pulse (probe). The obtained diffusivity is then converted to ambipolar mobility using the Einstein relation.

However, two potential complications arise regarding the interpretation of the obtained mobility. The first complication is related to the hot carrier effect, as discussed in detail in Chapter 3. The second complication arises from the effect of the induced excess carrier concentration, typically on the order of 10^{19} cm^{-3} [127]. At these carrier densities, approximations which are valid at lower carrier densities–such as that phonons are in equilibrium–may not be justified. This approximation was challenged by Von Peierls in 1930 [163] who argued that the electron-phonon interaction can drag each species out of equilibrium. Later, Gurevich formulated a theory of electron-phonon drag effects [164].

Experimentally, evidence for the effect of drag on the Seebeck coefficient has been observed in Si, Ge, ZnO, and others [165, 166, 167, 168]. The drag effect on mobility is not as easy to observe, due to the fact that the effect on mobility is only significant at high carrier densities. These high densities are usually achieved by doping, but at densities $> 10^{18}$ cm^{-3}, electron-charged impurity scattering becomes a dominant scattering channel such that the drag effect on mobility is masked by the presence of impurities. However, note that high carrier densities can still be achieved without conventional doping methods; for example in modulation doping, where carriers are spatially isolated from impurities, and photo-excitation.

Fully capturing the effect of mutual drag of electrons and phonons within the BTE framework requires solving the fully coupled BTE. In this formalism, the nonequilibrium distribution of the phonon system affects the electronic system as the nonequilibrium distribution of the electronic system affects the phonon system. Prior attempts at this problem include an analytic-computational partially decoupled framework to derive the phonon drag contribution to the Seebeck coefficient in Silicon [169]. Importantly, this work assumed a non-degenerate carrier concentration and a phonon system that is unaffected by the nonequilibrium distribution of the electron system. Ref. [170] utilized a first-principles approach to compute the electron-phonon and phonon-phonon matrix elements, but still ignored the phonon BTE dependence on the deviation of the electron distribution. Other authors have also employed a first-principles approach to solve the partially decoupled BTE [171]. All of these prior attempts used a partially decoupled framework, where the goal was to investigate the effect of a non equilibrium phonon distribution induced by a temperature gradient on the electronic system, while assuming the phonon BTE to be unaffected by the non equilibrium electron distribution. Recently, Protik *et al.* devised a framework to solve the fully-coupled BTE [172], enabling the capability to study the interplay between electrons and phonons as they drive each other out of equilibrium.

There is a growing body of work in the literature on drag in semiconductors using the fully-coupled Boltzmann transport equations. In Ref. [173], Protik and Broido employed solutions to the fully coupled BTE to investigate the mobility, thermal conductivity, and Seebeck coefficient in n-GaAs and found a significant enhancement in the mobility at degenerate carrier concentrations, but no significant contribution to the phonon thermal conductivity from the drag effect. Further, the authors found a significant increase to the absolute value of the Seebeck coefficient at low temperatures. Li *et al.* discovered unexpectedly large increase in the Seebeck coefficient at low temperatures in lightly-doped diamond due to drag, which was attributed to a collapse of anharmonic phonon-phonon scattering rates at low temperatures [174]. Quan *et al.* examined the phonon drag effect in wide band gap GaN and AlN and found prominent enhancements in both the mobility and Seebeck coefficient at room temperature [175]. Li and coauthors found a room temperature drag enhancement of the Seebeck coefficient of p-doped boron arsenide driven by high frequency acoustic phonons [176]. The emerging narrative from these works is one that highlights the importance of considering the non-equilibrium state of electrons and phonons when computing transport coefficients from first principles.

4.1 Coupled electron-phonon BTEs

The coupled electron-phonon Boltzmann transport equations have been given in previous references [177, 173, 175], but we reproduce them here for completeness. For electron and phonon systems in steady state, their BTEs read as:

$$\begin{aligned} \mathbf{v}(\mathbf{k}) \cdot \nabla_{\mathbf{r}} f(\mathbf{k}) + \frac{\mathbf{F}}{\hbar} \cdot \nabla_{\mathbf{k}} f(\mathbf{k}) &= \left.\frac{\partial f(\mathbf{k})}{\partial t}\right|_{\text{coll}} \\ \mathbf{v}(\mathbf{q}) \cdot \nabla_{\mathbf{r}} n(\mathbf{q}) &= \left.\frac{\partial n(\mathbf{q})}{\partial t}\right|_{\text{coll}} \end{aligned} \tag{4.1}$$

where $\mathbf{F}$ is an external force, $\mathbf{v}(\mathbf{k})$ is a velocity vector for an electronic state with wave vector $\mathbf{k}$, $\mathbf{v}(\mathbf{q})$ for phonons with wavevector $\mathbf{q}$. Here, the electron band and phonon branch indices have been suppressed. The distribution functions of electrons and phonons are given by f and n, respectively. The collision terms on the right side of Eq. 4.1 can be generally represented as the following

$$\begin{aligned} \left.\frac{\partial f(\mathbf{k})}{\partial t}\right|_{\text{coll}} &= \left.\frac{\partial f(\mathbf{k})}{\partial t}\right|_{\text{e-ph}} + \left.\frac{\partial f(\mathbf{k})}{\partial t}\right|_{\text{e-imp}} + ... \\ \left.\frac{\partial n(\mathbf{q})}{\partial t}\right|_{\text{coll}} &= \left.\frac{\partial n(\mathbf{q})}{\partial t}\right|_{\text{ph-ph}} + \left.\frac{\partial n(\mathbf{q})}{\partial t}\right|_{\text{ph-e}} + \left.\frac{\partial n(\mathbf{q})}{\partial t}\right|_{\text{ph-imp}} + ... \end{aligned} \tag{4.2}$$

Where the e-ph, e-imp, ph-ph, ph-e, and ph-imp terms represent the collision terms to due to electron-phonon scattering, electron-impurity scattering, phonon-phonon scattering, phonon-electron scattering and phonon-impurity scattering. Under the linearized BTE, which assumes that the electron and phonon distribution functions do not deviate significantly from equilibrium and thus can be expanded about equilibrium, the collision terms can be generally expressed as [177]:

$$\begin{aligned}\left.\frac{\partial f(\mathbf{k})}{\partial t}\right|_{\text{coll}} &= A_{\mathbf{k}}\Delta f(\mathbf{k}) + \sum_{\mathbf{k}'\neq\mathbf{k}} A_{\mathbf{k}'}\Delta f(\mathbf{k}') + \sum_{\mathbf{q}} B_{\mathbf{q}}\Delta n(\mathbf{q}) \\ \left.\frac{\partial n(\mathbf{q})}{\partial t}\right|_{\text{coll}} &= C_{\mathbf{q}}\Delta n(\mathbf{q}) + \sum_{\mathbf{q}'\neq\mathbf{q}} C_{\mathbf{q}'}\Delta n(\mathbf{q}') + \sum_{\mathbf{k}} D_{\mathbf{k}}\Delta f(\mathbf{k})\end{aligned} \tag{4.3}$$

Here, A, B, C, and D are proportionality factors. The deviations in the distribution functions are given as $\Delta f(\mathbf{k}) = f(\mathbf{k}) - f^0(\mathbf{k})$ and $\Delta n(\mathbf{q}) = n(\mathbf{q}) - n^0(\mathbf{q})$. Note that in Eq. 4.3, the collision terms have been separated into two parts: one proportional to the deviation of the distribution of the state of interest, and the second related to the distribution of other states. At one level of approximation, we may ignore the dependence of the collision term of a given state on the other states, in which case we obtain for electrons, $\left.\frac{\partial f(\mathbf{k})}{\partial t}\right|_{\text{coll}} = A_{\mathbf{k}}\Delta f(\mathbf{k})$. This assumes all other states are at equilibrium when evaluating a given state, and thus we only consider only out-scattering. The proportionality factor $A_{\mathbf{k}}$ can then be replaced with an inverse characteristic time, resulting in the familiar relaxation time approximation (RTA). Although this approximation significantly reduces the complexity of the BTE, it comes at the cost of ignoring the coupling between the electron and phonon system. At another level of approximation, we may ignore only the last term on the right hand side of Eq. 4.3 and consider non-equilibrium of other states of the same species which we are solving for. This a valid approximation if one species does not drag the other out of equilibrium. For example, if electrons are at a sufficiently low density and the electron-phonon coupling is weak enough, the change in the phonon distribution $\Delta n(\mathbf{q})$ can be effectively zero such that the last term on the right hand side of Eq. 4.3 disappears.

4.2 Phonon-phonon interaction

A phonon mode is a collective excitation in a crystal lattice, where each atom follows a specific displacement pattern. There is a frequency and wave vector associated with the phonon mode, so that the collective atomic motion is described as a wave propagating through the crystal. The crystal lattice Hamiltonian, including effects of atomic displacements is given as:

$$H_l = U_0 + \sum_i \frac{\mathbf{p}_i^2}{2m_i} + \frac{1}{2!}\sum_{ij}\sum_{\alpha\beta}\Phi_{ij}^{\alpha\beta}u_i^\alpha u_j^\beta + \frac{1}{3!}\sum_{ijk}\sum_{\alpha\beta\gamma}\Phi_{ijk}^{\alpha\beta\gamma}u_i^\alpha u_j^\beta u_k^\gamma + ... \tag{4.4}$$

This expression is a Taylor expansion of the potential about the atomic equilibrium positions. The harmonic and anharmonic force constants are given by $\Phi_{ij}^{\alpha\beta}$ and $\Phi_{ijk}^{\alpha\beta\gamma}$, respectively; i, j, k represent atomic positions in the crystal, and α, β, γ represent the three Cartesian directions. The n-th order force constants, n-th derivatives of energy with respect to atomic displacement, describe how the lattice potential changes with respect to displacements along the atomic degrees of freedom. The 2nd order force constants, $\Phi_{ij}^{\alpha\beta}$, are the harmonic force constants and are used to obtain the phonon dispersion. Truncating the lattice Hamiltonian at 2nd order gives the phonon eigenstates of the system; however, these are not true eigenstates since a state with finite velocity will never scatter and eventually leading to infinte thermal velocity. Therefore, the higher-order terms ($\Phi_{ijk}^{\alpha\beta\gamma}$ and above) termed anharmonic force constants, which act as perturbations, are necessary to correctly describe the system because they are the source of thermal resistance. The perturbations from $\Phi_{ijk}^{\alpha\beta\gamma}$ lead to three-phonon processes where one phonon creates two phonons or two phonons create one phonon.

Including higher order terms in Eq. 4.4 creates additional scattering channels like four-phonon processes, and so on. Four-phonon processes have been found to be important in certain materials, including BAs [178, 124]. The transition rates due to three-phonon processes can be derived with Fermi's Golden Rule. In the linearized BTE formulation, the transition rates are given as [177]:

$$\begin{aligned}\frac{1}{\tau_\mathbf{q}} = \frac{\pi}{\hbar^2 N_\mathbf{q}}\sum_{\mathbf{q}_1,\mathbf{q}_2}|V_{\mathbf{q},\mathbf{q}_1,\mathbf{q}_2}|^2\Big[&(1+n^0_{\mathbf{q}_1}+n^0_{\mathbf{q}_2})\delta(\omega_\mathbf{q}-\omega_{\mathbf{q}_1}-\omega_{\mathbf{q}_2}) + \\ &(n^0_{\mathbf{q}_2}+n^0_{\mathbf{q}_1})[\delta(\omega_\mathbf{q}-\omega_{\mathbf{q}_1}+\omega_{\mathbf{q}_2})-\delta(\omega_\mathbf{q}+\omega_{\mathbf{q}_1}-\omega_{\mathbf{q}_2})]\Big]\end{aligned} \tag{4.5}$$

where the mode indices have been omitted for clarity. $V_{\mathbf{q},\mathbf{q}_1,\mathbf{q}_2}$ is the three-phonon scattering matrix and is constructed from the 3rd order force constants as:

$$V_{\mathbf{q},\mathbf{q}_1,\mathbf{q}_2} = \left(\frac{\hbar}{2}\right)^{3/2}\sum_{\mathbf{R}_i\tau_i\alpha_i}\Phi^{\alpha,\beta,\gamma}_{0\tau,\mathbf{R}_1\tau_1,\mathbf{R}_2\tau_2}\frac{e^{i(\mathbf{q}_1\cdot\mathbf{R}_1+\mathbf{q}_2\cdot\mathbf{R}_2)}e^{\tau\alpha}_{\mathbf{q}}e^{\tau_1\beta}_{\mathbf{q}_1}e^{\tau_2\gamma}_{\mathbf{q}_2}}{(M_\tau M_{\tau_1}M_{\tau_2}\omega_\mathbf{q}\omega_{\mathbf{q}_1}\omega_{\mathbf{q}_2})^{1/2}} \tag{4.6}$$

$N_\mathbf{q}$ is the number of points in the reciprocal space mesh, $\omega_\mathbf{q}$ is the phonon frequency, $n^0_\mathbf{q}$ is the equilibrium phonon distribution, $e^{\tau_1\beta}_\mathbf{q}$ describes the phonon mode displacement pattern, and M_τ is the atom mass at sublattice site τ. Note that crystal momentum conservation is made implicit in these expressions. $\Phi^{\alpha,\beta,\gamma}_{0\tau,\mathbf{R}_1\tau_1,\mathbf{R}_2\tau_2}$ is the 3rd-order force constant and is the third derivative of energy with respect to the displacement of three atomic sites $(0\tau, \mathbf{R}_1\tau_1, \mathbf{R}_2\tau_2)$ along the Cartesian directions (α, β, γ).

It is worth mentioning how the force constants are obtained in practice. The harmonic force constants can be obtained either by DFPT or supercell methods, as mentioned in the Introduction. In the supercell method for the harmonic force constants, a supercell is created by replicating the relaxed unit cell multiple times along the lattice vectors. Within each supercell, a slight displacement of a single atom from its equilibrium position is introduced, and the restoring forces acting on these atoms are computed. To derive the third-order anharmonic force constants, we go through the same procedure but displace two atoms instead.

4.3 Coupled transport of electrons and phonons

Armed with the necessary tools, we may now delve into the procedure to solve the couple e-ph BTEs. The electron non-equilibrium distribution functions can be expanded about its equilibrium value in the presence of weak external fields as:

$$f_\mathbf{k} \approx f^0_\mathbf{k} - \frac{1}{\beta}\partial_{\epsilon_\mathbf{k}} f^0_\mathbf{k}\Psi_\mathbf{k} = f^0_\mathbf{k}[1 + (1 - f^0_\mathbf{k})\Psi_\mathbf{k}] \tag{4.7}$$

where f^0_k is the equilibrium Fermi-Dirac electron distribution, $\beta = \frac{1}{k_B T}$ and k_B is the Boltzmann constant, T is temperature, ϵ_k is electron energy, and Ψ_k is a deviation function. The deviation function is given by:

$$\Psi_\mathbf{k} = -\beta \nabla T \cdot \mathbf{I}_\mathbf{k} - \beta \mathbf{E} \cdot \mathbf{J}_\mathbf{k} \tag{4.8}$$

where $\mathbf{E}$ is the electric field and $\mathbf{I}_\mathbf{k}$, $\mathbf{J}_\mathbf{k}$ are linear response functions to the temperature gradient and electric field. We follow the same procedure for phonons and obtain:

$$n_\mathbf{q} \approx n^0_\mathbf{q}[1 + (1 + n^0_\mathbf{q})\Phi_\mathbf{q}] \tag{4.9}$$

and:

$$\Phi_{\mathbf{q}} = -\beta \nabla T \cdot \mathbf{F}_{\mathbf{q}} - \beta \mathbf{E} \cdot \mathbf{G}_{\mathbf{q}} \tag{4.10}$$

Here, $n_{\mathbf{q}}$ is the equilibrium Bose-Einstein distribution, $\Phi_{\mathbf{q}}$ is the deviation function, $\mathbf{F}_{\mathbf{q}}$ and $\mathbf{G}_{\mathbf{q}}$ are the temperature gradient and electric field response functions. Since phonons are not charged particles and hence cannot couple directly to the electric field, $\mathbf{G}_{\mathbf{q}}$ represents an indirect response that arises from the electron-phonon interaction.

Recall that the coupled set of equations we would like to solve is given by Eq. 4.1. The electron drift term is:

$$\frac{e}{\hbar}\mathbf{E} \cdot \nabla_{\mathbf{k}} f^0_{\mathbf{k}} - \mathbf{v}_{\mathbf{k}} \cdot \nabla T \partial_T f^0_{\mathbf{k}} = \beta f^0_{\mathbf{k}}(1 - f^0_{\mathbf{k}})\Big[-e\mathbf{E} - \frac{\epsilon_{\mathbf{k}} - \mu}{T}\nabla T\Big] \cdot \mathbf{v}_{\mathbf{k}} \tag{4.11}$$

Similarly, the phonon drift term is:

$$-\mathbf{v}_{\mathbf{q}} \cdot \nabla T \partial_T n^0_{\mathbf{q}} = -\beta n^0_{\mathbf{q}}(1 + n^0_{\mathbf{q}})\frac{\hbar\omega_{\mathbf{q}}}{T}\nabla T \cdot \mathbf{v}_{\mathbf{q}} \tag{4.12}$$

where $\mathbf{v}_{\mathbf{q}}$ is the phonon group velocity.

The collision terms of Eq. 4.1 are discussed next. For electrons, the e-ph collision processes that occur at lowest order at 1ph processes, where electrons scatter by absorption(+) or emission(-) of a phonon. The scattering probabilities associated with these processes can be written as:

$$\begin{aligned} X^+_{\mathbf{k},\mathbf{k+q}} &= \frac{2\pi}{\hbar}|g_{\mathbf{kq}}|^2 f^0_{\mathbf{k}}(1 - f^0_{\mathbf{k+q}})n^0_{\mathbf{q}}\delta(\epsilon_{\mathbf{k+q}} - \epsilon_{\mathbf{k}} - \hbar\omega_{\mathbf{q}}) \\ X^-_{\mathbf{k},\mathbf{k+q}} &= \frac{2\pi}{\hbar}|g_{\mathbf{kq}}|^2 f^0_{\mathbf{k}}(1 - f^0_{\mathbf{k+q}})(1 + n^0_{\mathbf{q}})\delta(\epsilon_{\mathbf{k+q}} - \epsilon_{\mathbf{k}} + \hbar\omega_{\mathbf{q}}) \end{aligned} \tag{4.13}$$

where $g_{\mathbf{kq}}$ is the electron-phonon matrix element that was introduced in Eq. 1.6. Linearizing Eq. 4.13, we obtain for the electron-phonon collision term:

$$\partial_t f_{\mathbf{k}}|_{\text{coll}} = \beta \sum_{\mathbf{q}} \left(X^+_{\mathbf{k},\mathbf{k+q}} \begin{bmatrix} \mathbf{I}_{\mathbf{k}} - \mathbf{I}_{\mathbf{k+q}} + \mathbf{F}_{\mathbf{q}} \\ \mathbf{J}_{\mathbf{k}} - \mathbf{J}_{\mathbf{k+q}} + \mathbf{G}_{\mathbf{q}} \end{bmatrix} + X^-_{\mathbf{k},\mathbf{k+q}} \begin{bmatrix} \mathbf{I}_{\mathbf{k}} - \mathbf{I}_{\mathbf{k+q}} - \mathbf{F}_{\mathbf{q}} \\ \mathbf{J}_{\mathbf{k}} - \mathbf{J}_{\mathbf{k+q}} - \mathbf{G}_{\mathbf{q}} \end{bmatrix} \right) \cdot \begin{bmatrix} \nabla T \\ \mathbf{E} \end{bmatrix} \tag{4.14}$$

The top line represents the term due to the temperature gradient and the bottom line represents the term due to the electric field. For phonons, collision processes can be a result of anharmonic phonon interactions (3-phonon) or phonon-electron interactions. There can also be 4-phonon processes but we ignore them in this work. The scattering probabilities due to 3-phonon interactions are given by:

$$W^{\pm}_{\mathbf{q},\mathbf{q}_1,\mathbf{q}_2} = \frac{\pi\hbar}{4}\frac{|V_{\mathbf{q},\mathbf{q}_1,\mathbf{q}_2}|^2}{\omega_{\mathbf{q}}\omega_{\mathbf{q}_1}\omega_{\mathbf{q}_2}}(n^0_{\mathbf{q}}+1)(n^0_{\mathbf{q}_1}+\frac{1}{2}\pm\frac{1}{2})n^0_{\mathbf{q}_2}\delta(\omega_{\mathbf{q}}\pm\omega_{\mathbf{q}_1}-\omega_{\mathbf{q}_2}) \tag{4.15}$$

Similarly, the ph-e scattering probabilities can be computed as:

$$Y_{\mathbf{qk}} = \frac{2\pi}{\hbar}|g_{\mathbf{kq}}|^2 f^0_{\mathbf{k}}(1-f^0_{\mathbf{k+q}})n^0_{\mathbf{q}}\delta(\epsilon_{\mathbf{k+q}}-\epsilon_{\mathbf{k}}-\hbar\omega_{\mathbf{q}}) \tag{4.16}$$

The phonon-phonon and phonon-electron collision terms can then be written as:

$$\begin{aligned}\partial_t n_{\mathbf{q}}|^{3ph}_{\text{coll}} = \beta\sum_{\mathbf{q}_1,\mathbf{q}_2}\Bigg(W^{+}_{\mathbf{q},\mathbf{q}_1,\mathbf{q}_2}\begin{bmatrix}\mathbf{F}_{\mathbf{q}}+\mathbf{F}_{\mathbf{q}_1}-\mathbf{F}_{\mathbf{q}_2}\\ \mathbf{G}_{\mathbf{q}}+\mathbf{G}_{\mathbf{q}_1}-\mathbf{G}_{\mathbf{q}_2}\end{bmatrix}+\\ \frac{1}{2}W^{-}_{\mathbf{q},\mathbf{q}_1,\mathbf{q}_2}\begin{bmatrix}\mathbf{F}_{\mathbf{q}}-\mathbf{F}_{\mathbf{q}_1}-\mathbf{F}_{\mathbf{q}_2}\\ \mathbf{G}_{\mathbf{q}}-\mathbf{G}_{\mathbf{q}_1}-\mathbf{G}_{\mathbf{q}_2}\end{bmatrix}\Bigg)\cdot\begin{bmatrix}\nabla T\\ \mathbf{E}\end{bmatrix}\end{aligned} \tag{4.17}$$

$$\partial_t n_{\mathbf{q}}|^{\text{ph-e}}_{\text{coll}} = 2\beta\sum_{\mathbf{k}}\Bigg(Y_{\mathbf{qk}}\begin{bmatrix}\mathbf{I}_{\mathbf{k}}-\mathbf{I}_{\mathbf{k+q}}+\mathbf{F}_{\mathbf{q}}\\ \mathbf{J}_{\mathbf{k}}-\mathbf{J}_{\mathbf{k+q}}+\mathbf{G}_{\mathbf{q}}\end{bmatrix}\Bigg)\cdot\begin{bmatrix}\nabla T\\ \mathbf{E}\end{bmatrix} \tag{4.18}$$

Phonon response to ∇T

Before discussing the scheme to solve the coupled BTEs, we first define some functions that lend each of the BTEs into the form we desire:

$$Q_{\mathbf{q}} = \sum_{\mathbf{q}_1,\mathbf{q}_2}\left[W^{+}_{\mathbf{q},\mathbf{q}_1,\mathbf{q}_2}+\frac{1}{2}W^{-}_{\mathbf{q},\mathbf{q}_1,\mathbf{q}_2}\right]+2\sum_{\mathbf{k}}Y_{\mathbf{qk}} \tag{4.19}$$

$$\Delta\mathbf{F}^{\text{S}}_{\mathbf{q}} = \frac{1}{Q_{\mathbf{q}}}\sum_{\mathbf{q}_1,\mathbf{q}_2}\left[W^{+}_{\mathbf{q},\mathbf{q}_1,\mathbf{q}_2}(\mathbf{F}_{\mathbf{q}2}-\mathbf{F}_{\mathbf{q}1})+\frac{1}{2}W^{-}_{\mathbf{q},\mathbf{q}_1,\mathbf{q}_2}(\mathbf{F}_{\mathbf{q}2}+\mathbf{F}_{\mathbf{q}1})\right] \tag{4.20}$$

$$\Delta\mathbf{F}^{\text{D}}_{\mathbf{q}} = \frac{2}{Q_{\mathbf{q}}}\sum_{\mathbf{k}}Y_{\mathbf{qk}}(\mathbf{I}_{\mathbf{k+q}}-\mathbf{I}_{\mathbf{k}}) \tag{4.21}$$

$$\mathbf{F}^0_{\mathbf{q}} = \frac{\hbar\omega_{\mathbf{q}}\mathbf{v}_{\mathbf{q}}n^0_{\mathbf{q}}(1+n^0_{\mathbf{q}})}{Q_{\mathbf{q}}T} \tag{4.22}$$

The set of equations above defines the phonon response to a temperature gradient, where we have defined self (S) and drag (D) terms that are functionals of the phonon electron deviation function, respectively. The phonon BTE due to the temperature gradient is then:

$$\mathbf{F}_{\mathbf{q}} = \mathbf{F}^{0}_{\mathbf{q}} + \Delta\mathbf{F}^{\mathrm{S}}_{\mathbf{q}} + \Delta\mathbf{F}^{\mathrm{D}}_{\mathbf{q}} \tag{4.23}$$

An important thing to note in Eq. 4.23 is that the drag term $\Delta\mathbf{F}_{\mathrm{D},\mathbf{q}}$ represents the effect of non-equilibrium electrons on phonon transport. If it is assumed that during the e-ph interaction, electrons remain at equilbrium, then $\Delta\mathbf{F}_{\mathrm{D},\mathbf{q}} = 0$ and there will be no drag contribution to the phonon BTE.

Phonon response to electric field

The phonon system does not respond directly to the electric field. The indirect effect of the electric field on the phonon system occurs via the e-ph interaction: that is, the electric field can drive electrons out of equilibrium, which would then be felt by the phonon system through ph-e scattering. Self and drag functions can be defined as:

$$\Delta\mathbf{G}^{\mathrm{S}}_{\mathbf{q}} = \frac{1}{Q_{\mathbf{q}}} \sum_{\mathbf{q}_1,\mathbf{q}_2} \left[W^{+}_{\mathbf{q},\mathbf{q}_1,\mathbf{q}_2} (\mathbf{G}_{\mathbf{q}_2} - \mathbf{G}_{\mathbf{q}_1}) + \frac{1}{2} W^{-}_{\mathbf{q},\mathbf{q}_1,\mathbf{q}_2} (\mathbf{G}_{\mathbf{q}_2} + \mathbf{G}_{\mathbf{q}_1}) \right] \tag{4.24}$$

$$\Delta\mathbf{G}^{\mathrm{D}}_{\mathbf{q}} = \frac{2}{Q_{\mathbf{q}}} \sum_{\mathbf{k}} Y_{\mathbf{qk}} (\mathbf{J}_{\mathbf{k}+\mathbf{q}} - \mathbf{J}_{\mathbf{k}}) \tag{4.25}$$

The phonon BTE due to the electric field becomes:

$$\mathbf{G}_{\mathbf{q}} = \Delta\mathbf{G}^{\mathrm{S}}_{\mathbf{q}} + \Delta\mathbf{G}^{\mathrm{D}}_{\mathbf{q}} \tag{4.26}$$

Electron response to electric field

We go through a similar formulation for electrons. We first define the e-ph scattering probability including both absorption and emission as:

$$R_{\mathbf{k}} = \sum_{\mathbf{k}} \left(X^{+}_{\mathbf{k},\mathbf{k}+\mathbf{q}} + X^{-}_{\mathbf{k},\mathbf{k}+\mathbf{q}} \right) \tag{4.27}$$

Then the self and drag terms:

$$\Delta\mathbf{J}^{\mathrm{S}}_{\mathbf{k}} = \frac{1}{R_{\mathbf{k}}}\sum_{\mathbf{q}}\mathbf{J}_{\mathbf{k}+\mathbf{q}}\big(X^{+}_{\mathbf{k},\mathbf{k}+\mathbf{q}} + X^{-}_{\mathbf{k},\mathbf{k}+\mathbf{q}}\big) \tag{4.28}$$

$$\Delta\mathbf{J}^{\mathrm{D}}_{\mathbf{k}} = \frac{1}{R_{\mathbf{k}}}\sum_{\mathbf{q}}\big(X^{-}_{\mathbf{k},\mathbf{k}+\mathbf{q}}\mathbf{G}_{-\mathbf{q}} - X^{+}_{\mathbf{k},\mathbf{k}+\mathbf{q}}\mathbf{G}_{\mathbf{q}}\big) \tag{4.29}$$

The electron BTE due to the electric field is:

$$\mathbf{J}_{\mathbf{k}} = \mathbf{J}^{0}_{\mathbf{k}} + \Delta\mathbf{J}^{\mathrm{S}}_{\mathbf{k}} + \Delta\mathbf{J}^{\mathrm{D}}_{\mathbf{k}} \tag{4.30}$$

where $\mathbf{J}^{0}_{\mathbf{k}} = \frac{e}{R_{\mathbf{k}}}f^{0}_{\mathbf{k}}(1 - f^{0}_{\mathbf{k}})\mathbf{v}_{\mathbf{k}}$.

Electron response to ∇T

The self and drag terms for the electron BTE due to the temperature gradient are:

$$\Delta\mathbf{I}^{\mathrm{S}}_{\mathbf{k}} = \frac{1}{R_{\mathbf{k}}}\sum_{\mathbf{q}}\mathbf{I}_{\mathbf{k}+\mathbf{q}}\big(X^{+}_{\mathbf{k},\mathbf{k}+\mathbf{q}} + X^{-}_{\mathbf{k},\mathbf{k}+\mathbf{q}}\big) \tag{4.31}$$

$$\Delta\mathbf{I}^{\mathrm{D}}_{\mathbf{k}} = \frac{1}{R_{\mathbf{k}}}\sum_{\mathbf{q}}\big(X^{-}_{\mathbf{k},\mathbf{k}+\mathbf{q}}\mathbf{F}_{-\mathbf{q}} - X^{+}_{\mathbf{k},\mathbf{k}+\mathbf{q}}\mathbf{G}_{\mathbf{q}}\big) \tag{4.32}$$

The electron BTE for a temperature gradient reads:

$$\mathbf{I}_{\mathbf{k}} = \mathbf{I}^{0}_{\mathbf{k}} + \Delta\mathbf{I}^{\mathrm{S}}_{\mathbf{k}} + \Delta\mathbf{I}^{\mathrm{D}}_{\mathbf{k}} \tag{4.33}$$

where $\mathbf{I}^{0}_{\mathbf{k}} = \frac{\epsilon_k - \mu}{R_{\mathbf{k}}T}f^{0}_{\mathbf{k}}(1 - f^{0}_{\mathbf{k}})\mathbf{v}_{\mathbf{k}}$.

We have now developed the set of equations (4.23, 4.26, 4.30, 4.33) we would like to solve to obtain quantities of interest. In these equations, terms with "0", "S", "D" subscripts are RTA terms, self terms, and drag terms respectively. The RTA terms include only out-scattering processes and represent a direct coupling to the external field, which is why there is no RTA term for the phonon electric field BTE in Eq. 4.26. The self terms are functionals of the response function of the respective species and are the in-scattering corrections. Considering terms only up to the self term is the typical approximation made in *ab initio* studies today as the phonons (electrons) are assumed in equilibrium in the electron (phonon) BTE. Excluding drag terms renders the BTEs a decoupled set of equations. The drag terms are functionals of the response functions of the other species, lifting the assumption that those species remain in equilibrium. Within this framework, we are able to investigate the effect of a non-equilibrium phonon (electron) distribution on electron (phonon) transport. Accordingly, each pair of BTEs (corresponding to each field) must be solved in a self consistent manner as they become tightly coupled from the inclusion of drag terms.

4.4 Procedure to solve BTEs

The BTEs are solved using the now-standard iterative scheme that have been well-described in several works (see, for example, Ref. [179]). Briefly, one starts with the RTA terms as a zeroth order solution. In the next iteration, this solution is fed into the BTE to obtain the self and drag terms, and this process is continued until convergence. The key difference here is that we are not solving a single BTE. Here, for each coupled BTE and for each phonon BTE iteration, the electron BTE is first iterated to self consistency. Therefore, once the phonon BTE is converged, the electron BTE is converged as well. This approach is physically justified because the electron system is typically significantly faster than the phonon system.

Once the BTEs are solved for the response functions, we may obtain transport coefficients such as the electrical conductivity, σ and Seebeck coefficient, S. The tensors are given by:

$$\begin{bmatrix} \sigma \\ \sigma S \end{bmatrix} = \frac{2e}{Vk_BT} \sum_{\mathbf{k}} f^0_{\mathbf{k}}(1 - f^0_{\mathbf{k}}) \mathbf{v}_{\mathbf{k}} \otimes \begin{bmatrix} \mathbf{J}_{\mathbf{k}} \\ \mathbf{I}_{\mathbf{k}} \end{bmatrix} \tag{4.34}$$

Computational details

The following quantities are required for a full solution of the coupled electron-phonon BTEs: second and third order interatomic force constants, which were obtained from Quantum Espresso and thirdorder.py [180], respectively; the dynamical matrix, e-ph matrix elements, real space cell maps and degeneracies, and the electronic Hamiltonian in Wannier space generated from EPW [150]. For Quantum Espresso calculations, we use norm conserving pseudopotentials with a Perdew, Burke, and Ernzerhof (PBE) exchange-correlation functional. The relaxed lattice constant was 4.8155 Å. We used a 12^3 $\mathbf{k}$ grid for SCF and NSCF calculations, and a 6^3 $\mathbf{q}$ grid for the phonon calculations. The third order force constants were calculated using a 3 × 3 × 3 supercell with five nearest neighbor cut-off. The `elphbolt` package was used to to solve the coupled BTEs [172]. The fine $\mathbf{k}$ and $\mathbf{q}$ grid of 150^3 and 50^3, respectively where used for the transport calculations, and the energy window was set to 400 meV below and above the conduction band minimum.

4.5 Results

Scattering rates

Electron scattering rates versus electron energy as shown in Figure 4.1 at 50 K and 300 K. We observe the characteristic kink around the optical phonon energy of 80 meV, corresponding to the onset of optical phonon emission. Below 80 meV, the rates are dominated by phonon absorption and emission processes. The scattering rates at 50 K are lower than at 300 K due to reduced phonon population at lower temperatures. Finally, note that the 300 K rates are in quantitative agreement with the 1ph results in Fig. 3.7a, showing that our approach is relatively robust to choice of pseudopotential and exchange-correlation functional.

We next discuss the phonon-phonon and phonon-electron RTA scattering rates versus phonon energy at 300 K and a nondegenerate carrier concentration of 5×10^{16} cm^{-3} as shown in Fig. 4.2. The black circles are phonon-phonon scattering rates and the red triangles are phonon-electron scattering rates. We notice that there is a gap on the x axis of Fig. 4.2 which is a result of the acoustic-optical gap in the phonon dispersion of BAs, so there are no phonons in that range of energy to participate in scattering processes. The coupled e-ph system exchange momenta. Momenta received by phonons from the electronic system can either be dissipated by scattering with other phonons or scattering with electrons, the latter which will lead to enhancement of electron transport properties [181]. At the same time, reduced phonon-phonon momentum dissipation due to extra momentum from the electron system can enhance the phonon transport coefficients. Although we do not consider the electron drag effect on phonon transport in this work, other studies have shown this effect to be overall, minimal [181, 173].

Importantly, observe that the phonon-electron scattering rates are orders of magnitude lower than the phonon-phonon scattering rates at this carrier concentration. The strength of phonon-electron scattering relative to phonon-

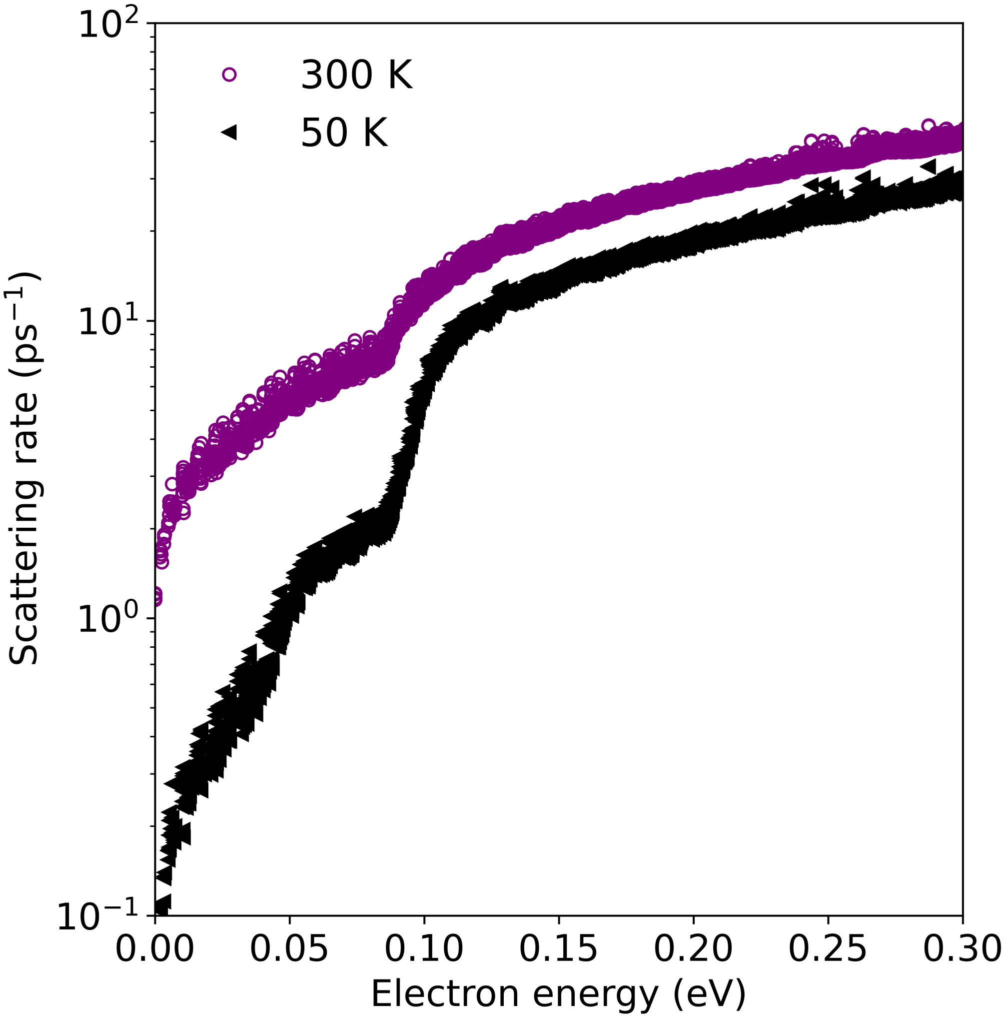

Figure 4.1: Electron-phonon scattering rates in BAs at 50 and 300 K. The rates at 50 K are lower than the rates at 300 K due to a reduced phonon population at lower temperatures. These calculations using a norm conserving pseudopotential agree with the results in Chapter 3 where we employed an ultrasoft pseudopotential, showing the robustness of this approach to specific choices of pseudopotential.

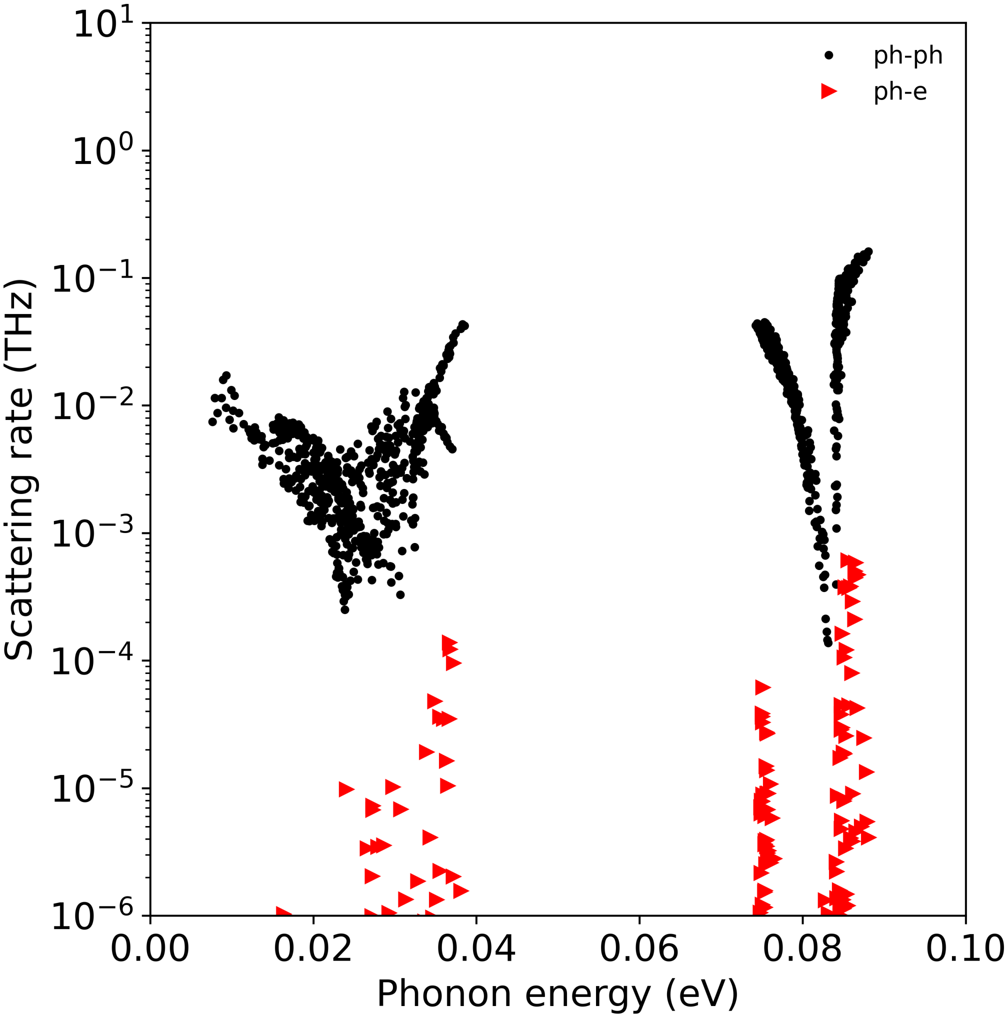

Figure 4.2: Phonon scattering rates in BAs at 300 K and a carrier concentration of 10^{16} cm^{-3}. Phonon-phonon scattering rates dominate phonon-electron rates at this temperature and carrier density. The gap on the x axis is a result of the acoustic-optical gap in the phonon dispersion of BAs, and there are no phonons in that range of energy to participate in scattering processes.

phonon scattering determines the magnitude of the drag effect. If phonon-electron scattering is relatively strong, then there will be significant momentum mixing between the systems and electrons will dissipate less momentum overall. At this temperature and carrier concentration, phonon-electron scattering rates are relatively weak and thus not expected to result in a significant enhancement of the electron mobility.

Conversely, the phonon-phonon and phonon-electron RTA scattering rates versus phonon energy at a degenerate carrier concentration of 10^{19} cm^{-3} are shown in Fig. 4.3. In comparison to Fig. 4.2, we observe that the phonon-electron scattering rates in Fig. 4.3 are significant. This is due to the strong electron-phonon interaction that arises from the position of the chemical potential in the conduction band, increasing the phase space for electron-phonon scattering. Thus at high carrier concentrations, flow of momentum back into the electronic system is more likely.

Qualitatively, we can understand this phenomenon as follows. When we assume an equilibrium distribution of phonons at a particular physical or lattice temperature, what we are saying is that electron-phonon scattering happens on a timescale much longer than the time it takes the phonon system to redistribute back to equilibrium, such that the electrons always "see" an equilibrated phonon system. That means that we have assumed the phonon-phonon scattering rates are much larger than the phonon-electron scattering rates. As we've seen in Fig. 4.3, this is not always the case and in these cases electrons can "see" a nonequilibrium phonon distribution that needs to be accounted for in the BTE.

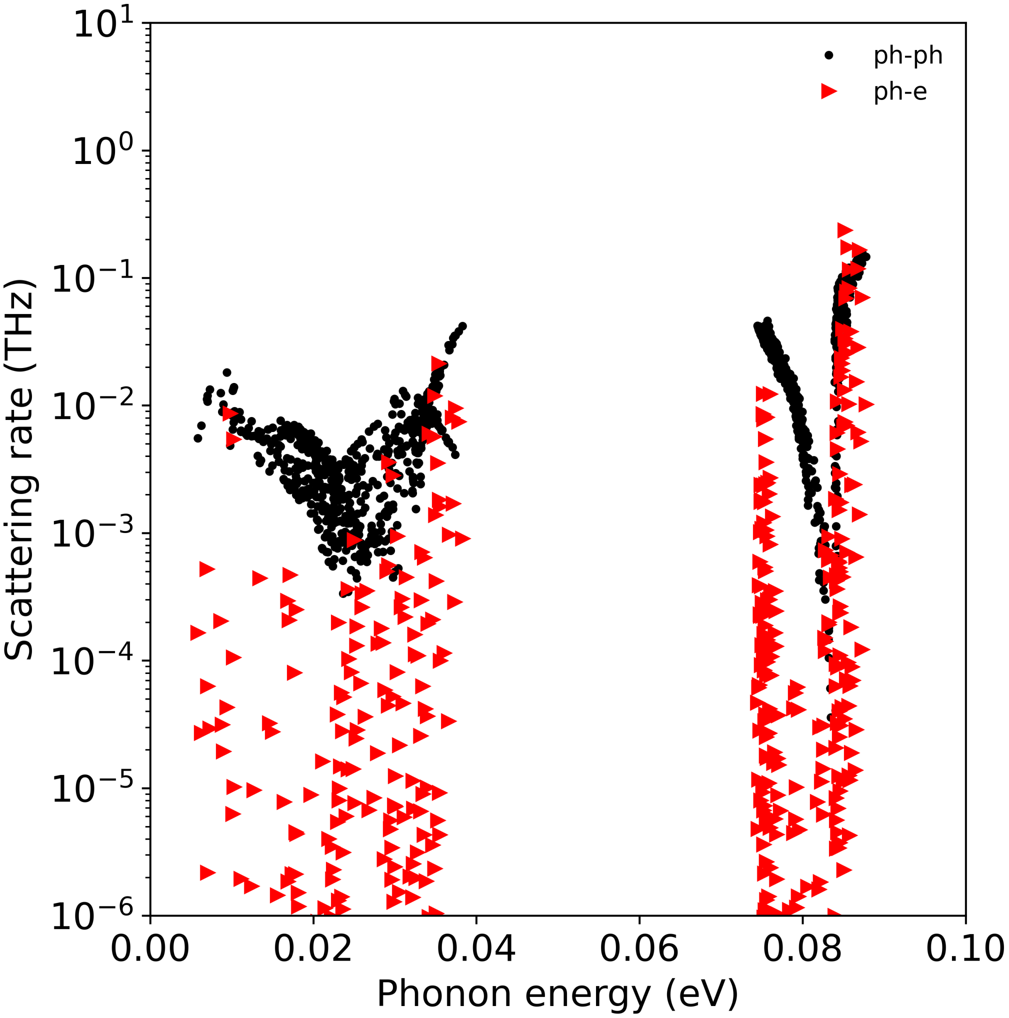

Figure 4.3: Phonon scattering rates in BAs at 300 K and a carrier concentration of 10^{19} cm^{-3}. At this temperature, ph-ph rates dominate ph-e rates but ph-e rates are also significant. Phonon-electron scattering facilitates momentum circulation between the electron and phonon system.

We next examine the dependence of the phonon scattering rates on temperature. The scattering rates at 50 K are shown in Fig. 4.4. We first note that the scattering rates are lower overall at 50 K compared to the rates at 300 K. This is expected and a consequence of the phonon population decreasing with temperature. Secondly, the relative magnitude of phonon-electron rates with respect to the phonon-phonon rates is higher at 50 K versus 300 K. This indicates that even though the scattering rates decrease with temperature, the phonon-phonon rates decrease more rapidly than the phonon-electron rates, suggesting that the drag effect may be stronger at lower temperatures.

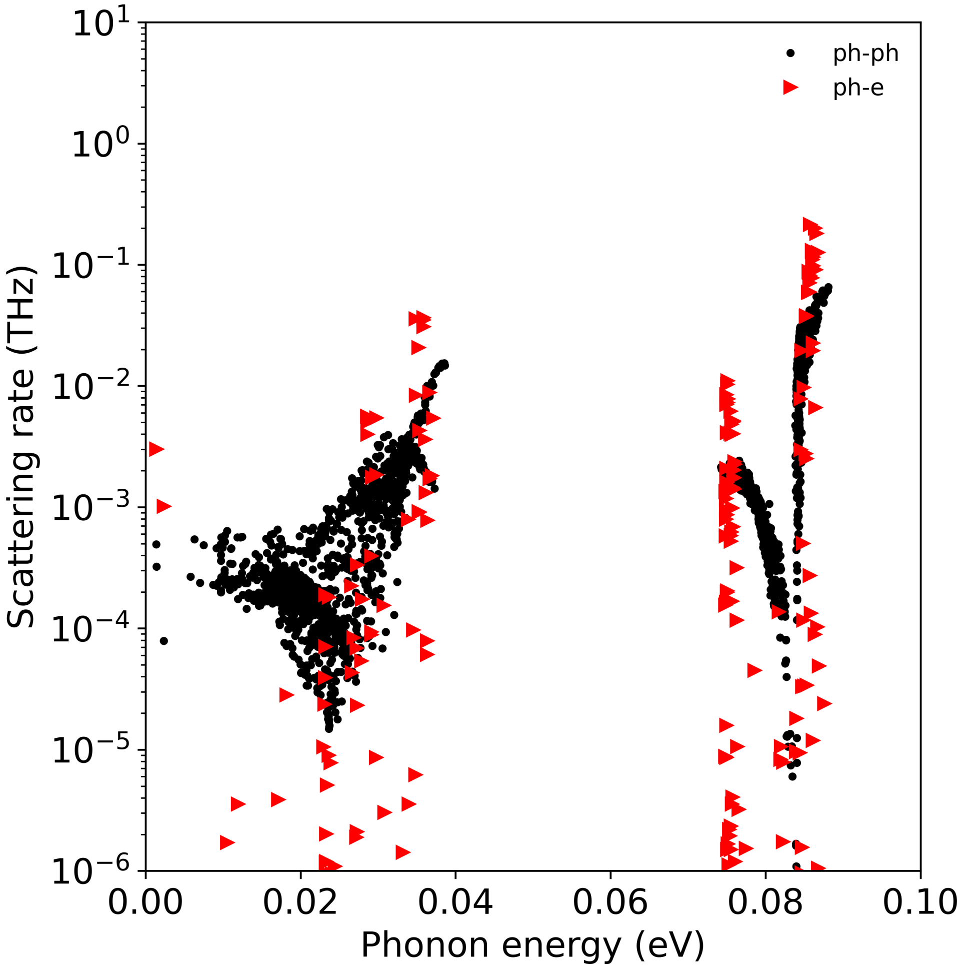

Figure 4.4: Phonon scattering rates in BAs at 50 K and a carrier concentration of 10^{19} cm^{-3}. At this temperature, ph-e scattering dominates ph-ph scattering due to the reduction in phonon population at lower temperatures.

Phonon drag effect on electron mobility

We now proceed to the effect of phonon drag on the electron mobility. Let's recall that in the typical *ab initio* treatment of mobility, the effect of phonon drag is ignored and assumed negligible. Therefore the electron-phonon interaction is always a momentum-dissipative process for electrons as they lose momenta to the thermal (phonon) bath. However, when phonons are not assumed in equilibrium momentum mixing can occur. This picture is closer to the physical microscopic process because momentum must be conserved as electrons transfer their momenta to phonons. The transfer of momentum can drive phonons out of equilibrium and the phonons can then dissipate this excess momentum through anharmonic phonon-phonon interaction, phonon-electron scattering, and phonon-defect scattering. Note that in this work we assume a pure sample and ignore impurity/defect effects.

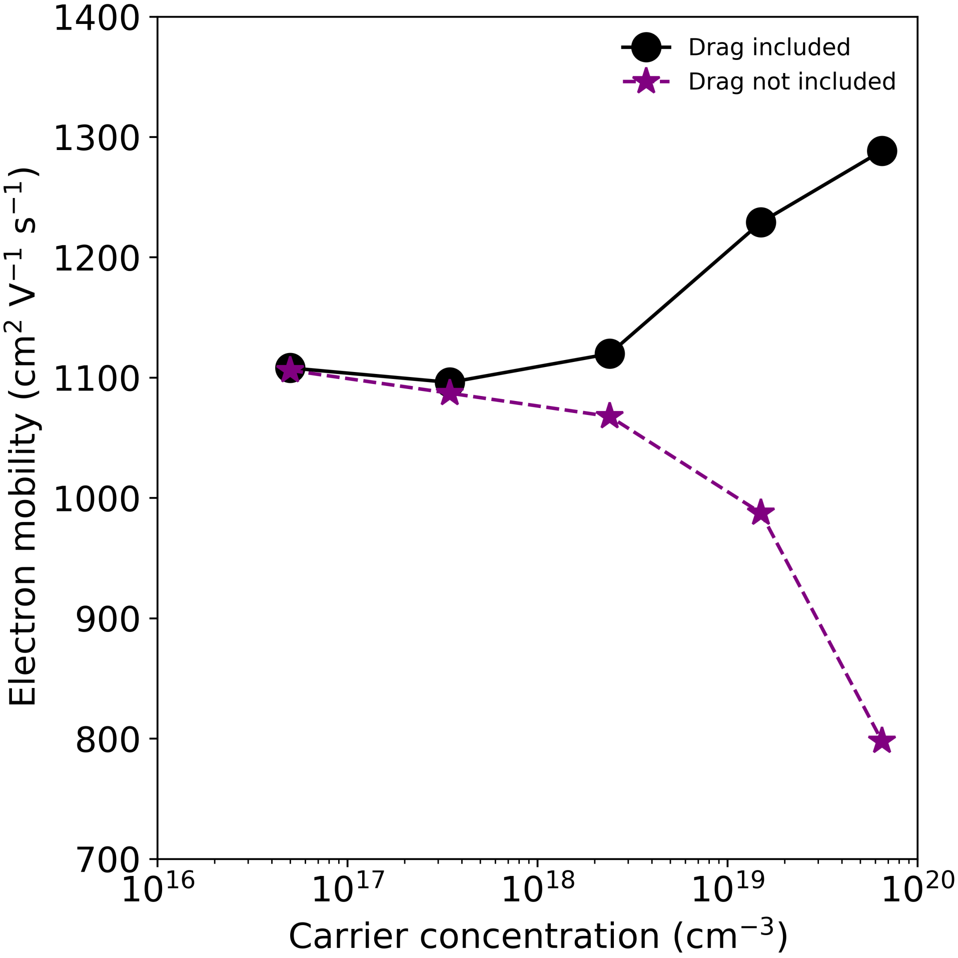

Figure 4.5: Electron mobility at 300 K versus carrier concentration in BAs, showing results for drag-included and drag-excluded processes. Without including drag, we observe a decrease in the mobility with concentration at degenerate densities. This is a result of the larger phase space for electron-phonon scattering. When drag is included in the calculation, the stronger electron-phonon interaction at high densities drives momentum mixing between the systems and enhances the drag effect, resulting in competing mechanisms for the drag-included processes and a resulting increasing trend of the electron mobility with concentration.

Figure 4.5 shows the computed electron mobility as a function of carrier concentration in BAs, including and excluding drag effects. Without drag (black circles), we observe a decrease in the mobility with concentration at these carrier densities. This decrease is a result of the larger phase space for electron-phonon scattering associated with the degenerate carrier density.

At low carrier concentrations where the chemical potential is in the band gap, electrons primarily interact with low-energy acoustic phonons in a quasi-elastic fashion. However, at high carrier concentrations when the chemical potential is in the conduction band, the phase space for electron-phonon scattering increases as there are contributions from all types of phonons, which in turn decreases the electron lifetime and mobility. When drag is included (red triangles) however, there is a different trend with carrier density that arises from two competing factors: stronger electron momentum dissipation processes and momentum mixing with the phonon system. The mobility increases with density as a result of the nonequilibrium phonon distribution created by the high carrier density, and this phonon distribution pumps momentum back into the electronic system as part of its own momentum-dissipative processes. This momentum mixing process is what acts to enhance the electron mobility, and has been observed in other compound semiconductors such as GaAs and GaN [173, 175].

To quantify this effect, the computed mobilities with and without drag at 5×10^{16} cm^{-3} as shown in Fig. 4.5 are 1108 and 1106 cm^2 V^{-1} s^{-1}, respectively, while at 6.5×10^{19} cm^{-3}, the calculated values are 1290 and 800 cm^2 V^{-1} s^{-1}, respectively.

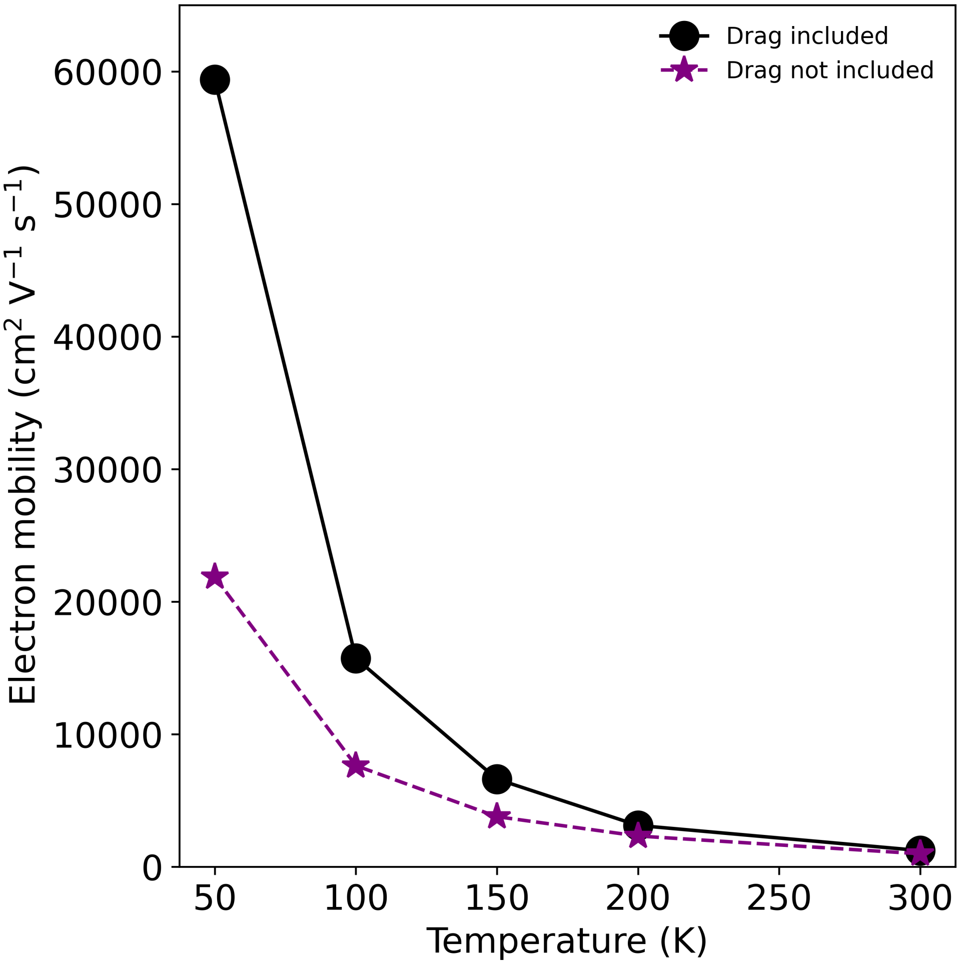

Figure 4.6: Electron mobility versus temperature in BAs, showing results for drag-included and drag-excluded processes at a carrier concentration of 10^{19} cm^{-3}. The mobility gain from drag increases as temperature decreases, and is almost an order of magnitude greater at 50 K than it is at 300 K.

Next, we examine the dependence of the electron mobility on temperature. We previously discussed the dependence of the phonon RTA scattering rates on temperature and noticed that the phonon-electron scattering rates were stronger in relative magnitude to phonon-phonon rates at 50 K compared to 300 K. This indicates that the relative amount of momenta transferred back into the electronic system is greater at 50 K, and thus should reflect in the electron mobility. We confirm this expectation in Fig. 4.6. At a carrier concentration of 10^{19} cm^{-3}, the mobility gain from drag increases as temperature is reduced, and is almost an order of magnitude greater at 50 K than it is at 300 K. The computed electron mobility excluding drag effects at 300 K is 990 cm^2 V^{-1} s^{-1}, whereas with drag included the mobility is 1230 cm^2 V^{-1} s^{-1}, an increase of $\sim$ 25%. At 50 K, the respective values are 21875 cm^2 V^{-1} s^{-1} and 59375 cm^2 V^{-1} s^{-1}.

It is worth mentioning that due to the computational cost associated with solving the coupled BTEs ($\sim$ 2000 − 3000 CPU hours per calculation), we limited our $\mathbf{k}$ and $\mathbf{q}$ grids to 150^3 and 50^3, respectively. A denser grid may alter our results somewhat, as shown in Fig. 10 of Ref. [175].

4.6 Discussion

The demonstration of drag-enhanced electron mobility in BAs is an important development, especially in the context of the results of Chapter 3. In Chapter 3, we found that electron-two-phonon processes played an important role in the carrier mobility, with corrections around $\sim$ 40% to the mobility predicted with only 1ph processes. This is in contrast to experimental reports [127, 126] that appear in agreement with the 1ph mobility. Our results here indicate, in addition to the hot carrier effect and the direct 2ph contribution we do not include in our calculations, another possible contribution to the discrepancy between our results and the experimental results: at high carrier concentrations for which the experiments were conducted, phonons may be dragged out of equilibrium thus resulting in an increase of the mobility.

Note that we do not consider electron-two-phonon processes or higher order phonon-phonon (four phonon) processes in this chapter. Even though we don't expect the outcome from this chapter's results to be significantly affected by the inclusion of electron-two-phonon processes, it is known that four phonon processes are important in BAs, and their inclusion could affect the computed drag-enhanced mobility because of the added phonon-phonon scattering mechanism which restore phonons back to equilibrium faster [124, 176]. We also do not include electron scattering with ionized impurities, which is physically justified in our case because we assume a carrier concentration obtained by photoexcitation of a pristine sample.

Further, we have neglected electron-electron interactions in this work. Electron-electron interactions are important to thermalize an initial unknown degenerate carrier distribution to a hot Fermi-Dirac distribution on the fs timescale [182, 183]. At high carrier concentrations, the low field mobility may also be influenced by electron-electron interactions, although clear and conclusive evidence for this is missing due to the increased strength of carrier-impurity scattering at these densities. We note that while several works have attempted to include electron-electron interactions within the framework of the BTE with varying approximations [183], a full first-principles framework for this problem has not yet been developed as of this writing. Therefore, a quantitative understanding of electron-electron scattering on the low field mobility in semiconductors is presently lacking.

Let us now conclude by revisiting our motivation for investigating phonon drag in boron arsenide. Recall that current estimates of the carrier mobility in boron arsenide are from three primary sources: *ab initio* calculations employing the lowest order of perturbation theory (1ph), calculations employing higher order perturbation theory (2ph, our work, Chapter 3), and pump-probe experiments that track diffusion of photoexcited carriers. The 1ph theory and photoexcitation experiments are seemingly in agreement, but our 2ph work underestimates these results by around 40%. We suspect that this disagreement could be a result of one or a combination of the following factors. One factor is the potential cancellation of different types of 2ph processes as discussed in Chapter 3 that could lead to a $\sim 10-20\%$ underestimate of the mobility in our calculations. Secondly, the hot carrier effect could overestimate the carrier mobility from experiments. Another reason for the discrepancy could be the induced high carrier concentration, on the order of 10^{19} cm $^{-3}$ [127]. In fact, the hot carrier effect and phonon drag could simultaneously inflate the experimental values. What we have demonstrated in this chapter is that at these high densities, the obtained experimental carrier mobility may be enhanced due to momentum circulation between the electron and phonon systems, potentially partly accounting for the discrepancy between our two-phonon results in Chapter 3 and experiment.

4.7 Summary

In this chapter, we explored the coupled electron-phonon Boltzmann transport equations where the solution to each of the BTEs requires knowledge of the non equilibrium distribution of the other species. We demonstrated that the coupled BTEs can be solved in an iterative fashion, where we start with the zeroth order solution and iterate until we obtain the self and drag terms. Importantly, because the electron system tends to be overall faster than the phonon system, the BTEs are solved such that for each phonon BTE iteration, the electron BTE is first iterated to self consistency. We then showed from solutions of the coupled electron-phonon BTEs that the assumption of an equilibrium phonon distribution when solving the electron BTE is not justified at high carrier concentrations. Particularly, there is a 25% increase in the mobility at 300 K and a carrier concentration of 10^{19} cm^{-3} when the drag effect is included versus when it is not included. The phonon drag enhancement of electron mobility is temperature-dependent and strongest at low temperatures. At high carrier concentrations, there are two main competing factors with regard to the mobility. One is the reduction in mobility that comes from a larger phase space for electron-phonon scattering which leads to electronic momentum dissipation, and the other is the increased mixing between electrons and phonons that tends to enhance the mobility. We showed that when drag is included in our calculations, the mobility increases with carrier concentration, whereas the mobility decreases with increased concentration when drag is not included. Our results reveal important phenomena about the coupled transport of electrons and phonons in boron arsenide.

Chapter 5

CONCLUSION AND OUTLOOK

This thesis has centered on investigations of transport in semiconductors and semiconductor devices. In Chapter 1, we introduced a class of semiconductor devices called HEMTs which are widely used to build low-noise amplifiers in fields like radio astronomy and quantum computing. We discussed their noise characteristics and the importance of material properties like carrier mobility and thermal conductivity on device performance, which then prompts us to investigate potential materials with desirable properties.

In Chapter 2, we suggested techniques to achieve better noise performance in HEMTs by proposing a new theory of drain noise based on real-space transfer of electrons out of the quantum well of the device. This theory is based on a general formulation of partition noise that occurs when charge carriers have multiple paths to arrive at a terminal. We found that an explanation based on this theory was able to account for various dependencies of the observed noise. In particular, there is a critical dependence of the noise on the magnitude of the conduction band offset formed between channel and barrier that helps unravel strategies to realize devices with lower noise figure. A larger conduction band offset in HEMTs helps to maximize the channel sheet density. According to our theory, a large offset is also beneficial to minimize the transfer of electrons into the adjacent layer, which in turn would possibly improve the noise performance. To minimize the transfer, the electron temperature could be reduced which would reduce the population of electrons able to thermionically emit out of the quantum well. This can be achieved by adjusting the elemental composition of the compound semiconductor that makes up the channel. However, this adjustment must be carefully balanced with the requirement for high mobility. Alternatively, an increase in the conduction band offset can be attained without affecting the channel by adjusting the elemental composition in the adjacent barrier layer, instead of the channel. In any case, these adjustments must be made while carefully accounting for the potential of lattice mismatch that can lead to the formation of misfit dislocations that negatively impact the noise.

In Chapter 3, we employed first principles methods to investigate charge transport in boron arsenide, a material which, due to its exceptionally high thermal conductivity could potentially be integrated into various technological applications in the future, including HEMTs. By including higher-order electron-phonon scattering processes (2ph), we find that the predicted electron and hole mobility is significantly reduced compared to the lowest level of perturbation theory involving one electron and one phonon (1ph). Our results are in apparent disagreement with recent experimental reports that employ diffusion of photoexcited charge carriers to estimate the mobility. We proposed that the experimental origin of the discrepancy could arise from the superdiffusion of hot carriers shortly after photoexcitation, an effect which has been observed using scanning ultrafast electron microscopy. Furthermore, the induced excess carrier concentration in photexcitation could be potentially responsible for an inflation of the experimentally-obtained mobility. On the theory side, the predicted value of the mobility could be underestimated as a result of a nontrivial cancellation between the iterated and direct contributions to 2ph scattering, the latter of which we neglect in our work. We also consider quadrupolar corrections to the electron-phonon matrix elements and dynamical matrices as another potential source of error in our work, but we found no significant difference between the mobility computed by including dynamical quadrupoles versus when dynamical quadrupoles are excluded. To test our predictions given the defective samples presently available, we suggested an experimental approach based on direct measurements of hot-carrier lifetimes using.

As discussed, one of the potential reasons for the disagreement between our work and experiments could be the effect of the induced excess carrier concentration in photoexcitation on the phonon distribution. Most first-principles studies of carrier transport assume an equilibrium occupation of phonons at a given lattice or physical temperature. This approximation is usually well-justified if the timescale of electron-phonon scattering is much longer than that of phonon-phonon scattering. In these cases phonons are driven out of equilibrium on the timescale of the electron-phonon interaction and one would then need a coupled electron-phonon BTE framework that includes the scattering of phonons by electrons in the phonon BTE. As we saw in Chapter 4, this framework is necessary to compute the mobility in semiconductors at high carrier concentrations as electrons and phonons "drag" themselves out of equilibrium. Without including drag in our calculation, we showed that the mobility reduced as the carrier concentration increased. This is a result of an increased phase space for electron-phonon scattering. When drag was included, the stronger electron-phonon interaction at high densities resulted in an increasing trend of the electron mobility with concentration.

5.1 Future work

Inclusion of other noise sources in HEMTs

In Chapter 2, we proposed one physical mechanism responsible for drain noise in HEMTs. Our work suggests measures to decrease the noise figure of HEMTs by carefully engineering the channel and barrier layers to optimize the conduction band offset to decrease the likelihood of thermionic emission out of the channel. However, our work assumed a peak electron temperature with a physical temperature dependence. This assumption may not be completely justified at high electric fields, as suggested in Ref. [107]. More experimental and modeling work needs to be done to accurately characterize the dependence of the peak electron temperature on physical temperature. Furthermore, there could be other mechanisms that contribute to the observed noise. Consider for example, impact ionization: a process where electrons subject to a high electric field gain sufficient energy to collide with ions and generate electron-hole pairs, exciting new charge carriers from the valence band of the material that then contribute to electrical conduction. Impact ionization is usually recognized as a kink in the DC current-voltage characteristics [40, 43] beyond the ohmic regime and at high bias. Effects of impact ionization on noise characteristics of HEMTs have been studied with Monte Carlo simulations [184, 185]. An improvement on our work could be an extension of our drain temperature model to include other potential contributors, such as impact ionization, to predict the drain noise figure.

Electron-two-phonon interactions

Our work considered one type of 2ph scattering: consecutive one-phonon events mediated by an intermediate state. This physical picture corresponds to the first derivative of the interatomic potential with respect to lattice displacements taken to second order in perturbation theory. We did not include 2ph events involving the simultaneous interaction of an electron with two phonons which corresponds to the second-order derivative of the interatomic potential. Further work is required to quantify the extent of the cancellation between these two 2ph processes.

Time-resolved evolution of distribution function

Our solution approach to the BTE assumes a steady-state distribution of electrons and phonons. An interesting next step is the development of tools to solve the time-dependent coupled BTEs for up to hundreds of ps. Some works have studied the time-dependent phonon BTE without assuming an equilibrium electron distribution function (that is, the collision term includes ph-ph and ph-e scattering) [186]. Tong and Bernardi developed a numerical scheme to solve the coupled electron-phonon BTEs for up to tens of picoseconds in a photoexcited graphene sample [187]. Application of such a scheme to study electron phonon dynamics in boron arsenide would aid in placing our simulation results in context of recent experimental findings. In general, a framework to investigate time-dependent electron and phonon transport for timescales long enough to observe equilibration would be useful to understand the dynamics of electrons and phonons under photoexcitation in materials.

Electron-electron interactions

In nondegenerate semiconductors, the effect of electron-electron scattering on transport coefficients is generally considered minimal compared to phonon and impurity scattering [188, 189]. However, at high carrier concentrations, the interaction of electrons with a collective electronic excitation—plasmons—is thought to be nontrivial [190, 191, 183]. Further, it has been established that for degenerate semiconductors there is a coupling between plasmons and phonons that challenges the assumption of independent (phonon and plasmon) excitations in the semiconductor [192, 193]. These effects are not considered in this thesis, but the inclusion of plasmonic effects within the first-principles BTE framework is an active area of research that will necessitate ongoing development in the years ahead.

BIBLIOGRAPHY

[1] Roberto Menozzi. Hot electron effects and degradation of GaAs and InP HEMTs for microwave and millimetre-wave applications. In: *Semiconductor science and technology* 13.10 (1998). `https://iopscience.iop.org/article/10.1088/0268-1242/13/10/001/meta`, p. 1053.

[2] Joel Schleeh et al. Characterization and modeling of cryogenic ultralow-noise InP HEMTs. In: *IEEE transactions on electron devices* 60.1 (2012). `https://ieeexplore.ieee.org/document/6365264`, pp. 206–212.

[3] Alexander Y Choi et al. Characterization of self-heating in cryogenic high electron mobility transistors using Schottky thermometry. In: *Journal of Applied Physics* 130.15 (2021). `https://pubs.aip.org/aip/jap/article/130/15/155107/1062506`.

[4] Anthony J Ardizzi et al. Self-heating of cryogenic high electron-mobility transistor amplifiers and the limits of microwave noise performance. In: *Journal of Applied Physics* 132.8 (2022). `https://pubs.aip.org/aip/jap/article/132/8/084501/2837443`.

[5] H. Heffner. The fundamental noise limit of linear amplifiers. In: *Proceedings of the IRE* 50.7 (1962). `https://ieeexplore.ieee.org/abstract/document/4066904/`, pp. 1604–1608.

[6] Marian W. Pospieszalski. Modeling of noise parameters of MESFETs and MODFETs and their frequency and temperature dependence. In: *IEEE transactions on microwave theory and techniques* 37.9 (1989). `https://ieeexplore.ieee.org/abstract/document/32217/`, pp. 1340–1350.

[7] Feliciano Giustino. Electron-phonon interactions from first principles. In: *Reviews of Modern Physics* 89.1 (2017). `https://journals.aps.org/rmp/abstract/10.1103/RevModPhys.89.015003`, p. 015003.

[8] Pierre Hohenberg and Walter Kohn. Inhomogeneous electron gas. In: *Physical review* 136.3B (1964). `https://journals.aps.org/pr/abstract/10.1103/PhysRev.136.B864`, B864.

[9] Walter Kohn and Lu Jeu Sham. Self-consistent equations including exchange and correlation effects. In: *Physical review* 140.4A (1965). `https://journals.aps.org/pr/abstract/10.1103/PhysRev.140.A1133`, A1133.

[10] Richard M Martin. *Electronic structure: basic theory and practical methods*. Cambridge university press, 2020.

[11] Samuel Poncé et al. First-principles calculations of charge carrier mobility and conductivity in bulk semiconductors and two-dimensional materials. In: *Reports on Progress in Physics* 83.3 (2020). https://iopscience.iop.org/article/10.1088/1361-6633/ab6a43/meta/, p. 036501.

[12] Stefano Baroni et al. Phonons and related crystal properties from density-functional perturbation theory. In: *Reviews of modern Physics* 73.2 (2001). https://journals.aps.org/rmp/abstract/10.1103/RevModPhys.73.515, p. 515.

[13] Ivo Souza, Nicola Marzari, and David Vanderbilt. Maximally localized Wannier functions for entangled energy bands. In: *Physical Review B* 65.3 (2001). https://journals.aps.org/prb/abstract/10.1103/PhysRevB.65.035109, p. 035109.

[14] Arash A Mostofi et al. wannier90: A tool for obtaining maximally-localised Wannier functions. In: *Computer physics communications* 178.9 (2008). https://www.sciencedirect.com/science/article/pii/S0010465507004936, pp. 685–699.

[15] Paul Drude. Zur elektronentheorie der metalle. In: *Annalen der Physik* 312.3 (1902), pp. 687–692.

[16] OD Restrepo, K Varga, and ST Pantelides. First-principles calculations of electron mobilities in silicon: Phonon and Coulomb scattering. In: *Applied Physics Letters* 94.21 (2009). https://pubs.aip.org/aip/apl/article/94/21/212103/118660/First-principles-calculations-of-electron.

[17] Kristen Kaasbjerg, Kristian S Thygesen, and Karsten W Jacobsen. Phonon-limited mobility in n-type single-layer MoS 2 from first principles. In: *Physical Review B* 85.11 (2012). https://journals.aps.org/prb/abstract/10.1103/PhysRevB.85.115317, p. 115317.

[18] Cheol-Hwan Park et al. Electron–phonon interactions and the intrinsic electrical resistivity of graphene. In: *Nano letters* 14.3 (2014). https://pubs.acs.org/doi/10.1021/nl402696q, pp. 1113–1119.

[19] Jin-Jian Zhou and Marco Bernardi. Ab initio electron mobility and polar phonon scattering in GaAs. In: *Physical Review B* 94.20 (2016). https://journals.aps.org/prb/abstract/10.1103/PhysRevB.94.201201, p. 201201.

[20] Marvin L Cohen and Steven G Louie. *Fundamentals of condensed matter physics*. Cambridge University Press, 2016.

[21] Marian W. Pospieszalski. Extremely low-noise amplification with cryogenic FETs and HFETs: 1970-2004. In: *IEEE Microwave Magazine* 6.3 (2005). https://ieeexplore.ieee.org/abstract/document/1511915, pp. 62–75.

[22] Joseph C. Bardin, Daniel H. Slichter, and David J. Reilly. Microwaves in quantum computing. In: *IEEE Journal of Microwaves* 1.1 (2021). https://ieeexplore.ieee.org/abstract/document/9318753, pp. 403–427.

[23] Philip Krantz et al. A quantum engineer's guide to superconducting qubits. In: *Applied Physics Reviews* 6.2 (2019). https://aip.scitation.org/doi/full/10.1063/1.5089550, p. 021318.

[24] Takatomo Enoki et al. 0.1-μm InAlAs/InGaAs HEMTS with an InP-recess-etch stopper grown by MOCVD. In: *Microwave and Optical Technology Letters* 11.3 (1996), pp. 135–139.

[25] Tamara Saranovac et al. Pt gate sink-in process details impact on InP HEMT DC and RF performance. In: *IEEE Transactions on Semiconductor Manufacturing* 30.4 (2017). https://ieeexplore.ieee.org/abstract/document/8027092, pp. 462–467.

[26] A Leuther et al. 35 nm metamorphic HEMT MMIC technology. In: *2008 20th International conference on indium phosphide and related materials*. https://ieeexplore.ieee.org/abstract/document/4702910. IEEE. 2008, pp. 1–4.

[27] Niklas Wadefalk et al. Cryogenic wide-band ultra-low-noise IF amplifiers operating at ultra-low DC power. In: *IEEE Transactions on Microwave Theory and Techniques* 51.6 (2003). https://ieeexplore.ieee.org/abstract/document/1201803, pp. 1705–1711.

[28] R Lai et al. Sub 50 nm InP HEMT with fT= 586 GHz and amplifier circuit gain at 390 GHz for sub-millimeter wave applications. In: *2010 22nd International Conference on Indium Phosphide and Related Materials (IPRM)*. https://ieeexplore.ieee.org/abstract/document/5516002. IEEE. 2010, pp. 1–3.

[29] Eunjung Cha et al. 0.3–14 and 16–28 GHz wide-bandwidth cryogenic MMIC low-noise amplifiers. In: *IEEE Transactions on Microwave Theory and Techniques* 66.11 (2018). https://ieeexplore.ieee.org/abstract/document/8500350, pp. 4860–4869.

[30] A Leuther et al. Metamorphic HEMT technology for low-noise applications. In: *2009 IEEE International Conference on Indium Phosphide & Related Materials*. https://ieeexplore.ieee.org/abstract/document/5012475. IEEE. 2009, pp. 188–191.

[31] R Lai et al. Sub 50 nm InP HEMT device with Fmax greater than 1 THz. In: *2007 IEEE International Electron Devices Meeting*. https://ieeexplore.ieee.org/abstract/document/4419013. IEEE. 2007, pp. 609–611.

[32] Liang Liu et al. InP-HEMT X-band low-noise amplifier with ultralow 0.6-mW power consumption. In: *IEEE electron device letters* 33.2 (2011). https://ieeexplore.ieee.org/abstract/document/6112173, pp. 209–211.

[33] Eunjung Cha et al. 0.3–14 and 16–28 GHz wide-bandwidth cryogenic MMIC low-noise amplifiers. In: *IEEE Transactions on Microwave Theory and Techniques* 66.11 (2018). https://ieeexplore.ieee.org/abstract/document/9108196, pp. 4860–4869.

[34] Eunjung Cha et al. InP HEMTs for sub-mW cryogenic low-noise amplifiers. In: *IEEE Electron Device Letters* 41.7 (2020). https://ieeexplore.ieee.org/abstract/document/9108196, pp. 1005–1008.

[35] R Dingle et al. Electron mobilities in modulation-doped semiconductor heterojunction superlattices. In: *Applied Physics Letters* 33.7 (1978). https://pubs.aip.org/aip/apl/article-abstract/33/7/665/1059745, pp. 665–667.

[36] Thomas Grave. Pseudomorphic HEMTs: Device Physics and Materials Layer Design. In: *Pseudomorphic HEMT Technology and Applications*. https://link.springer.com/chapter/10.1007/978-94-009-1630-2_2. Springer, 1996, pp. 23–69.

[37] Frank Schwierz. The frequency limits of field-effect transistors: MOSFET vs. HEMT. In: *2008 9th International Conference on Solid-State and Integrated-Circuit Technology*. https://ieeexplore.ieee.org/document/4734822. IEEE. 2008, pp. 1433–1436.

[38] *Fundamentals of HEMTs devices and technology.*

[39] EF Schubert. Delta doping of III–V compound semiconductors: Fundamentals and device applications. In: *Journal of Vacuum Science & Technology A: Vacuum, Surfaces, and Films* 8.3 (1990). https://avs.scitation.org/doi/pdf/10.1116/1.576617, pp. 2980–2996.

[40] Mark H Somerville, Alexander Ernst, and Jesús A del Alamo. A physical model for the kink effect in InAlAs/InGaAs HEMTs. In: *IEEE Transactions on Electron Devices* 47.5 (2000). https://ieeexplore.ieee.org/abstract/document/841222/, pp. 922–930.

[41] April S Brown et al. AlInAs-GaInAs HEMTs utilizing low-temperature AlInAs buffers grown by MBE. In: *IEEE electron device letters* 10.12 (1989). https://ieeexplore.ieee.org/abstract/document/43141/, pp. 565–567.

[42] W Kruppa and J Brad Boos. Examination of the kink effect in InAlAs/InGaAs/InP HEMTs using sinusoidal and transient excitation. In: *IEEE Transactions on Electron Devices* 42.10 (1995). https://ieeexplore.ieee.org/abstract/document/464427/, pp. 1717–1723.

[43] Guo-Gang Zhou, A Fischer-Colbrie, and JS Harris. IV kink in InAlAs/InGaAs MODFETs due to weak impact ionization process in the InGaAs channel. In: *Proceedings of 1994 IEEE 6th International Conference on Indium Phosphide and Related Materials (IPRM)*. `https://ieeexplore.ieee.org/abstract/document/328263/`. IEEE. 1994, pp. 435–438.

[44] Xiaobing Mei et al. First demonstration of amplification at 1 THz using 25-nm InP high electron mobility transistor process. In: *IEEE Electron Device Letters* 36.4 (2015). `https://ieeexplore.ieee.org/abstract/document/7047678`, pp. 327–329.

[45] Dae-Hyun Kim, Berinder Brar, and Jesús A del Alamo. f T= 688 GHz and f max= 800 GHz in L g= 40 nm In 0.7 Ga 0.3 As MHEMTs with g m_max> 2.7 mS/μm. In: *2011 International Electron Devices Meeting*. `https://ieeexplore.ieee.org/abstract/document/6131548/`. IEEE. 2011, pp. 13–6.

[46] Keysight. Fundamentals of RF and microwave noise figure measurements. In: (2022).

[47] V Mitin, L Reggiani, and L Varani. Generation-recombination noise in semiconductors. In: *Noise and fluctuations control in electronic devices* (2002). `http://www-ee.eng.buffalo.edu/faculty/mitin/Papers/VMitin_doc_1-20-10.pdf`, pp. 11–30.

[48] Sh Kogan. Electronic noise and fluctuations in solids. In: *Electronic Noise and Fluctuations in Solids* (2008).

[49] Harry Nyquist. Thermal agitation of electric charge in conductors. In: *Physical review* 32.1 (1928). `https://journals.aps.org/pr/abstract/10.1103/PhysRev.32.110`, p. 110.

[50] John Bertrand Johnson. Thermal agitation of electricity in conductors. In: *Physical review* 32.1 (1928). `https://journals.aps.org/pr/abstract/10.1103/PhysRev.32.97`, p. 97.

[51] Charles Kittel. *Elementary statistical physics*. Courier Corporation, 2004.

[52] Bekari Gabritchidze. Investigation of drain noise in high electron mobility transistors through on-wafer characterization and modelling. PhD thesis. University of Crete, 2022.

[53] Hermann Statz, Hermann A. Haus, and Robert A. Pucel. Noise characteristics of gallium arsenide field-effect transistors. In: *IEEE Transactions on Electron Devices* 21.9 (1974). `https://ieeexplore.ieee.org/abstract/document/1477781`, pp. 549–562.

[54] W. Shockley, John A. Copeland, and R.P. James. The impedance field method of noise calculation in active semiconductor devices. In: *Quantum Theory of Atoms, Molecules, and the Solid State, A tribute to John C. Slater* (1966), p. 537.

[55] A Van der Ziel. Thermal noise in double-injection space-charge-limited solid-state diodes. In: *Electronics Letters* 2.6 (1970), pp. 45–46.

[56] A Van der Ziel. Thermal noise in the hot electron regime in FET's. In: *IEEE Transactions on Electron Devices* 18.10 (1971). `https://ieeexplore.ieee.org/abstract/document/1476637`, pp. 977–977.

[57] Marian W Pospieszalski. On the limits of noise performance of field effect transistors. In: *2017 IEEE MTT-S International Microwave Symposium (IMS)*. `https://ieeexplore.ieee.org/abstract/document/8059045`. IEEE. 2017, pp. 1953–1956.

[58] Sayan Das and Joseph C Bardin. Characterization of shot noise suppression in nanometer MOSFETs. In: *2021 IEEE MTT-S International Microwave Symposium (IMS)*. `https://ieeexplore.ieee.org/document/9574931`. IEEE. 2021, pp. 892–895.

[59] S Munoz et al. Drain temperature dependence on ambient temperature for a cryogenic low noise C-band amplifier. In: *1997 27th European Microwave Conference*. Vol. 1. `https://ieeexplore.ieee.org/abstract/document/4138821`. IEEE. 1997, pp. 114–118.

[60] Sander Weinreb and Jun Shi. Low Noise Amplifier With 7-K Noise at 1.4 GHz and 25° C. In: *IEEE Transactions on Microwave Theory and Techniques* (2021). `https://ieeexplore.ieee.org/abstract/document/9374769`.

[61] Marian W Pospieszalski. On the dependence of FET noise model parameters on ambient temperature. In: *2017 IEEE Radio and Wireless Symposium (RWS)*. `https://ieeexplore.ieee.org/abstract/document/7885975`. IEEE. 2017, pp. 159–161.

[62] Jagdeep Shah. Hot electrons and phonons under high intensity photoexcitation of semiconductors. In: *Solid-State Electronics* 21.1 (1978). `https://www.sciencedirect.com/science/article/pii/0038110178901132`, pp. 43–50.

[63] WH Knox et al. Femtosecond excitation of nonthermal carrier populations in GaAs quantum wells. In: *Physical review letters* 56.11 (1986). `https://journals.aps.org/prl/abstract/10.1103/PhysRevLett.56.1191`, p. 1191.

[64] Bekari Gabritchidze et al. Experimental characterization of temperature-dependent microwave noise of discrete HEMTs: Drain noise and real-space transfer. In: *2022 IEEE/MTT-S International Microwave Symposium-*

IMS 2022. https://ieeexplore.ieee.org/abstract/document/9865505. IEEE. 2022, pp. 615–618.

[65] RA Höpfel et al. Hot carrier drift velocities in GaAs/AlGaAs multiple quantum well structures. In: *Physica B+ C* 134.1-3 (1985). https://www.sciencedirect.com/science/article/pii/0378436385903961, pp. 509–513.

[66] Jagdeep Shah et al. Hot electrons in modulation-doped GaAs-AlGaAs heterostructures. In: *Applied physics letters* 44.3 (1984). https://aip.scitation.org/doi/abs/10.1063/1.94739, pp. 322–324.

[67] Marion Asche et al. *Hot-electron transport in semiconductors*. Vol. 58. Springer Science & Business Media, 2006.

[68] Jagdeep Shah et al. Energy-loss rates for hot electrons and holes in GaAs quantum wells. In: *Physical review letters* 54.18 (1985). https://journals.aps.org/prl/abstract/10.1103/PhysRevLett.54.2045, p. 2045.

[69] Kathleen Kash et al. Picosecond luminescence measurements of hot carrier relaxation in III–V semiconductors using sum frequency generation. In: *Physica B+ C* 134.1-3 (1985). https://www.sciencedirect.com/science/article/pii/0378436385903420, pp. 189–198.

[70] SA Lyon. Spectroscopy of hot carriers in semiconductors. In: *Journal of luminescence* 35.3 (1986). https://www.sciencedirect.com/science/article/pii/0022231386900669, pp. 121–154.

[71] Ralph A Höpfel, Jagdeep Shah, and Arthur C Gossard. Nonequilibrium electron-hole plasma in GaAs quantum wells. In: *Physical review letters* 56.7 (1986). https://journals.aps.org/prl/abstract/10.1103/PhysRevLett.56.765, p. 765.

[72] Jagdeep Shah. Investigation of hot carrier relaxation with picosecond laser pulses. In: *Le Journal de Physique Colloques* 42.C7 (1981). https://jphyscol.journaldephysique.org/articles/jphyscol/abs/1981/07/jphyscol198142C755/jphyscol198142C755.html, pp. C7–445.

[73] V Aninkevičius et al. Comparative analysis of microwave noise in GaAs and AlGaAs/GaAs channels. In: *Solid-state electronics* 36.9 (1993). https://www.sciencedirect.com/science/article/pii/003811019390174O, pp. 1339–1343.

[74] A Matulionis et al. QW-shape-dependent hot-electron velocity fluctuations in InGaAs-based heterostructures. In: *physica status solidi (b)* 204.1 (1997), pp. 453–455.

[75] RA Höpfel and G Weimann. Electron heating and free-carrier absorption in GaAs/AlGaAs single heterostructures. In: *Applied physics letters* 46.3 (1985). https://aip.scitation.org/doi/abs/10.1063/1.95662, pp. 291–293.

[76] MG Shorthose, JF Ryan, and A Moseley. Phonon-assisted tunnelling of photoexcited carriers from InGaAs quantum wells in applied electric fields. In: *Solid-state electronics* 32.12 (1989). https://www.sciencedirect.com/science/article/pii/0038110189902554, pp. 1449–1453.

[77] Jagdeep Shah. Hot carriers in quasi-2-D polar semiconductors. In: *IEEE journal of quantum electronics* 22.9 (1986). https://ieeexplore.ieee.org/abstract/document/1073164, pp. 1728–1743.

[78] RA Höpfel et al. Picosecond time-of-flight measurements of minority electrons in GaAs/AlGaAs quantum well structures. In: *Applied physics letters* 48.2 (1986). https://aip.scitation.org/doi/abs/10.1063/1.96979, pp. 148–150.

[79] BK Ridley. Hot electrons in low-dimensional structures. In: *Reports on Progress in Physics* 54.2 (1991). https://iopscience.iop.org/article/10.1088/0034-4885/54/2/001/meta, p. 169.

[80] K Hess et al. Negative differential resistance through real-space electron transfer. In: *Applied Physics Letters* 35.6 (1979). https://aip.scitation.org/doi/abs/10.1063/1.91172, pp. 469–471.

[81] Serge Luryi et al. Charge injection transistor based on real-space hot-electron transfer. In: *IEEE Transactions on Electron Devices* 31.6 (1984). https://ieeexplore.ieee.org/abstract/document/1483901, pp. 832–839.

[82] A Kastalsky et al. A field-effect transistor with a negative differential resistance. In: *IEEE electron device letters* 5.2 (1984). https://ieeexplore.ieee.org/abstract/document/1484207, pp. 57–60.

[83] YK Chen et al. Observation of high-frequency high-field instability in GaAs/InGaAs/AlGaAs DH-MODFETs at K band. In: *IEEE electron device letters* 9.1 (1988). https://ieeexplore.ieee.org/abstract/document/20394, pp. 1–3.

[84] Joy Laskar et al. Experimental and theoretical investigation of the DC and high-frequency characteristics of the negative differential resistance in pseudomorphic AlGaAs/InGaAs/GaAs MODFETs. In: *IEEE transactions on electron devices* 39.2 (1992). https://ieeexplore.ieee.org/abstract/document/121681, pp. 257–263.

[85] PJ Price. Intervalley noise. In: *Journal of Applied Physics* 31.6 (1960). https://aip.scitation.org/doi/abs/10.1063/1.1735782, pp. 949–953.

[86] W Shockley, JA Copeland, and RP James. Quantum Theory of Atoms. In: *Molecules and the Solid State (New York: Academic)* (1966).

[87] Milton Feng et al. Real space transfer noise of GaAs p-HEMTs. In: *Compound Semiconductors 1997. Proceedings of the IEEE Twenty-Fourth International Symposium on Compound Semiconductors*. https://ieeexplore.ieee.org/abstract/document/711707. IEEE. 1997, pp. 463–466.

[88] A Van Die and JI Dijkhuis. Thermally activated real-space-transfer noise in pseudomorphic high-electron-mobility transistors. In: *Journal of applied physics* 74.2 (1993). https://aip.scitation.org/doi/abs/10.1063/1.354914, pp. 1143–1150.

[89] Javier Mateos et al. Influence of real-space transfer on transit time and noise in HEMTs. In: *ESSDERC'96: Proceedings of the 26th European Solid State Device Research Conference*. https://ieeexplore.ieee.org/abstract/document/5436031. IEEE. 1996, pp. 745–748.

[90] Javier Mateos et al. Influence of Al mole fraction on the noise performance of GaAs/Al/sub x/Ga/sub 1-x/As HEMTs. In: *IEEE Transactions on Electron Devices* 45.9 (1998). https://ieeexplore.ieee.org/abstract/document/711380, pp. 2081–2083.

[91] Frank Schwierz and Juin J Liou. *Modern microwave transistors: theory, design, and performance*. Wiley-interscience, 2003.

[92] Javier Mateos et al. Effect of the T-gate on the performance of recessed HEMTs. A Monte Carlo analysis. In: *Semiconductor science and technology* 14.9 (1999). https://iopscience.iop.org/article/10.1088/0268-1242/14/9/320/meta, p. 864.

[93] Joel Schleeh. *Cryogenic ultra-low noise InP high electron mobility transistors*. https://publications.lib.chalmers.se/records/fulltext/186929/186929.pdf. Chalmers University of Technology, 2013.

[94] KM Van Vliet et al. Noise in single injection diodes. I. A survey of methods. In: *Journal of Applied Physics* 46.4 (1975). https://ieeexplore.ieee.org/abstract/document/9108196, pp. 1804–1813.

[95] ZS Gribnikov, Karl Hess, and GA Kosinovsky. Nonlocal and nonlinear transport in semiconductors: Real-space transfer effects. In: *Journal of applied physics* 77.4 (1995). https://aip.scitation.org/doi/abs/10.1063/1.358947, pp. 1337–1373.

[96] M Keever et al. Measurements of hot-electron conduction and real-space transfer in GaAs-Al x Ga1- x As heterojunction layers. In: *Applied Physics Letters* 38.1 (1981). https://aip.scitation.org/doi/abs/10.1063/1.92117, pp. 36–38.

[97] TH Glisson et al. Monte Carlo simulation of real-space electron transfer in GaAs-AlGaAs heterostructures. In: *Journal of Applied Physics* 51.10 (1980). `https://aip.scitation.org/doi/abs/10.1063/1.327500`, pp. 5445–5449.

[98] Yen-Wei Chen et al. Enhancement-mode In 0.52 Al 0.48 As/In 0.6 Ga 0.4 As tunneling real space transfer high electron mobility transistor. In: *Journal of Vacuum Science & Technology B: Microelectronics and Nanometer Structures Processing, Measurement, and Phenomena* 22.3 (2004). `https://avs.scitation.org/doi/abs/10.1116/1.1715090`, pp. 974–976.

[99] M Keever, K Hess, and M Ludowise. Fast switching and storage in GaAs—Al x Ga 1-x As heterojunction layers. In: *IEEE Electron Device Letters* 3.10 (1982). `https://ieeexplore.ieee.org/abstract/document/1482680`, pp. 297–300.

[100] Eunjung Cha. *InP High Electron Mobility Transistors for Cryogenic Low-Noiseand Low-Power Amplifiers*. Chalmers University of Technology, 2020.

[101] DH Park and KF Brennan. Monte Carlo simulation of 0.35-mu m gate-length GaAs and InGaAs HEMTs. In: *IEEE transactions on electron devices* 37.3 (1990). `https://ieeexplore.ieee.org/abstract/document/47765`, pp. 618–628.

[102] Helena Rodilla et al. Cryogenic performance of low-noise InP HEMTs: a Monte Carlo study. In: *IEEE transactions on electron devices* 60.5 (2013). `https://ieeexplore.ieee.org/abstract/document/6497570`, pp. 1625–1631.

[103] Simon M Sze and Kwok K Ng. *Physics of semiconductor devices*. John wiley & sons, 2007.

[104] *Sentaurus TCAD manuals*. URL: `http://www.synopsys.com/`.

[105] Felix Heinz et al. Noise Performance of Sub-100-nm Metamorphic HEMT Technologies. In: *2020 IEEE/MTT-S International Microwave Symposium (IMS)*. `https://ieeexplore.ieee.org/abstract/document/9223783`. IEEE. 2020, pp. 293–296.

[106] MR Murti et al. Temperature-dependent small-signal and noise parameter measurements and modeling on InP HEMTs. In: *IEEE Transactions on Microwave Theory and Techniques* 48.12 (2000). `https://ieeexplore.ieee.org/abstract/document/899016`, pp. 2579–2587.

[107] Massimo V Fischetti. Monte Carlo simulation of transport in technologically significant semiconductors of the diamond and zinc-blende structures. I. Homogeneous transport. In: *IEEE transactions on elec-*

tron devices 38.3 (1991). https://ieeexplore.ieee.org/abstract/document/75176/, pp. 634–649.

[108] Charles Kittel and Herbert Kroemer. Thermal physics. In: 2nd. 1998, p. 183.

[109] Robert A Pucel, Hermann A Haus, and Hermann Statz. Signal and noise properties of gallium arsenide microwave field-effect transistors. In: *Advances in electronics and electron physics*. Vol. 38. https://www.sciencedirect.com/science/article/pii/S0065253908612056. Elsevier, 1975, pp. 195–265.

[110] J Frey. Effects of intervalley scattering on noise in GaAs and InP field-effect transistors. In: *IEEE Transactions on Electron Devices* 23.12 (1976). https://ieeexplore.ieee.org/stamp/stamp.jsp?arnumber=1478666, pp. 1298–1303.

[111] Werner Baechtold. Noise behavior of GaAs field-effect transistors with short gate lengths. In: *IEEE Transactions on Electron Devices* 19.5 (1972). https://ieeexplore.ieee.org/abstract/document/1476944, pp. 674–680.

[112] EA Hendriks and RJJ Zijlstra. Diffusion and inter-valley noise in (100) n-channel Si-MOSFETs from T= 4.2 to 295 K. In: *Solid-state electronics* 31.2 (1988). https://www.sciencedirect.com/science/article/pii/0038110188901268, pp. 171–180.

[113] KY Cheng et al. Measurement of the Γ-L separation in Ga0. 47In0. 53As by ultraviolet photoemission. In: *Applied Physics Letters* 40.5 (1982). https://aip.scitation.org/doi/pdf/10.1063/1.93126, pp. 423–425.

[114] T González et al. Noise suppression due to long-range Coulomb interaction: crossover between diffusive and ballistic transport regimes. In: *Semiconductor science and technology* 12.8 (1997). https://iopscience.iop.org/article/10.1088/0268-1242/12/8/001/meta, p. 1053.

[115] Sandeep R Bahl, WJ Azzam, and JA del Alamo. Strained-insulator in/sub x/al/sub 1-x/as/n/sup+/-in/sub 0.53/ga/sub 0.47/as heterostructure field-effect transistors. In: *IEEE transactions on electron devices* 38.9 (1991). https://ieeexplore.ieee.org/abstract/document/83719, pp. 1986–1992.

[116] Lucas Lindsay, DA Broido, and TL Reinecke. First-principles determination of ultrahigh thermal conductivity of boron arsenide: A competitor for diamond? In: *Physical review letters* 111.2 (2013). https://journals.aps.org/prl/abstract/10.1103/PhysRevLett.111.025901, p. 025901.

[117] Joon Sang Kang et al. Experimental observation of high thermal conductivity in boron arsenide. In: *Science* 361.6402 (2018). `https://www.science.org/doi/full/10.1126/science.aat5522`, pp. 575–578.

[118] Sheng Li et al. High thermal conductivity in cubic boron arsenide crystals. In: *Science* 361.6402 (2018). `https://www.science.org/doi/full/10.1126/science.aat8982`, pp. 579–581.

[119] Fei Tian et al. Unusual high thermal conductivity in boron arsenide bulk crystals. In: *Science* 361.6402 (2018). `https://www.science.org/doi/full/10.1126/science.aat7932`, pp. 582–585.

[120] Te-Huan Liu et al. Simultaneously high electron and hole mobilities in cubic boron-V compounds: BP, BAs, and BSb. In: *Physical Review B* 98.8 (2018). `https://journals.aps.org/prb/abstract/10.1103/PhysRevB.98.081203`, p. 081203.

[121] Kyle Bushick et al. Boron arsenide heterostructures: lattice-matched heterointerfaces and strain effects on band alignments and mobility. In: *npj Computational Materials* 6.1 (2020). `https://www.nature.com/articles/s41524-019-0270-4`, p. 3.

[122] Joon Sang Kang et al. Integration of boron arsenide cooling substrates into gallium nitride devices. In: *Nature Electronics* 4.6 (2021). `https://www.nature.com/articles/s41928-021-00595-9`, pp. 416–423.

[123] Bing Lv et al. Experimental study of the proposed super-thermal-conductor: BAs. In: *Applied Physics Letters* 106.7 (2015). `https://aip.scitation.org/doi/10.1063/1.4913441`, p. 074105.

[124] Tianli Feng, Lucas Lindsay, and Xiulin Ruan. Four-phonon scattering significantly reduces intrinsic thermal conductivity of solids. In: *Physical Review B* 96.16 (2017). `https://journals.aps.org/prb/abstract/10.1103/PhysRevB.96.161201`, p. 161201.

[125] Jaehyun Kim et al. Thermal and thermoelectric transport measurements of an individual boron arsenide microstructure. In: *Applied Physics Letters* 108.20 (2016). `https://aip.scitation.org/doi/10.1063/1.4950970`, p. 201905.

[126] Jungwoo Shin et al. High ambipolar mobility in cubic boron arsenide. In: *Science* 377.6604 (2022). `https://www.science.org/doi/full/10.1126/science.abn4290`, pp. 437–440.

[127] Shuai Yue et al. High ambipolar mobility in cubic boron arsenide revealed by transient reflectivity microscopy. In: *Science* 377.6604 (2022). `https://www.science.org/doi/full/10.1126/science.abn4727`, pp. 433–436.

[128] Marco Bernardi et al. Ab initio study of hot carriers in the first picosecond after sunlight absorption in silicon. In: *Physical review letters* 112.25 (2014). `https://journals.aps.org/prl/abstract/10.1103/PhysRevLett.112.257402`, p. 257402.

[129] A Sher and KK Thornber. RESONANT ELECTRON-PHONON SCATTERING IN POLAR SEMICONDUCTORS. In: *Applied Physics Letters* 11.1 (1967). `https://aip.scitation.org/doi/abs/10.1063/1.1754948`, pp. 3–5.

[130] KL Ngai and EJ Johnson. Two-phonon deformation potential in InSb. In: *Physical Review Letters* 29.24 (1972). `https://journals.aps.org/prl/abstract/10.1103/PhysRevLett.29.1607`, p. 1607.

[131] Gerald P Alldredge and FJ Blatt. On the role of two-phonon processes in the energy relaxation of a heated-electron distribution. In: *Annals of Physics* 45.2 (1967). `https://www.sciencedirect.com/science/article/pii/0003491667901236`, pp. 191–231.

[132] Nien-En Lee et al. Ab initio electron-two-phonon scattering in GaAs from next-to-leading order perturbation theory. In: *Nature communications* 11.1 (2020). `https://www.nature.com/articles/s41467-020-15339-0`, p. 1607.

[133] Peishi S Cheng et al. High-field transport and hot-electron noise in GaAs from first-principles calculations: Role of two-phonon scattering. In: *Physical Review B* 106.24 (2022). `https://journals.aps.org/prb/abstract/10.1103/PhysRevB.106.245201`, p. 245201.

[134] Benjamin Hatanpää et al. Two-phonon scattering in nonpolar semiconductors: A first-principles study of warm electron transport in Si. In: *Physical Review B* 107.4 (2023). `https://journals.aps.org/prb/abstract/10.1103/PhysRevB.107.L041110`, p. L041110.

[135] Joon Sang Kang et al. Basic physical properties of cubic boron arsenide. In: *Applied Physics Letters* 115.12 (2019). `https://aip.scitation.org/doi/full/10.1063/1.5116025`, p. 122103.

[136] Gerald D. Mahan. *Condensed matter in a nutshell.* Princeton University Press, 2011.

[137] Peishi Cheng. *Charge and heat transport in non-metallic crystals using first-principles Boltzmann transport theory.* California Institute of Technology, 2022.

[138] P. Lawaetz. Long-Wavelength Phonon Scattering in Nonpolar Semiconductors. In: *Phys. Rev.* 183 (3 July 1969). `https://link.aps.org/doi/10.1103/PhysRev.183.730`, pp. 730–739. DOI: `10.1103/PhysRev.183.730`.

[139] P. Vogl. Microscopic theory of electron-phonon interaction in insulators or semiconductors. In: *Phys. Rev. B* 13 (2 Jan. 1976). `https://link.aps.org/doi/10.1103/PhysRevB.13.694`, pp. 694–704. DOI: `10.1103/PhysRevB.13.694`.

[140] Jinsoo Park et al. Long-range quadrupole electron-phonon interaction from first principles. In: *Physical Review B* 102.12 (2020). `https://journals.aps.org/prb/abstract/10.1103/PhysRevB.102.125203`, p. 125203.

[141] Miquel Royo and Massimiliano Stengel. First-principles theory of spatial dispersion: Dynamical quadrupoles and flexoelectricity. In: *Physical Review X* 9.2 (2019). `https://journals.aps.org/prx/abstract/10.1103/PhysRevX.9.021050`, p. 021050.

[142] Miquel Royo, Konstanze R Hahn, and Massimiliano Stengel. Using high multipolar orders to reconstruct the sound velocity in piezoelectrics from lattice dynamics. In: *Physical Review Letters* 125.21 (2020). `https://journals.aps.org/prl/abstract/10.1103/PhysRevLett.125.217602`, p. 217602.

[143] Xavier Gonze and Changyol Lee. Dynamical matrices, Born effective charges, dielectric permittivity tensors, and interatomic force constants from density-functional perturbation theory. In: *Physical Review B* 55.16 (1997). `https://journals.aps.org/prb/abstract/10.1103/PhysRevB.55.10355`, p. 10355.

[144] Alexander Y Choi et al. Electronic noise of warm electrons in semiconductors from first principles. In: *Physical Review Materials* 5.4 (2021). `https://journals.aps.org/prmaterials/abstract/10.1103/PhysRevMaterials.5.044603`, p. 044603.

[145] Samuel Poncé et al. First-principles predictions of hall and drift mobilities in semiconductors. In: *Physical Review Research* 3.4 (2021). `https://journals.aps.org/prresearch/abstract/10.1103/PhysRevResearch.3.043022`, p. 043022.

[146] Marco Bernardi. First-principles dynamics of electrons and phonons. In: *The European Physical Journal B* 89 (2016). `https://link.springer.com/article/10.1140/epjb/e2016-70399-4`, pp. 1–15.

[147] Paolo Giannozzi et al. QUANTUM ESPRESSO: a modular and open-source software project for quantum simulations of materials. In: *Journal of physics: Condensed matter* 21.39 (2009), p. 395502.

[148] Jin-Jian Zhou et al. Perturbo: A software package for ab initio electron–phonon interactions, charge transport and ultrafast dynamics. In: *Computer Physics Communications* 264 (2021). `https://www.sciencedirect.com/science/article/pii/S0010465521000837`, p. 107970.

[149] Xavier Gonze et al. Recent developments in the ABINIT software package. In: *Computer Physics Communications* 205 (2016), pp. 106–131.

[150] Samuel Poncé et al. EPW: Electron–phonon coupling, transport and superconducting properties using maximally localized Wannier functions. In: *Computer Physics Communications* 209 (2016). https://www.sciencedirect.com/science/article/pii/S0010465516302260, pp. 116–133.

[151] Kyle Bushick et al. Band structure and carrier effective masses of boron arsenide: Effects of quasiparticle and spin-orbit coupling corrections. In: *Applied Physics Letters* 114.2 (2019). https://aip.scitation.org/doi/10.1063/1.5062845, p. 022101.

[152] Samuel Poncé, Elena R Margine, and Feliciano Giustino. Towards predictive many-body calculations of phonon-limited carrier mobilities in semiconductors. In: *Physical Review B* 97.12 (2018). https://journals.aps.org/prb/abstract/10.1103/PhysRevB.97.121201, p. 121201.

[153] John Buckeridge and David O Scanlon. Electronic band structure and optical properties of boron arsenide. In: *Physical Review Materials* 3.5 (2019). https://journals.aps.org/prmaterials/pdf/10.1103/PhysRevMaterials.3.051601, p. 051601.

[154] John L Lyons et al. Impurity-derived p-type conductivity in cubic boron arsenide. In: *Applied Physics Letters* 113.25 (2018). https://aip.scitation.org/doi/10.1063/1.5058134, p. 251902.

[155] Ebrahim Najafi et al. Super-diffusion of excited carriers in semiconductors. In: *Nature communications* 8.1 (2017). https://www.nature.com/articles/ncomms15177?origin=ppub, pp. 1–7.

[156] Brian A Ruzicka et al. Hot carrier diffusion in graphene. In: *Physical Review B* 82.19 (2010). https://journals.aps.org/prb/abstract/10.1103/PhysRevB.82.195414, p. 195414.

[157] Usama Choudhry et al. Persistent hot carrier diffusion in boron arsenide single crystals imaged by ultrafast electron microscopy. In: *Matter* (2022). https://www.sciencedirect.com/science/article/pii/S2590238522005811.

[158] T Holstein. Theory of ultrasonic absorption in metals: the collision-drag effect. In: *Physical review* 113.2 (1959). https://journals.aps.org/pr/abstract/10.1103/PhysRev.113.479, p. 479.

[159] P. Kocevar. Multiphonon Scattering. In: *Physics of Nonlinear Transport in Semiconductors*. Ed. by David K. Ferry, J. R. Barker, and C. Jacoboni. Boston, MA: Springer US, 1980, pp. 167–174. ISBN: 978-1-4684-3638-9. DOI: 10.1007/978-1-4684-3638-9_7. URL: https://doi.org/10.1007/978-1-4684-3638-9_7.

[160] BA Weinstein and Manuel Cardona. Resonant first-and second-order Raman scattering in GaP. In: *Phys. Rev. B* 8.6 (1973). https://journals.aps.org/prb/abstract/10.1103/PhysRevB.8.2795, p. 2795.

[161] KL Ngai. Carrier-Two Phonon Interaction in Semiconductors. In: *Proceedings of the Twelfth International Conference on the Physics of Semiconductors: July 15–19, 1974 Stuttgart.* https://link.springer.com/chapter/10.1007/978-3-322-94774-1_83. Springer. 1974, pp. 489–498.

[162] G Fasol et al. Continuous-wave spectroscopy of femtosecond carrier scattering in GaAs. In: *Physical Review B* 41.3 (1990). https://journals.aps.org/prb/abstract/10.1103/PhysRevB.41.1461, p. 1461.

[163] R Peierls. Zur Theorie der elektrischen und thermischen Leitfähigkeit von Metallen. In: *Annalen der Physik* 396.2 (1930). https://onlinelibrary.wiley.com/doi/10.1002/andp.19303960202, pp. 121–148.

[164] Yu G Gurevich and OL Mashkevich. The electron-phonon drag and transport phenomena in semiconductors. In: *Physics Reports* 181.6 (1989), pp. 327–394.

[165] HPR Frederikse. Thermoelectric power of germanium below room temperature. In: *Physical Review* 92.2 (1953). https://journals.aps.org/pr/abstract/10.1103/PhysRev.92.248, p. 248.

[166] TH Geballe and GW Hull. Seebeck effect in germanium. In: *Physical Review* 94.5 (1954). https://journals.aps.org/pr/abstract/10.1103/PhysRev.94.1134, p. 1134.

[167] TH Geballe and GW Hull. Seebeck effect in silicon. In: *Physical Review* 98.4 (1955). https://journals.aps.org/pr/abstract/10.1103/PhysRev.98.940, p. 940.

[168] AR Hutson. Piezoelectric scattering and phonon drag in ZnO and CdS. In: *Journal of Applied Physics* 32.10 (1961). https://pubs.aip.org/aip/jap/article/32/10/2287/376949/Piezoelectric-Scattering-and-Phonon-Drag-in-ZnO, pp. 2287–2292.

[169] GD Mahan, L Lindsay, and DA Broido. The Seebeck coefficient and phonon drag in silicon. In: *Journal of Applied Physics* 116.24 (2014). https://pubs.aip.org/aip/jap/article/116/24/245102/152054.

[170] Jiawei Zhou et al. Ab initio optimization of phonon drag effect for lower-temperature thermoelectric energy conversion. In: *Proceedings of the National Academy of Sciences* 112.48 (2015). https://www.pnas.org/doi/abs/10.1073/pnas.1512328112, pp. 14777–14782.

[171] Mattia Fiorentini and Nicola Bonini. Thermoelectric coefficients of n-doped silicon from first principles via the solution of the Boltzmann transport equation. In: *Physical Review B* 94.8 (2016). https://journals.aps.org/prb/abstract/10.1103/PhysRevB.94.085204, p. 085204.

[172] Nakib H Protik et al. The elphbolt ab initio solver for the coupled electron-phonon Boltzmann transport equations. In: *npj Computational Materials* 8.1 (2022). https://www.nature.com/articles/s41524-022-00710-0, p. 28.

[173] Nakib H Protik and David A Broido. Coupled transport of phonons and carriers in semiconductors: A case study of n-doped GaAs. In: *Physical Review B* 101.7 (2020). https://journals.aps.org/prb/abstract/10.1103/PhysRevB.101.075202, p. 075202.

[174] Chunhua Li et al. Colossal phonon drag enhanced thermopower in lightly doped diamond. In: *Materials Today Physics* 27 (2022). https://www.sciencedirect.com/science/article/pii/S2542529322001389, p. 100740.

[175] Yujie Quan, Yubi Chen, and Bolin Liao. Significant phonon drag effect in wide band gap GaN and AlN. In: *Physical Review B* 107.24 (2023). https://journals.aps.org/prb/abstract/10.1103/PhysRevB.107.245202, p. 245202.

[176] Chunhua Li et al. High-frequency phonons drive large phonon-drag thermopower in semiconductors at high carrier density. In: *Physical Review B* 107.8 (2023). https://journals.aps.org/prb/abstract/10.1103/PhysRevB.107.L081202, p. L081202.

[177] Jiawei Zhou, Bolin Liao, and Gang Chen. First-principles calculations of thermal, electrical, and thermoelectric transport properties of semiconductors. In: *Semiconductor Science and Technology* 31.4 (2016). https://iopscience.iop.org/article/10.1088/0268-1242/31/4/043001/meta, p. 043001.

[178] Navaneetha K Ravichandran and David Broido. Phonon-phonon interactions in strongly bonded solids: selection rules and higher-order processes. In: *Physical Review X* 10.2 (2020). https://journals.aps.org/prx/abstract/10.1103/PhysRevX.10.021063, p. 021063.

[179] Wu Li. Electrical transport limited by electron-phonon coupling from Boltzmann transport equation: An ab initio study of Si, Al, and MoS 2. In: *Physical Review B* 92.7 (2015). https://journals.aps.org/prb/abstract/10.1103/PhysRevB.92.075405, p. 075405.

[180] Wu Li et al. ShengBTE: A solver of the Boltzmann transport equation for phonons. In: *Computer Physics Communications* 185.6 (2014). https://www.sciencedirect.com/science/article/pii/S0010465514000484, pp. 1747–1758.

[181] Nakib H Protik and Boris Kozinsky. Electron-phonon drag enhancement of transport properties from a fully coupled ab initio Boltzmann formalism. In: *Physical Review B* 102.24 (2020). `https://journals.aps.org/prb/abstract/10.1103/PhysRevB.102.245202`, p. 245202.

[182] Tian Fang et al. High-field transport in two-dimensional graphene. In: *Physical Review B* 84.12 (2011). `https://journals.aps.org/prb/abstract/10.1103/PhysRevB.84.125450`, p. 125450.

[183] Fabio Caruso and Feliciano Giustino. Theory of electron-plasmon coupling in semiconductors. In: *Physical Review B* 94.11 (2016). `https://journals.aps.org/prb/pdf/10.1103/PhysRevB.94.115208`, p. 115208.

[184] J Mateos et al. Monte Carlo modelling of noise in advanced III–V HEMTs. In: *Journal of Computational Electronics* 14.1 (2015). `https://link.springer.com/article/10.1007/s10825-014-0653-1`, pp. 72–86.

[185] Mark Isler. Investigation and modeling of impact ionization in HEMTs for DC and RF operating conditions. In: *Solid-State Electronics* 46.10 (2002). `https://www.sciencedirect.com/science/article/pii/S0038110102001107`, pp. 1587–1593.

[186] Sridhar Sadasivam, Maria KY Chan, and Pierre Darancet. Theory of thermal relaxation of electrons in semiconductors. In: *Physical review letters* 119.13 (2017). `https://journals.aps.org/prl/abstract/10.1103/PhysRevLett.119.136602`, p. 136602.

[187] Xiao Tong and Marco Bernardi. Toward precise simulations of the coupled ultrafast dynamics of electrons and atomic vibrations in materials. In: *Physical Review Research* 3.2 (2021). `https://journals.aps.org/prresearch/abstract/10.1103/PhysRevResearch.3.023072`, p. 023072.

[188] John M Ziman. *Electrons and phonons: the theory of transport phenomena in solids.* Oxford university press, 2001.

[189] Joachim Appel. Electron-electron scattering and transport phenomena in nonpolar semiconductors. In: *Physical Review* 122.6 (1961). `https://journals.aps.org/pr/abstract/10.1103/PhysRev.122.1760`, p. 1760.

[190] MV Fischetti. Effect of the electron-plasmon interaction on the electron mobility in silicon. In: *Physical Review B* 44.11 (1991). `https://journals.aps.org/prb/pdf/10.1103/PhysRevB.44.5527`, p. 5527.

[191] Anna Hauber and Stephen Fahy. Scattering of carriers by coupled plasmon-phonon modes in bulk polar semiconductors and polar semiconductor heterostructures. In: *Physical Review B* 95.4 (2017). `https:`

//journals.aps.org/prb/pdf/10.1103/PhysRevB.95.045210, p. 045210.

[192] A Mooradian and GB Wright. Observation of the interaction of plasmons with longitudinal optical phonons in GaAs. In: *Physical Review Letters* 16.22 (1966). https://journals.aps.org/prl/abstract/10.1103/PhysRevLett.16.999, p. 999.

[193] BB Varga. Coupling of plasmons to polar phonons in degenerate semiconductors. In: *Physical Review* 137.6A (1965). https://journals.aps.org/pr/abstract/10.1103/PhysRev.137.A1896, A1896.